

THÈSE DE DOCTORAT

de l'Université de recherche Paris Sciences et Lettres
PSL Research University

Préparée à Ecole Supérieure de Physique et de Chimie
Industrielles de la Ville de Paris

Vers la production de "patchy particles" à base de cristaux liquides

Ecole doctorale n°564
PHYSIQUE EN ÎLE-DE-France

Spécialité Physique

Soutenue par Kunyun HE
le 23 Mars 2018

Dirigée par **Olivier DAUCHOT**
& **Teresa LOPEZ-LEON**

COMPOSITION DU JURY :

Mme. LACAZE Emmanuelle
Institut des NanoScience de Paris CNRS-
Université Pierre et Marie Curie,
Rapporteur

M. BRASSELET Etienne
Université de Bordeaux, Rapporteur

Mme. LINDNER Anke
ESPCI Paris, Président

Mme. ISHII Yoko
Kyoto University, Examineur

M. DAUCHOT Olivier
ESPCI Paris, Directeur de thèse

Mme. LOPEZ-LEON Teresa
ESPCI Paris, Codirecteur de thèse

Towards the realization of liquid crystalline “patchy particles”

Abstract

One main goal of modern material science is to produce complex three-dimensional architectures from the self-assembly of pre-designed colloidal building blocks. Developing methods to produce colloidal particles capable to interact in complex ways is crucial in this perspective. This thesis describes a new strategy in which liquid crystals are used for producing anisotropic colloidal particles. These new particles are double emulsions where a nematic liquid crystal is confined to a spherical shell, the geometry of which imposes the presence of topological defects. The number and position of the defects set the valence of the particles as well as the directionality of the eventual bonds between them. Our study aims at fabricating such liquid crystal shells in a controlled way, both in terms of size and defect structure. We describe the standard microfluidic methods used to produce liquid crystal shells and test their operational limits. We show that the standard microfluidic techniques do not allow for scaling the system down to the colloidal scale. We then present a new microfluidic set-up which improves our capability of producing shells in a large range of sizes at high frequencies. Combining experiments and numerical simulations, we study the possibility of inducing transitions between different valence states through a continuous variation of the shell geometry. Finally, we study a lyotropic chromonic liquid crystal, which exhibits a large elastic anisotropy in the nematic phase. We study how this exotic nematic liquid crystal responds to confinement and curvature and investigate the new emerging symmetries.

Keywords: Liquid crystals, topological defects, microfluidics, double emulsions, anisotropic colloids, self-assembly.

Vers la production de “patchy particles” à base de cristaux liquides

Résumé

L'un des objectifs majeurs de la recherche contemporaine en science des matériaux est la production d'architectures tridimensionnelles complexes grâce à l'auto-assemblage de briques élémentaires colloïdales. De ce point de vue, le développement de méthodes permettant la production de particules colloïdales capables d'interagir entre elles de façon complexe est donc crucial. Cette thèse décrit une nouvelle stratégie pour produire des particules anisotropes à l'aide de cristaux liquides. Il s'agit de doubles émulsions, où un cristal liquide nématique est confiné à l'intérieur d'une coque sphérique, et dont la géométrie impose la présence de défauts topologiques. Le nombre et la position des défauts déterminent la valence des particules ainsi que la directionalité des futures liaisons entre celles-ci. Dans cette étude, nous fabriquons de telles coques de cristaux liquides de façon contrôlée à la fois vis-à-vis de leur taille et des configurations de défauts. Nous décrivons les méthodes microfluidiques traditionnelles qui permettent de produire des coques de cristaux liquides, et nous en testons les limites de fonctionnement. Nous montrons que ces techniques ne permettent pas de réduire la taille du système à l'échelle colloïdale. Nous présentons un setup microfluidique amélioré, qui nous permet de produire des coques avec une grande distribution de taille et à haute fréquence. En combinant résultats expérimentaux et simulations numériques, nous étudions la possibilité d'induire des transitions entre différentes configurations de défauts, grâce à une modification continue de la géométrie de la coque. Enfin, nous nous intéressons à un cristal liquide chromonique doté d'une grande anisotropie élastique en phase nématique. Nous étudions la manière dont ce nématique exotique répond à l'influence du confinement et de la courbure, et nous explorons les nouvelles symétries qui en émergent.

Mots Clés: Cristaux liquides, défauts topologiques, microfluidique, émulsions doubles, particules anisotropiques, auto-assemblage.

Acknowledgments

I would like to extend my sincere gratitude and appreciation to all those who have contributed to the work presented in my thesis.

For this thesis I would like to thank my reading committee members: Emmanuelle Lacaze and Etienne Brasselet, for their time, brilliant comments and suggestions. I would also like to thank the examiners of my defense committee: Anke Lindner and Yoko Ishii, for their time and insightful questions.

Special mention goes to my enthusiastic advisors, Teresa Lopez-Leon and Olivier Dauchot. My PhD has been an amazing experience and I appreciate all their contributions of time and ideas to make my Ph.D. experience productive and stimulating. I am extremely grateful to Teresa, not only for her guidance and all the useful discussions, especially during the difficult experimental development stage, but also for giving me so many wonderful opportunities for attending academic conferences, which gave me a lot of inspiration, motivation and confidence during my PhD. My sincere thanks to Olivier for his encouragement, guidance and valuable suggestions. The joy and enthusiasm he has for his research was contagious and motivational for me.

I gratefully acknowledge the funding sources, Chinese Scholarship Council, that made my PhD work possible.

I have worked with talented experimental and theoretical collaborators without whom my research would not have been possible. I thank our collaborators from the University of Seville, Jose Manuel Gordillo, Francisco Campo-Cortés and Enrique Sanchez for their constant help in building the experimental setup. I express my deep sense of gratitude to Jose Manuel and Francisco for their devoted interest, valuable guidance and the support when so generously hosting me in Seville. I extend my gratefulness to the collaborators from de Pablos group at the University of Chicago. My sincere thanks to Professor Juan de Pablo for giving his scientific expertise, beneficial criticism and the exchange of novel ideas. Special thanks go to Ye Zhou and Hadi Ramezani-Dakhel for performing numerical simulations and sharing their thoughts. I thank Alberto Fernandez-Nieves for his helpful comments and suggestions during his visit in our lab. I also thank Yoko Ishii for her advice and field guidance during her stay in our team. I am grateful to Randall Kamien and Lisa

Tran for their hospitality at the University of Pennsylvania and their kind invitation to the Gordon Research Conference.

Millions of thanks go to the EC2M team members for the good moments we had working together. My sincere thanks go to Mathilde Reyssat for her assistance and kind help at any time. I also express my gratitude to my colleagues and friends: Alexandre Darmon, for all his help and encouragement both experimentally and morally, and for the time we spent in the office that is full of art and science, Guillaume Briant, for his kind help and patience in all the situations, Guillaume Durey, for his continuous motivation and so many interesting and helpful discussions, Charlotte de Blois, for all the funny and great moments we had at lunchtime. I also thank Ben Huang, Kamel Khelloufi, Martyna Goral and Dae-seok Kim for their help in the lab. I would like to thank Elie Raphaël, the director of Gulliver lab, Stéphanie Ledoux, Solange Rogue and all the other researchers and students from the group, for the nice working atmosphere.

My time in Paris was enjoyable due to the many friends and groups that became a part of my life. I extend my special thanks to Suyuan Dong, Jun Sun, Jingwen Zhao, Conghui Jiang, Ran Chen, Xiaohan Zhou, Andong Li and all the other friends for their support, advice, care, affection and strength. I would like to thank everyone who played an important role during my research tenure: Fei Ye, Yanan Liu, Menghua Zhao, Mathilde Bercy, Michael Benzaquen, Wen Ma, Haidai Hu, Chuande Wang, Hualin Wang, Xin Ye, Lihui Hu, Bin Fang, Tao Song, as well as expressing my apology that I could not mention personally one by one.

A special thanks to all my teachers and professors for their influence and impact have had on my life.

Lastly, I would like to thank my family for all their love, care and encouragement. For my loving parents, my sisters and brothers who supported me in all my pursuits. And most of all for Quanyi Yin, for his continued and unfailing support, care, understanding and standing beside me during the past 11 years. Without his help, I would not have been able to complete much of what I have done. Thank you!

Contents

| | |
|---|-----------|
| Introduction | 9 |
| 1 Confined liquid crystals: theory and methods | 19 |
| 1.1 Introduction to liquid crystals | 19 |
| 1.1.1 Liquid crystalline phases | 19 |
| 1.1.2 Director and order parameter | 21 |
| 1.1.3 Frank-Oseen elastic energy | 22 |
| 1.2 Surface anchoring | 23 |
| 1.3 Topological defects | 25 |
| 1.3.1 Singularities of the nematic order | 25 |
| 1.3.2 The 3D-expansion of 1/2 point defects | 27 |
| 1.3.3 Fully 3D defects | 29 |
| 1.3.4 Topological defects and curvature | 30 |
| 1.4 Nematic droplets | 31 |
| 1.5 Nematic shells | 33 |
| 1.6 Materials and methods | 34 |
| 1.6.1 Materials | 34 |
| 1.6.2 Experimental methods | 38 |
| 1.6.3 Numerical methods | 41 |
| 2 Exploring the limits of standard microfluidic techniques | 43 |
| 2.1 Standard microfluidic techniques for droplet production | 43 |
| 2.1.1 Fabrication of liquid crystal shells using an axisymmetric glass-capillary device | 46 |
| 2.1.2 Device testing through variation of inter-capillary distance | 49 |
| 2.2 Conclusion | 53 |
| 3 Towards the production of micro-sized liquid crystal shells using pressure gradients | 55 |
| 3.1 New microfluidic techniques for droplet production | 55 |
| 3.1.1 Micro- and nanoflows driven by electrical forces | 55 |
| 3.1.2 Microflows driven by pressure gradients | 57 |
| 3.2 Implementation of CSW technique for the production of liquid crystal shells | 60 |

| | | |
|----------|--|------------|
| 3.2.1 | Design and construction of the setup | 60 |
| 3.2.2 | Controlled injection of outer, middle and inner fluids | 63 |
| 3.2.3 | Operational conditions for the production of nematic shells | 65 |
| 3.3 | Size and thickness of the produced double emulsions | 69 |
| 3.4 | Scaling laws for the shell diameter and shell production frequency | 72 |
| 3.4.1 | Linear dependence between $P_o - P_a$ and U | 72 |
| 3.4.2 | Production frequency f | 74 |
| 3.4.3 | Inner (D_i) and outer (D_o) diameters of the nematic shells | 75 |
| 3.5 | Conclusion | 78 |
| 4 | Controlling the valency of liquid crystal shells through shell geometry | 79 |
| 4.1 | Defect configurations in nematic shells | 79 |
| 4.1.1 | Simulated nematic shells | 79 |
| 4.1.2 | Experimental nematic shells | 80 |
| 4.2 | Osmotic effects | 82 |
| 4.3 | Topological transitions between different defect configurations | 83 |
| 4.3.1 | De-confinement transitions in bivalent nematic shells | 83 |
| 4.3.2 | De-confinement transitions in trivalent nematic shells | 84 |
| 4.3.3 | Expulsion of inner droplets from nematic shells | 84 |
| 4.4 | Origin of expulsion of inner droplets from nematic shells | 86 |
| 4.4.1 | Energy barrier for the expulsion | 86 |
| 4.4.2 | Effect of water flux | 88 |
| 4.5 | Conclusions | 91 |
| 5 | Controlling the valency of liquid crystal shells through elastic anisotropy | 93 |
| 5.1 | Lyotropic chromonic liquid crystals | 94 |
| 5.2 | Spherical droplets | 95 |
| 5.2.1 | Phase diagram for the SSY-water system | 95 |
| 5.2.2 | Stable emulsions of SSY-water solutions in oil | 96 |
| 5.2.3 | Defect structures in a spherical SSY-water droplet | 98 |
| 5.3 | Sessile droplets | 101 |
| 5.3.1 | Sessile SSY-water droplet in contact with air | 101 |
| 5.3.2 | Sessile SSY-water droplet in contact with oil | 102 |
| 5.4 | Chromonic SSY shells | 107 |
| 5.5 | Conclusion | 109 |
| | Conclusions | 111 |
| | Bibliography | 113 |

Introduction

The dream of self-assembly

One main goal of modern material science is to produce complex three-dimensional architectures from the self-assembly of pre-designed building blocks. If the building blocks have a colloidal size, the materials resulting from their self-assembly might have unprecedented optical properties [1, 2]. In the last few years, there has been intense interest in creating, controlling, and assembling metamaterials: materials that owe their properties not to the microscopic constituents but, rather to the couplings, connections, and geometry [3]. Such materials are expected to have extraordinary properties and revolutionary technological applications as invisibility cloaks, sub-wavelength lenses, highly sensitive sensors, or super antennas [4]. However, the realization of these complex architectures remains challenging. Current fabrication methods rely on top-down approaches, where matter is structured from larger to smaller length scales [5]. Most of the top-down techniques, which involve the use of lithographic techniques are usually expensive, inefficient and limited in their ability to provide high resolution [6]. Complementary to these physical strategies are the chemically inspired bottom-up approaches [7], as it is the case of self-assembly processes, which offer a more flexible alternative to fabricate new types of colloidal architectures, especially in three dimensions [8–10]. Here, the complexity of the material depends highly on the type of interactions between the building blocks. Exploring new alternatives to produce building blocks capable of interacting in complex ways is key in this context.

Building blocks: one of the key issues

Much research in material science and condensed-matter physics in the past century has focused on studying the self-assembly of fundamental building blocks (typically atoms, molecules and colloidal particles) into bulk thermodynamic phases [8, 11, 12]. There has been particular interest in assembling complex structures from colloidal spheres due to their structural dimensions between 1 nm and 1 μ m [13]. Colloidal spheres with this range of size exhibit Brownian motion due to collisions with the solvent molecules [14]. The interactions between colloid spheres can lead to the formation of a great variety of phases, such as gasses, liquids, crystals, liquid crystals or glasses, depending on the properties of

both, the colloidal particle and the dispersing solvent [15,16]. In many senses, colloidal spheres can be considered as the mesoscopic counterparts of atoms, with the advantage of being large enough to be observed under a microscope in real space and real time [17,18]. Experimental studies on spherical colloids have enabled progress regarding fundamental problems relevant to condensed matter, such as nucleation, crystallization and nature of glass states [15,19,20]. On the other hand, spherical colloids also represent a class of ideal building blocks that could be assembled into long-range ordered lattices [20–23].

The drawback of colloidal spheres is that they do not interact in a directional fashion: while atoms interact in an anisotropic way, i.e., they form bonds along specific directions in space, colloidal particles interact with potentials that have spherical symmetry. Their self-assembly is usually induced by entropy minimization, which results in a limited selection of attainable close-packed crystal types: face centered cubic (fcc), hexagonal closed-packed (hcp), or body-centered cubic (bcc) [22,24]. Although the diversity of colloidal structures can be increased when particles of different size are assembled into dense binary colloidal crystals, many structures remain difficult or impossible to make [25,26]. For example, the diamond structure, which was predicted to have a full three-dimensional photonic bandgap more than 20 years ago [27], remains elusive because it requires fourfold coordination. Inducing anisotropy in the colloidal interactions is a current challenge.

Inducing anisotropy

Adding shape or surface anisotropy is a way to induce directional interactions between colloidal particles [21,28,29]. Recent advances in colloidal synthesis have made it possible to create almost monodisperse (sub)micrometer particles in various shapes and sizes: spheres, cubes, rods, plates, ellipsoids, stars and many other exotic geometries [30–32]. The shape anisotropy of non-spherical colloidal building blocks expands their potential to form more complex structures by self-assembly [33]. Lee *et al* [34] reported the synthesis of peanut-shaped colloids with a permanent transverse magnetic dipole and described how their self-organization is regulated by the strongly selective side-by-side magnetic interactions and their shape complementarity, see Fig. 1(a). Pine and co-workers elaborated a strategy to induce directional self-assembly by applying the lock-and-key principle to a colloidal system [35]. The method employs colloids with complementary shapes: colloidal spheres acting as keys and monodisperse colloidal particles with a spherical cavity acting as locks. The binding occurs spontaneously via depletion interaction, by means of which different assemblies could be formed, see Fig. 1(b). Similarly, Rossi *et al* [36] used depleting polymers and thermo-responsive nanoparticles to drive the crystallization of silica cubes into a precise face-to-face packing, forming large 3D simple cubic crystal lattices, see Fig. 1(c). New synthetic methods have also given access to a wide range of well-defined polyhedral nanocrystalline shapes [37,38], which can form colloidal lattices of different symmetries, some examples can be seen in Fig. 1(d).

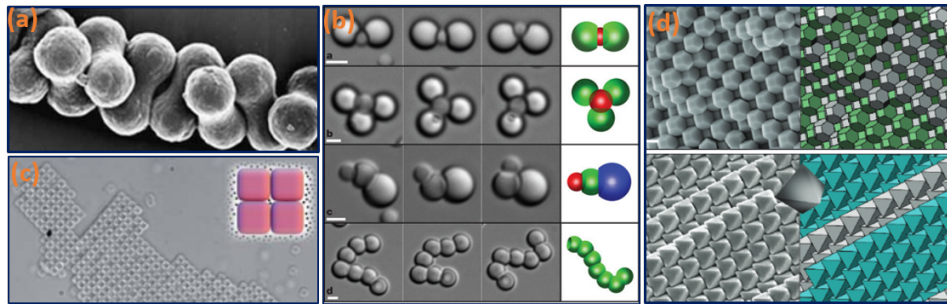


Figure 1: Self-assembly of nonspherical colloids. (a) Field emission scanning electron microscopy images of peanut-shaped particle chains under 2D confinement. Figure adapted from reference [34]. (b) Time-lapse optical microscopy images and schematics showing the flexibility of lock-key bonds in various assemblies. Figure adapted from reference [35]. (c) Silica cubes forming simple cubic crystals when driven by shape-selective depletion interactions. Figure adapted from reference [36]. (d) Scanning electron micrographs of the colloidal lattices and the corresponding diagrams of their densest known lattice packings. Figure adapted from reference [37].

Besides shape anisotropy, inducing specificity in the particle-particle interactions can give rise to complex crystalline structures [28, 39–41]. One of the most powerful strategies to achieve highly selective interactions between colloidal particles is to functionalize their surfaces with DNA strands and borrow from biology the binding specificity encoded into the DNA sequences [42, 43]. This opens up new opportunities for engineering crystalline assemblies, clusters and potentially self-replicating colloidal structures [44–47]. DNA-directed self-assembly of nanoparticles allows for regularly spaced network structures and extremely well-ordered superlattices to be assembled via fairly isotropic interactions that mimic metallic or ionic bonding. By using this strategy, Mafarlane and co-workers [48] succeeded in producing a number of different tailorable crystalline structures, see Fig. 2(a). Further development in DNA-mediated self-assembly has been done by introducing anisotropy in the particle shape. By using core nanoparticles with exotic shapes (triangular prisms, rods, and rhombic dodecahedra), while leaving the DNA design unchanged, Jones and co-workers [49] showed the emergence of new one-, two- and three-dimensional structures that could not be produced with spherical nanoparticles, see Fig. 2(b). The progress made in materials based on DNA-directed assembly is reported in a recent review [50].

Other than selectivity, surface functionalization can also provide colloids with directional interactions [28, 39, 40]. A possible approach, that has attracted much attention in the last years, is to decorate the surface of colloidal spheres with attractive “patches”, which can be made of synthetic organic or biological molecules. In that case, the particles would interact via patch-patch interactions. The bonding directionality and coordination number would be set by the position and number of patches. Numerical simulations [51, 52]

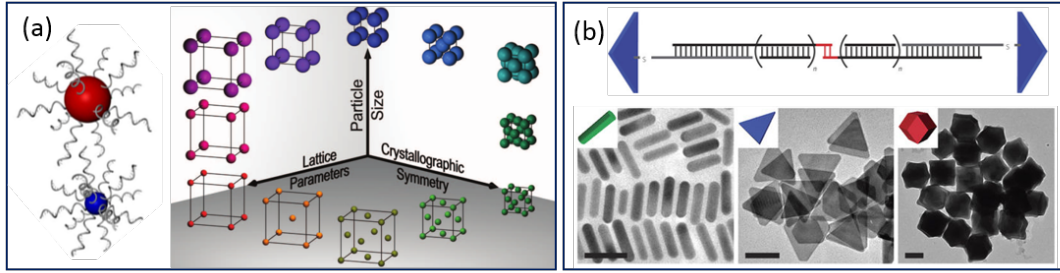


Figure 2: Self-assembly of DNA-functionalized particles. (a) Left: spherical nanoparticles functionalized with the appropriate DNA strands. Right: nanoparticle superlattice engineering with DNA. Figure adapted from reference [48]. (b) Top: schematic of the oligonucleotides used to assemble anisotropic nanostructures and bottom: transmission electron microscopy images of rods, triangular prisms and rhombic dodecahedra. The scale bars represent 50 nm. Figure adapted from reference [49].

have shown that a large variety of molecular-mimetic superstructures can be self-assembled from spherical patchy particles that would interact through the chemistry of their patterned surfaces. In a theoretical study, Zhang *et al* [53] demonstrated the possibility of forming diamond structures from the assembly of colloids with four attractive patches. This structure is of great interest because of the large photonic band gap it has been proposed to possess [27]. The idea of introducing patches on the surface of spherical particles to guide their self-assembly is conceptually simple, but it is challenging from an experimental point of view.

Experimental efforts done in the last decade have enabled the fabrication of particles with a large number of chemically distinct patches. A Janus particle [54], with two chemically distinct hemispheres, is the simplest example of a patchy particle. Janus particles with oppositely charged hemispheres have been shown to form clusters with interesting symmetries. More complex patchy particles have been recently produced by Granick *et al* who developed chemical protocols for functionalizing micrometer-sized colloidal spheres with three or more zones of chemical functionality, which can self-assemble into higher order structures [55, 56]. For instance, triblock particles, with three patches (north pole, south pole and equator) can lead to the formation of a colloidal Kagoma lattice, see Fig. 3(a) and (b). Triblock particles with asymmetrical patches [57] were also used to obtain a rich variety of open colloidal structures by staged self-assembly, see Fig. 3(c). Finally, particles with four small patches, produced by similar mechanisms, lead to the formation of tetrahedral clusters [58], as shown in Fig. 3(d). Very recently, Sacanna and colleagues [59] developed a physical approach, the so-called “colloidal fusion”, to produce patchy particles. The method involves the controlled coalescence of colloidal clusters into a single particle. At the core of the original cluster is a plasticizable particle, which is extruded outwards to eventually form the patches on the final particle. The location of the patches is therefore

defined and controlled by the packing geometry of the original cluster, as shown in Fig. 4.

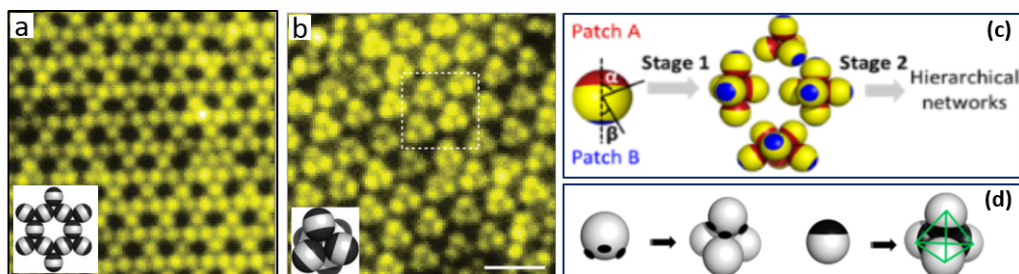


Figure 3: Self-assembly of patchy particles. (a) Fluorescence image of triblock Janus spheres assembled in a Kagome lattice. (b) A bilayer of parallel kagome lattices. Figure (a) and (b) adapted from reference [55]. (c) Schematics of hierarchical assembly based on the staged self-assembly of triblock spheres. Scale bar is $4 \mu\text{m}$. Figure adapted from reference [57]. (d) Two routes for self-assembly of a monodisperse tetramer from Janus spheres. Figure taken from reference [58].

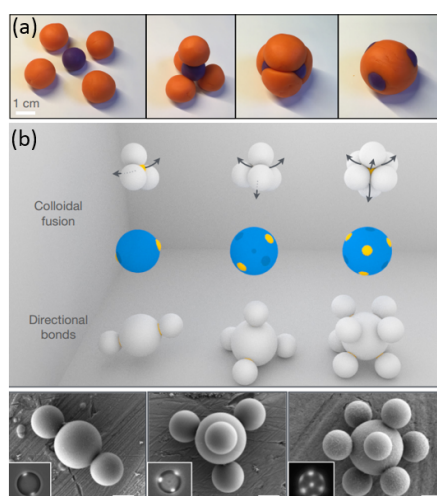


Figure 4: (a) Play-dough model illustrating the concept of colloidal fusion. (b) Schematics of liquid-core extrusion and directional bonds of three types of liquid-core colloidal clusters. SEM images at the bottom showing coordinated patchy particles with particles directionally sticking to patches. Insets are optical images of corresponding patchy particles with fluorescent patches. Scale bars are $1 \mu\text{m}$. Figure adapted from reference [59].

Despite the great progress made in the last years, we are still far from having a robust method that allows us to produce specific building blocks for the production of targeted

colloidal superlattices. The fabrication of patchy colloids with tailored symmetries involves synthetic challenges, and procedures to obtain some desired symmetries are still not available. Also, introducing patches in geometrically ordered locations on a spherical surface usually involves multistep processes, potentially limiting the scale on which such particles can be made. Methods based on the selective self-assembly of DNA-coated particles are more robust and easier to implement; however, they provide less control on the type of structure that can be attained. It has become more and more evident that new approaches need to be developed.

Liquid crystal shells: a new approach

A completely new approach has been proposed in a theoretical work by David Nelson [60]. This approach consists in coating spherical particles with nematic liquid crystals and functionalizing the topological defects that arise when nematic order is forced to develop on a curved surface. Indeed, when a nematic liquid crystal is confined to a spherical shell, a set of symmetrically positioned topological defects spontaneously appear at specific sites of the sphere, due to geometrical frustrations in the orientational order of the liquid crystal. These topological defects are not only mathematic concepts, but also physical entities with properties intrinsically different from the material in which they appear. In particular, defects are high energy spots suitable for chemical attack that could be functionalized with ligands. These topological defects, once functionalized, could act as attractive patches, providing a new and flexible pathway to produce colloidal “superatoms”: the number of defects would determine the valence of the particle and the defect positions would determine the bonding directionality [60–65]. Interestingly, the ground state of a two-dimensional nematic on a sphere is a state with four point defects sitting at the vertices of a tetrahedron [61, 62], as shown in Fig. 5(a), providing a route to produce colloidal crystals with the diamond structure, as shown in Fig. 5(b)-(d).

This idea has triggered an important amount of research in the last ten years, both from experimental and theoretical fronts. The first experimental study on nematic liquid crystal shells was performed by Fernandez-Nieves *et al* [66]. To confine the nematic liquid crystal to a spherical shell, they used double emulsions. They observed three different types of shells in terms of defect number: bivalent, trivalent and tetravalent. However, because of the thickness heterogeneity of the shell, the defects appeared all confined at the top part of the particle, see Fig. 6. In a later study by Lopez-Leon *et al* [67], they showed that the arrangement of defects can be controlled by the shell thickness gradient. If the resulting nematic shell is extremely thin, the bivalent, trivalent and tetravalent states display the symmetries of the sp^3 , sp^2 and sp orbitals of carbon atoms, as shown by the schematic diagrams in Fig. 7(c), (f) and (i), respectively. Additionally, further experimental and computational works have also shown that the number and positions of defects (the shell bonding properties) highly depend on other parameters such as the elastic constant of the

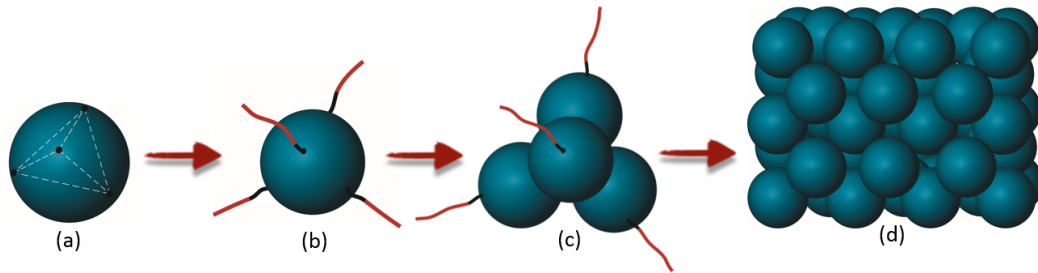


Figure 5: (a) Two-dimensional nematic texture on a sphere, which is characterized by four point defects at the vertices of a tetrahedron. (b) Tetravalent nematic colloid, where the topological defects have been functionalized with ligands, such as DNA strands. (c) Tetrahedral symmetry resulting from the self-assembly of tetravalent nematic colloids. (d) Colloidal crystals with diamond-like symmetry.

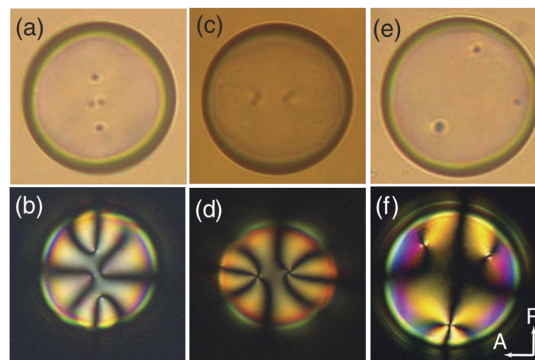


Figure 6: Three types of nematic shells commonly observed between crossed polarizers, distinguished by the number and type of defects: (a), (b) four defects, (c), (d) two defects, (e), (f) three defects. Figure adapted from [66].

liquid crystal [63,64,67], the molecular anchoring at the boundaries [68–70], or the presence of external fields [65], providing new possibilities for creating new valences or directionalities.

The complexity of the defect configurations increases when considering liquid crystals of lower symmetry, such as cholesteric [72, 73] or smectic liquid crystals [74, 75]. This is clearly shown in a recent work by Tran *et al* [76], where they studied a cholesteric shell with weak homeotropic molecular anchoring (the liquid crystal molecules are oriented perpendicularly to the shell boundaries). By playing with the anchoring strength they showed the emergence of new states and associated surface structures: a state where thick stripes decorate on the surface of the shell, Fig. 8(a), and a state where thin stripes wrap into double spirals, Fig. 8(b).

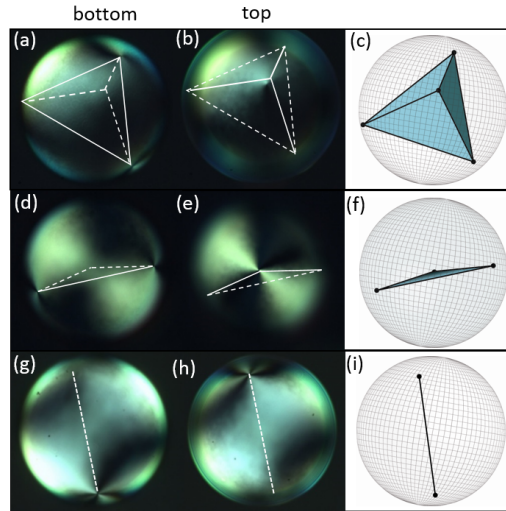


Figure 7: (a-b) Cross-polarized images of a very thin shell with four defects, (c) Schematic diagram of the observed arrangement of the four defects, (d-e) Cross-polarized images of a very thin shell with three defects, (f) Schematic diagram of the three-dimensional arrangement of the three defects, (g-h) Cross-polarized images of a very thin shell with two defects, (i) Schematic diagram of the observed arrangement of the two defects. Figure from reference [71].

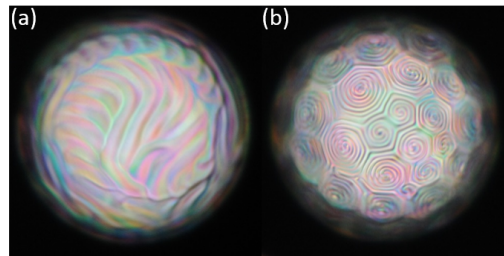


Figure 8: (a) Thick stripes and (b) double-spiraled thin stripes emerge on a cholesteric shell as the anchoring strength is varied. Image taken by G. Durey [76].

The above mentioned studies have revealed a great richness in defect configurations spontaneously emerging in liquid crystal shells, which opens a large spectrum of possibilities for inducing directional interactions between particles. Although the desired tetrahedral arrangement of four defects have already been produced in nematic shells [71], several key challenges remain to be addressed to achieve Nelson's idea. The first milestone is to scale down the size of liquid crystal shells to the colloidal range. The liquid crystal shells that we produce today have a size in the range of $100 \mu\text{m}$, and thus, they are not brownian particles. Reducing their size is important for both triggering spontaneous self-assembly and for producing crystals where the optical index is modulated at a micron scale. The standard microfluidic techniques usually employed to produce the shells do not allow for

a large scale variation of the shell diameter. Therefore, new shell production techniques need to be developed to scale down the shells to the colloidal size. The second milestone is to produce a large spectrum of multivalent shells in a controlled way, that is, to have good control over the valence, i.e. the number of defects, and the bond directionality, i.e. the position of the defects. Although it has been shown that a number of possible defect configurations can be stabilized by different methods, we are not able to produce monodisperse samples of targeted defect structures yet, because of the existence of metastability. The third milestone regards the functionalization of the topological defects. This will certainly require some dedicated efforts on designing a suitable strategy. This thesis is largely concerned with the first two milestones: 1) reducing the size of the shells; 2) producing shells with a controlled defect structure. In the next section, we present an outline of the rest of the thesis, where we briefly describe the specific works performed.

Outline of subsequent chapters

The rest of this thesis is organized as follows.

In Chapter 1, we review the general concepts concerning liquid crystals and topological defects. Then, we introduce our experimental systems and the methods used to study them.

In Chapter 2, we describe the standard microfluidic methods typically used to produce liquid crystal shells. We test the operational limits of glass capillary devices by playing with the geometry of the device and flow rates.

In Chapter 3, we present a new microfluidic set-up based on "Confined Selective Withdrawal" (CSW). We establish the production regimes for nematic shells and study how the different control parameters influence the geometry of the produced shells.

In Chapter 4, we investigate the presence of metastability in nematic shells. By inducing a continuous variation of the shell geometry, we study the possibility of forcing the transition from one defect configuration into another one.

In Chapter 5, we study a new type of nematic liquid crystal, a lyotropic chromonic liquid crystal, where the elastic constant associated to twist deformation is much lower than the other elastic constants of the liquid crystal. This results in the emergence of spontaneous twist in the liquid crystal. We study how this exotic nematic liquid crystal responds to confinement and curvature and investigate the new emerging symmetries.

Chapter 1

Confined liquid crystals: theory and methods

In this chapter, we introduce the theoretical framework necessary for the study of nematic phases in spherical geometries. We first discuss fundamental concepts associated to the nematic phase, such as elastic energy or molecular anchoring. We bring in the concept of topological defect and classify the different types of defects in terms of their charge and dimensionality. We establish then the topological constraints associated to spherical confinement and show the different defect configurations that these constraints can lead to for the specific cases of bulk nematic droplets or spherical shells. Finally, we describe the materials and methods employed in the rest of the thesis.

1.1 Introduction to liquid crystals

1.1.1 Liquid crystalline phases

Liquid crystal phases, also called mesomorphic phases [77], are intermediate states of matter between isotropic liquids (i.e., molecules with no long-range order) and crystalline solids (i.e., molecules with both orientational and positional long-range order). Liquid crystalline mesophases are more ordered than ordinary liquid phases, but less ordered than crystalline phases [78, 79]. They typically exhibit orientational order and even positional order in some spatial directions. This partial molecular order leads to interesting physical properties: liquid crystals (LCs) can flow as conventional fluids, yet they have other properties, such as birefringence, that typically exists in crystals.

To generate liquid crystal mesophases, the molecules have to be anisotropic. Either their shape is such that one axis is very different from the other two, or, in some cases, different parts of the molecules have very different solubilizing properties. From their molecular structure LCs can be divided into two types: calamitic LCs, where the molecules are rod-

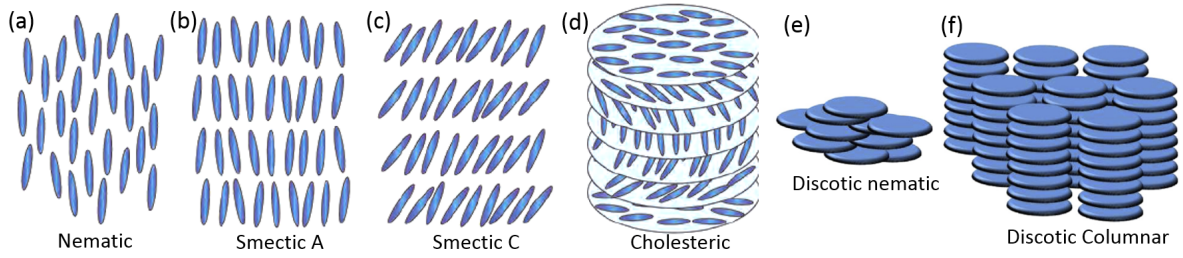


Figure 1.1: Schematic representation of the molecular arrangement in (a) Nematic, (b) Smectic A, (c) Smectic C and (d) Cholesteric phases. Blue rod represents the calamitic liquid crystal molecules. Structure of the nematic phase (e) and the columnar phase (f) of disc-like molecules.

shaped, or discotic LCs, where the molecules are disk-like. A number of different liquid crystal phases have been observed in calamitic liquid crystals. The simplest one is the nematic phase in which the molecules align along their long axis leading to maintain a preferred orientational order but have no positional order [80], as depicted in Fig. 1.1 (a). Two other phases common to calamitic liquid crystals are smectic and cholesteric phases. In addition to the orientational order of nematic LCs, smectic LCs exhibit one-dimensional positional order since the molecules organise themselves in layers [81]. In the smectic A phase, the molecules are perpendicular to the layers, as shown in Fig. 1.1 (b), while in the smectic C phase, the molecules are tilted with respect to the layer, as shown in Fig. 1.1 (c). In the cholesteric phase, also called twisted nematic, the molecules display long range orientational order, but the preferred molecular orientation continuously rotates along a perpendicular axis, leading to a twisted helical molecular arrangement [82], as shown in Fig. 1.1 (d). The cholesteric LC can therefore be regarded as a structure of equally spaced planes showing a common molecular orientation. Disk-like molecules can also form a number of liquid crystal phases [83]. The most symmetric one is the nematic phase, which is characterized by an orientational order of the discs without any long-range positional order, as shown in Fig. 1.1 (e). Another distinct category is the columnar phase, in which the disks stack up to produce columns, the different columns constituting a two-dimensional crystalline lattice, as shown in Fig. 1.1 (f).

Transitions between different phases can be triggered in two different ways: by purely thermal processes or by the influence of solvents. Liquid crystals obtained by the first method are called thermotropic LCs, while those obtained by the second one are called lyotropic LCs. In thermotropic LCs, the characteristic ordering only depends on temperature. In the case of nematics, the following phase transitions are considerable: solid-nematic-isotropic liquid (see Fig. 1.2). Cooling below the nematic-isotropic transition point T_{NI} , the liquid becomes turbid, which indicates a phase transition to the liquid crystalline state. Finally, below the melting point T_m the system is solid. In lyotropic LCs, however, the concentration of the solution is more important than the temperature in de-

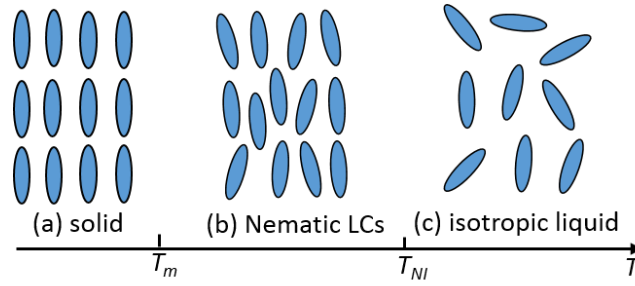


Figure 1.2: Schematics of three distinct phases of matter: (a) Crystalline phase, (b) Nematic phase, (c) Isotropic phase. The thermotropic nematic phase exists within a particular temperature range $T_m - T_{NI}$.

termining whether a liquid crystal phase is stable.

In this thesis, we will focus on nematic phases. Chapter 3 and 4 concern calamitic thermotropic LCs, while Chapter 5 deals with lyotropic LCs formed by aqueous solution of disk-like molecules, with the focus on nematic and columnar phases.

1.1.2 Director and order parameter

The long-range orientational order of nematic phases is described by the director n [54], which indicates the average molecular orientation at a given point in space. In calamitic liquid crystals, n corresponds to the direction along which the rod-like molecules align, as shown in Fig. 1.3(a). In the nematic phase, there is no polar ordering, i.e., n and $-n$ are equivalent [84]. Due to thermal fluctuations, the orientations of the individual molecules will differ from n , which is determined by averaging the orientation of all the molecules. Let's assume that the direction of the preferred orientation at one point in the sample is along the z axis, and that the long axis of a molecule makes an angle θ with respect to the preferred direction, as shown in Fig. 1.3(b). The degree of orientational ordering of the rod-like molecules in the nematic phase is determined by the nematic scalar order parameter S :

$$S = \left\langle \frac{3 \cos^2 \theta - 1}{2} \right\rangle \quad (1.1)$$

The order parameter S quantifies the total degree of ordering [85, 86], where θ is the angle between the director and the long axis of each molecule. The values of the order parameter S are therefore restricted to the interval $[-1/2, 1]$ with $S = 1$ for a perfectly oriented system and $S = 0$ for completely disordered phase [87]. The negative value of $S = -1/2$ corresponds to a state where all the molecules are aligned perpendicular to the director. In nematics with positive values of S , the molecules prefer to orient parallel to the director n . In a typical liquid crystal, the values for the order parameter range between 0.3 and 0.8. S decreases upon approaching the isotropic phase, and vanishes discontinuously at

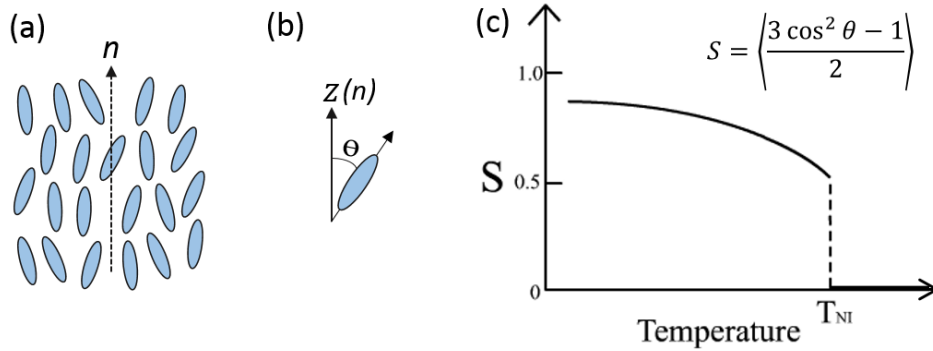


Figure 1.3: Director and order parameter in nematic liquid crystals. (a) n is the local director, showing the average molecular orientation at a given point in space. (b) θ is the angle between the mesogen molecule axis and the local director. (c) Typical evolution of the order parameter S with temperature. T_{NI} is the clearing temperature, i.e. the critical temperature at which the nematic-isotropic phase transition takes place.

the transition to the isotropic phase, as shown in Fig. 1.3(c). In this thesis, we will work at a temperature far from the nematic-isotropic phase transition in the absence of any external field, where S approximately is constant and the free energy of the system can be expressed solely in terms of $n = n(\bar{r})$.

1.1.3 Frank-Oseen elastic energy

In nematic liquid crystals, the uniform parallel alignment of the local director corresponds to the state of minimum free energy. Boundary conditions or external fields, however, may result in continuous variations of the preferred orientation n at different positions in the sample. Such continuous variations of the director field n lead to specific elastic deformations in the system. Any deformation of the director field can be expressed as a combination of three fundamental deformation modes: splay, twist, and bend, as schematically shown in Fig. 1.4. The variations of the director n in space induce an increase of the free energy, the contribution of each type of deformation to the overall energy density F is given by the Frank-Oseen equation [88, 89]:

$$f_{(n)} = \frac{1}{2}K_1(\nabla \cdot n)^2 + \frac{1}{2}K_2[n \cdot (\nabla \times n)]^2 + \frac{1}{2}K_3[n \times (\nabla \times n)]^2 \quad (1.2)$$

Where K_1 , K_2 , K_3 denote, respectively, the splay, twist, and bend elastic constants.

There are other deformation modes that can also contribute to the free energy density $f_{(n)}$, such as *splay-bend* and *saddle-splay* terms [90, 91]:

$$f_{13} = K_{13} \nabla \cdot [n(\nabla \cdot n)] \quad (1.3)$$

$$f_{24} = -K_{24} \nabla \cdot [n(\nabla \cdot n) + n \times (\nabla \times n)] \quad (1.4)$$

where K_{13} and K_{24} are the *splay-bend* and *saddle-splay* constants, respectively. Their effects are primarily limited to the surface of the nematic liquid crystals [92]. Hence, unless strong distortions occur in the close vicinity of the surface, K_{13} and K_{24} can be neglected as compared to the bulk terms. Furthermore, the Frank elastic constants are often simplified by assuming a *one elastic constant approximation*: $K \equiv K_1 = K_2 = K_3$. With these assumptions, equation 1.2 simplifies considerably to become:

$$f_{(n)} = \frac{1}{2}K[(\nabla \cdot n)^2 + (\nabla \times n)^2] \quad (1.5)$$

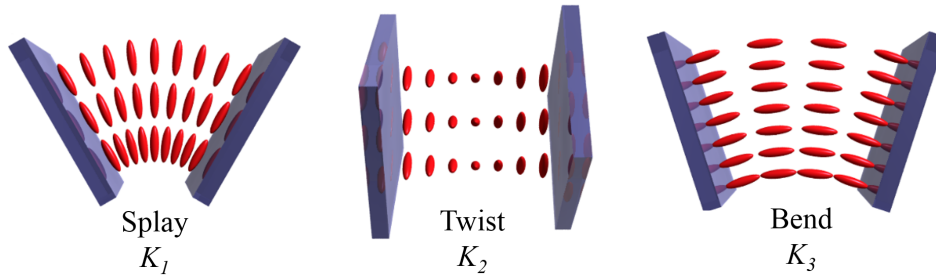


Figure 1.4: Schematic of splay, twist and bend deformation of the nematic director field n . Figure adapted from [93].

1.2 Surface anchoring

When the nematic phase is placed in contact with another phase (solid, liquid or gas) an interface is created which imposes a certain orientation to the director. The preferred orientation of the nematic director n at surfaces or interfaces is known as surface anchoring [94].

The orientation of the molecules with respect to the surface can be characterized using two angular components [84] shown in Fig. 1.5. The angle ϕ between the director projection and a reference direction on the substrate plane gives the measure of the azimuthal (in-plane) orientation of n . The zenithal (out of plane) angle, θ , between n and the substrate normal gives the tilt of n with respect to the surface. According to these angles, we can classify the anchoring in four categories. (i) uniform planar anchoring: $\theta = \pi/2$, $\phi = \text{constant}$ (Fig. 1.6(a)). (ii) homeotropic anchoring: $\theta = 0$ (Fig. 1.6(b)). (iii) degenerate planar anchoring: $\theta = \pi/2$, ϕ varies (Fig. 1.6(c)), and (iv) tilted anchoring: $0 < \theta < \pi/2$, $\phi = \text{constant}$ (Fig. 1.6(d)).

The preferred orientation of n at a given interface is called the easy axis. Any deviation of n from the easy axis has an energy cost. In the continuum description, the local free

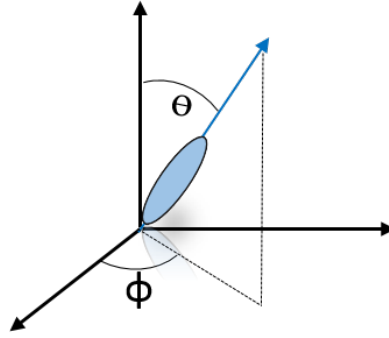


Figure 1.5: Schematic representation defining the two characteristic anchoring angles: polar anchoring angle θ and azimuthal anchoring angle ϕ .

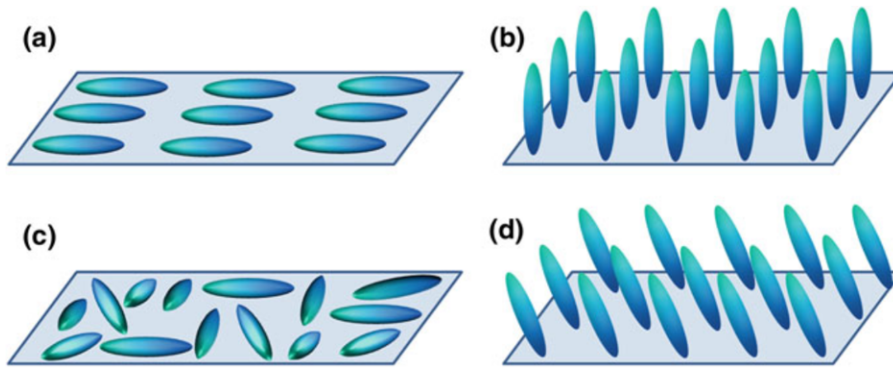


Figure 1.6: Anchoring of nematic liquid crystals on a surface: (a) a uniform planar anchoring, (b) homeotropic anchoring, (c) degenerate planar anchoring and (d) tilted anchoring. Figures adapted from [95].

energy has to be supplemented by a surface term f_s that takes into account these anchoring effects. In the Rapini-Papolar approximation [96], the surface anchoring energy is given by the following expression:

$$f_s = \frac{1}{2}W_\theta(\sin^2(\theta - \theta_0) + \frac{1}{2}W_\phi(\sin^2(\phi - \phi_0)) \quad (1.6)$$

Here, θ_0 refers to the preferred zenithal angle of the director field at surface; the difference $(\theta - \theta_0)$ reflects the deviation of the actual director field from this preferred angle. Similarly, $(\phi - \phi_0)$ represents the difference between the azimuthal orientation of the director field and the preferred direction. The coefficients W_θ and W_ϕ are designated as polar and azimuthal anchoring energies and they describe the strength of the anchoring of n at the surface. As a computational simplification, infinitely strong anchoring conditions are often assumed. In these cases, it is presupposed that the anchoring terms are large compared to the other energy terms in consideration, so that the elastic and field interactions are unable

to affect the interaction of the nematic at the surface. The orientation of the director field is then fixed at the boundary wall, and the surface terms can be neglected in any energy minimization. Under weak anchoring conditions, however, the surface orientation can be affected by elastic or field forces, and the surface terms must be reckoned with.

How to induce a given anchoring experimentally? In most of thermotropic LCs, a uniform planar anchoring on a solid substrate can be achieved by coating the substrate with a polymer layer and a subsequent mechanical rubbing procedure, by which the polymer chains are aligned along a specific direction. On such a substrate, n aligns parallel to the substrate along the rubbing direction. Often, the procedure works also by rubbing the bare substrate without polymer, microgrooves on the substrate surface are then assumed to be responsible for the uniform planar anchoring [94,97]. Homeotropic anchoring is obtained on solid substrates coated with monolayers of surfactants or other short chain-like molecules which self-assemble perpendicular on the substrate [98].

On fluid interfaces, the anchoring is given by the molecular interaction between the fluids at contact. In most of thermotropic liquid crystals, the nematic/air interface usually exhibits a strong homeotropic anchoring. On many other fluids, including water and glycerol, the anchoring is planar. Interestingly, the anchoring between two fluid phases can be modified by adding surfactant molecules. A systematic study about the effects of surfactants on the anchoring properties of liquid crystal-water interfaces shows the key role of the molecular architecture, alkyl-chain length and concentration of surfactants on the orientation of the liquid crystals at the interface [99]. If the surfactant molecule responds to oil-water interface by extending its non-polar alkyl chain homeotropically, it causes the liquid crystal molecules to align in a homeotropic orientation (Fig. 1.6(b)). Examples of surfactants that work in this way are ionic surfactants like sodium dodecyl sulfate (SDS) [100]. However, polymers, such as polyvinylalcohol (PVA) adsorb at the interface in a more or less random coil conformation, imposing tangential anchoring at the surface [101]. Those surfactants, or polymers give us the possibility of tuning the anchoring of fluid-liquid crystal interfaces. The details on the chemical features of the liquid crystals and stabilizers used in our experiment will be presented in section 1.6.

1.3 Topological defects

1.3.1 Singularities of the nematic order

In addition to the continuous variations of the director field shown in Fig. 1.4, topological defects can also be present in a nematic sample [102]. These defects are singularities where the director is locally undefined. In the close vicinity of the singularity, the order parameter is reduced and the elastic distortion becomes maximal. The system relaxes such distortion by creating a small isotropic region, referred to as *defect core* [103].

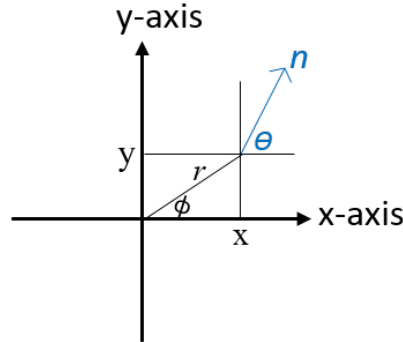


Figure 1.7: Coordinate system used to define the variation of n in space [104].

Defects can be classified in terms of their topological charge or winding number s [105, 106]:

$$s = \frac{1}{2\pi} \oint_{\mathcal{C}} d\ell (n_x \partial_{\ell} n_y - n_y \partial_{\ell} n_x) \quad (1.7)$$

where ℓ is the distance traveled along the loop \mathcal{C} enclosing the defect point. In other terms, the winding number measures the amount of rotation of the director field around the defect. Consider a planar structure in which the director is confined to the xy plane (the z axis being normal to n). At every point in the plane, the director has a specific orientation, given by the angle θ measured counter-clockwise from the x -axis, as shown in Fig. 1.7. In general, θ is a function of x and y , i.e., $\theta = \theta(x, y)$. The components of the director are : $n_x = \cos \theta(x, y)$, $n_y = \sin \theta(x, y)$, $n_z = 0$. Taking a centered circle of radius r for the loop \mathcal{C} , such that:

$$x = r \cos \phi, y = r \sin \phi, \text{ and } r = \sqrt{x^2 + y^2} \quad (1.8)$$

$$\phi = \tan^{-1}(y/x) \quad (1.9)$$

We seek simple solutions that depend linearly on ϕ and does not depend on r ; that is [82]:

$$\theta = s\phi + \theta_0 \quad (1.10)$$

where s and θ_0 are constants. This equation describes the director configuration around the defect. The director in a liquid crystal is a double headed arrow, this means that θ must change by some multiple of π when ϕ is increased by 2π in order to recover the initial orientation. This implies that the constant $s = m/2$ with $m = \pm 1, 2, 3, 4$.etc: only defects of integer or half-integer charge are compatible with the two-fold symmetry of the nematic phase. If s , which is also called the strength of the defect, is positive, then the director rotates in a counter-clockwise manner around a counter-clockwise path encircling the defect. If s is negative, the director rotates clockwise when traveling along the same counter-clockwise path. The director configuration for different types of defects

are illustrated in Fig. 1.8. Fig. 1.8(a) shows a $s = +1$ defect, where n rotates by 2π around the defect in a counter-clockwise way, while its negative counterpart is shown in Fig. 1.8(b). Fig. 1.8(c) shows a $s = +1/2$ defect, where n rotates by π in a counter-clockwise manner along one full loop around the defect, while its negative counterpart is shown in Fig. 1.8(d).

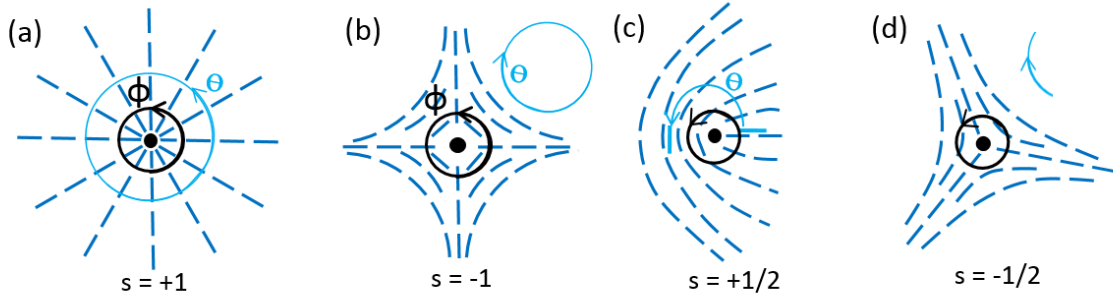


Figure 1.8: Schematic representations of topological defects in a two-dimensional nematic. The black dot indicates the point where the director is undefined, while the discontinuous lines represent the surrounding director field.

1.3.2 The 3D-expansion of $1/2$ point defects

The three-dimensional expansion of $s = \pm 1/2$ point defects leads to the formation of line defects, commonly referred to as disclinations, as schematically represented in Fig. 1.9(a) and (b). In this configuration, the director has no vertical component and the disclination is perpendicular to the plane of the molecules. Disclinations, observable as thread-like structures in nematic samples, are responsible for the name nematic (derived from the Greek name *nematos*, meaning thread). Experimentally, it is observed that only disclinations of strength $s = \pm 1/2$ are stable, whereas disclinations of higher strength are unstable. In particular, $s = \pm 1$ disclinations can relax their structure by escaping into the third (vertical) dimension, due to their cylindrical symmetry [83, 107]. Rather than forcing the director field to lie on the $x - y$ plane, it is allowed to have a vertical component, leading to a continuous structure with just a $s = +1$ singularity, called boojum [108], on each surface, as schematically shown in Fig. 1.10(a) and (b).

Under the one elastic constant approximation, the energy of an isolated disclination line per unit length is given by:

$$E = \int_{r_c}^R f_E(2\pi r) dr = \pi K s^2 \ln(R/r_c) \quad (1.11)$$

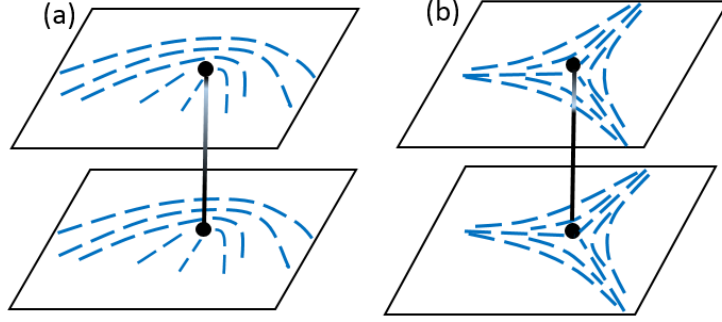


Figure 1.9: Schematic representations of $s = +1/2$ disclination (a) and $s = -1/2$ disclination (b) in three dimensional nematic director field.

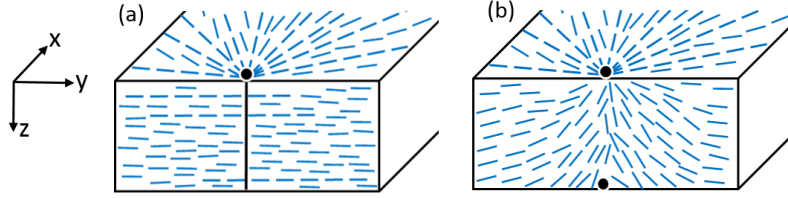


Figure 1.10: (a) Cross section showing the structure of a $s = +1$ disclination in the bulk, connecting two surface defects of the same sign. (b) An escaped structure joining two boojums.

where R is the size of the sample and r_c is a lower cutoff radius (corresponding to the size of the defect core), which is usually of molecular dimensions. Additionally, the average energy of the disclination varies as square of the *topological charge*, s . Hence, defects of integer defects ($s = \pm 1$) generally transform into low energy semi-integer ($s = \pm 1/2$) defect states. In the case of two defects of charge s_1 and s_2 separated by a distance r_{12} , the interaction energy between a pair of disclinations is given by [83, 109]:

$$E = \pi K (s_1 + s_2) s^2 \ln(R/r_c) - 2\pi K s_1 s_2 \ln(r_{12}/2r_c) \quad (1.12)$$

The assumption here is that $r_c \ll r_{12} \ll R$. If $s_1 = -s_2$, E becomes independent of R . The topological strength s is also called *topological charge* to emphasize that interactions between defects, as those between electrical charges, can either be repulsive or attractive. Indeed for $s_1 \cdot s_2 < 0$, the interaction force between defects is negative, as a result, defects approach and annihilate. In contrast, when $s_1 \cdot s_2 > 0$, the defects repel, eventually reaching the boundaries of the cell containing the nematic phase.

1.3.3 Fully 3D defects

Point defects in the nematic bulk are typically radial and hyperbolic hedgehogs, whose three-dimensional structures are shown in Fig. 1.11 (a) and (b). Hedgehogs are characterized by an integer *topological charge* q specifying how many times one meets all possible orientations of the director field while moving around a closed surface surrounding the point defect. By convention, a radial hedgehog has a topological charge $q = +1$ whereas a hyperbolic hedgehog is designated with $q = -1$. Since the nematic director n and $-n$ describe the same state, both hedgehogs in Fig. 1.11(a) and (b) are topologically equivalent, since they can be transformed into each other by a continuous transformation of the director field: the transformation of a hyperbolic hedgehog into a radial one can be done by rotating the director about the vertical axis through an angle π when going outwardly from the core in any radial direction.

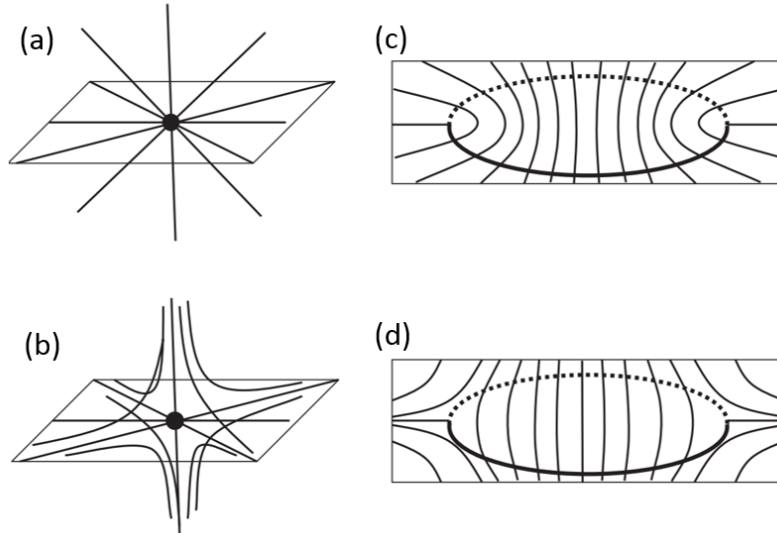


Figure 1.11: Schematic representations of (a) radial hedgehog defects with $q = +1$ and (b) hyperbolic hedgehog with $q = -1$. (c) Splitting of a $q = +1$ point defect into a $+1/2$ disclination loops. (d) Splitting of a $q = -1$ point defect into a $-1/2$ disclination loop. Figures adapted from [110].

These point defects also possess a fine structure at smaller length scales, which has attracted a lot of attention. It has been suggested by Melzer and Nabarro [111], on the basis of their observations, that point defects might split into disclination loops of strength $1/2$. Fig. 1.11(a) and (c) (or Fig. 1.11(b) and (d)) illustrate how a radial hedgehog (or hyperbolic hedgehog) opens up to a $+1/2$ (or $-1/2$) disclination ring by filling the inside of the loop with vertical lines of the director field. When considering the far field of the nematic director, in Fig. 1.11(c) (Fig. 1.11(d)), the disclination ring is still seen as a radial hedgehog (hyperbolic hedgehog). This means that the ring is assigned the same topological

point charge $q = +1$ (or $q = -1$). This transformation of points into disclination rings is allowed from the point of view of topology, while the energies of points and rings might be quite different, not only because of their size but also because of the type and degree of deformation. Detailed analysis of the energies of points and disclination rings is thoroughly discussed in [112, 113].

1.3.4 Topological defects and curvature

Without any external constraints, the ground state of a 2D planar nematic phase is characterized by a uniform director field. Topological defects may be generated in out-of-equilibrium states, for instance inducing a phase transition, but the defects appearing in these transient states end up annihilating each other. In contrast, when nematic liquid crystals are confined to a curved surface, boundary conditions impose unavoidable topological constraints on the director field that typically result in the presence of defects that are, in this case, topologically protected against annihilation [104, 114]. The total topological charge of a liquid crystal confined to a closed surface is imposed by the fundamental Poincaré-Hopf and Gauss-Bonnet theorems, which are connected to the Euler characteristic of the confining surface [115].

The Euler characteristic χ of the closed surface (such as a sphere or a torus) is a topological invariant that does not change under smooth deformations of that surface. The Euler characteristic for a closed surface can be obtained by triangulating the surface, and counting the number of vertices V_t , the number of edges E_d and the number of faces F_c of the resulting polygonal network [106]:

$$\chi = V_t - E_d + F_c \quad (1.13)$$

It can be shown that the Euler characteristic χ does not depend on the choice of the polygonal network, but it does depend on the type of closed surface chosen. The Gauss-Bonnet theorem relates the Euler characteristic of the closed surface S to its Gaussian curvature, as:

$$2\pi\chi = \oint_S K dS = \oint_S d\theta d\phi \cdot \nu \cdot \left[\frac{\partial \nu}{\partial \theta} \times \frac{\partial \nu}{\partial \phi} \right] \quad (1.14)$$

Here $K = \kappa_1 \kappa_2$ is the local Gaussian curvature and κ_1, κ_2 are the two principal curvatures at a given point on the surface. The vector ν is the local normal to the surface at the point under consideration. θ and ϕ are the two angles defining the position of the chosen point on the surface. For a sphere or any closed surface obtained by smoothly morphing the surface, one finds that the Euler characteristic is $\chi = 2$.

The Euler characteristic can also be defined through the *genus* g of the surface:

$$\chi = 2(1 - g) \quad (1.15)$$

The *genus* g is the number of handles one has to attach to a sphere to transform it into the surface under consideration. For a spherical surface $g = 0$, and thus, the Euler characteristic equals 2.

The Poincaré-Hopf theorem states that the sum of all *topological charges* s of the director field n on the closed surface is equal to the Euler characteristic of the surface, that is, 2 in the case of a sphere [116–118]:

$$\sum_i s_i = \chi \quad (1.16)$$

The Gauss-Bonnet theorem states that if the director field is normal to the closed surface, then, the sum of the *topological charges* q of all points inside the bounded volume is [119]:

$$\sum_i q_i = \chi/2 \quad (1.17)$$

that is, 1 in the case of a sphere. A trivial illustration would be a radial hedgehog located at the center of a sphere. These two theorems link the topology of the confining environment to the total required topological charge.

1.4 Nematic droplets

A spherical droplet of nematic liquid crystal is the simplest system that brings us to confront these topological questions. The particular director configuration in the droplet mainly depends on the anchoring conditions of the liquid crystal molecules at the droplet interface, which determine the boundary conditions for n , and fix the topological constraints on the liquid crystal. Here we consider that the anchoring at the drop surface is infinitely strong, then, fixed.

If the boundary conditions are homeotropic, i.e. n is normal to the surface, the topological constraints imposed by the Gauss-Bonnet theorem are fulfilled by forming a radial director field with a hedgehog defect of topological charge $q_{total} = +1$ located at the center of the droplet, as shown in Fig. 1.12(a) and Fig. 1.12(c). In contrast, for nematic droplets with planar boundary conditions, i.e. n is tangential to the surface, the topological constraints imposed by the Poincaré-Hopf theorem require a total topological surface charge $s_{total} = +2$ at the droplet interface. The liquid crystal typically meets these constraints by forming bipolar drops [120], which are characterized by two surface point defects or boojums [121] with topological charge $s = +1$ separated by a drop diameter distance, see Fig. 1.12(b) and (d). Such topologically required defects are analogous to the defects in the meridional field at the North and South Poles of the Earth globe [118], as schematically shown in Fig. 1.12(b).

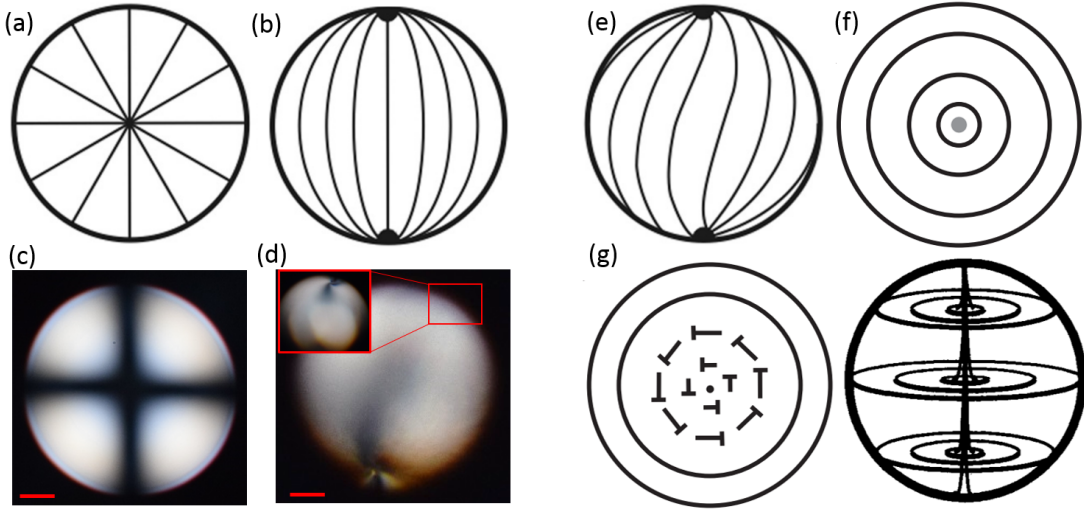


Figure 1.12: Examples of director configurations within nematic droplets, (a) radial configuration characterized by a point defect at the center of the sphere for normal boundary conditions. (b) bipolar configuration. Cross-polarized images of radial (c) and bipolar (d) nematic droplets corresponding to the director configuration within (a) and (b), respectively. (e) twisted bipolar and (f) concentric configurations for tangential boundary conditions. (g) Escaped concentric structure that has two diametrically opposed bend-type point disclinations on the surface. Nails indicate that the director is tilted with respect to the plane. Scale bars, $25 \mu\text{m}$. Figures adapted from [122].

The bipolar and radial structures are observed in most of nematic LCs, when the boundary at the droplet surface are planar and perpendicular, respectively. However, a number of other director configurations have been reported for specific systems [123]. Generally, the orientational LC structure depends not only on the boundary conditions, but also on the ratio of elastic constants, the size and form of the droplet as well as the presence of external fields. In a bipolar droplet, splay deformation is obviously present near the poles of the droplet and bend deformation dominates along the lines connecting the two poles. A variation to this configuration can be obtained by adding a twist deformation to the director field, while maintaining the point defects of the bipolar structure. The resulting configuration is similar to the standard bipolar one, except that the director field at the surface makes an angle α with respect to the meridional lines connecting the point defects, as shown in Fig. 1.12(c). The twisted bipolar structure becomes preferred over the untwisted bipolar one when: $K_1 \geq K_2 + 0.431K_3$ [124, 125], where K_1 , K_2 and K_3 are the elastic constants corresponding to splay, twist and bend deformations, respectively. This structure will be studied in Chapter 5, where we use a chromonic liquid crystal, where K_2 is much lower than K_1 or K_3 (in the nematic phase).

Another possible director configuration that fulfills the planar topological constraints is

the concentric structure, which possesses a line defect running along the droplet diameter. Here the director field is everywhere perpendicular to this line, grey dot in Fig. 1.12(f), arranged in a series of concentric circles. The concentric structure becomes energetically favorable when the ratio K_3/K_1 becomes sufficiently small [124, 126]. This structure is, however, unstable, as stated in section 1.3.2, since integer line defects are not stable. The line defect escapes into the third dimension via a twisted configuration [127, 128], yielding a virtual line defect connecting the two boojums of topological charge $s = +1$, as shown in Fig. 1.12(e).

The defect structures within nematic droplets mainly reveal the presence of integer surface defects because bulk effects dominates over surface effects. To stabilize half-integer defects, we have to consider more complex geometries, such as a shell geometry, where the nematic is confined between two spherical surfaces, see the schematics in Fig. 1.13(a).

1.5 Nematic shells

Compared to bulk droplets, nematic shells offer more degrees of freedom. In this case, the presence of an inner as well as an outer interface allow us to independently tune the anchoring conditions at the two boundaries. Moreover, by varying the size of the inner droplet, we can tune the shell thickness. In this thesis, we will focus on shells under planar boundary conditions and variable thickness. Here topological constraints exist on both the inner and outer surfaces, by that forcing the presence of defects with overall charge $s = +2$ on each interface.

For very thin shells, the ground state is predicted to have four $s = +1/2$ disclination lines at the vertices of a tetrahedron [61, 62], see Fig. 1.13(b). For thick concentric shells, see schematic in Fig. 1.13(a), the lower energy state is a bipolar configuration with two pairs of boojums. This structure, shown in Fig. 1.13(c), is reminiscent of the bipolar structure observed in droplets. Theory and numerical simulations have shown that the bipolar structure becomes favourable with respect to the tetrahedral structure when $h^*/R \simeq 0.5$ [62, 66, 129], where h is the shell thickness and R is the shell outer radius.

As we will see in the following section, experimental shells are double emulsions where an aqueous droplet is embeded inside a larger nematic droplet, which is in turn dispersed in an aqueous medium. Due to the density difference between the inner droplet and the liquid crystal droplet, the experimental nematic shells are usually heterogeneous in thickness, see Fig. 1.13(d), where the center of the inner sphere is shifted by Δ with respect to the center of the outer one. Numerical simulations have shown that this non-concentric geometry has an impact in the energy landscape of the system and leads to the formation of new defect structures [129–131]. In thin heterogeneous shells, the four $s = +1/2$ defects shift their positions towards the thin part of the shell, loosing the tetrahedral arrangement, as

shown in Fig. 1.13(e). A new structure becomes the ground state when the shell is thicker, and thus, more heterogeneous in thickness. This new structure combines a pair of $s = +1$ boojums, located in the thick region of the shell, with two $s = +1/2$ disclination lines, located at its thin part, see Fig. 1.13(f).

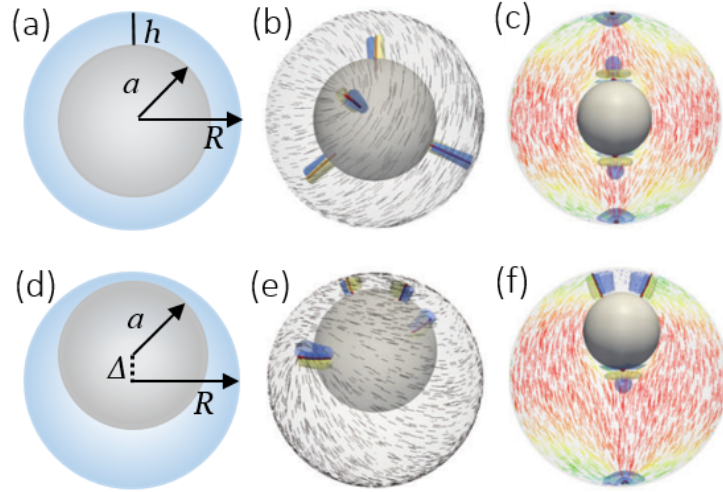


Figure 1.13: (a) Schematic side view of concentric shell. (b) and (e): Tetravalent defect configuration with four $s = +1/2$ defects, (c) Bivalent structure with two pairs of $s = +1$ defects. (d) Schematic side view of heterogeneous shell. (f) Trivalent configuration with one $s = +1$ defect and two $s = +1/2$ defects.

It is obvious that geometry plays a critical role in the type of defect structures appearing in the shells. In chapter 4, we will experimentally study the effect of the shell geometry on the type of defect structure appearing in experimental shells and the possibility of inducing transformations between different defect structures.

1.6 Materials and methods

1.6.1 Materials

In this thesis, we used two different types of liquid crystals: rod-like thermotropic liquid crystals (TLCs), which will be used in Chapter 3 and 4, and disk-like lyotropic chromonic liquid crystals (LCLCs), which will be used in Chapter 4. This section provides the details on their molecular structure and physico-chemical properties.

Thermotropic liquid crystals: 5CB

The thermotropic nematic liquid crystal used in our experiments is 4-Cyano-4'-pentylbiphenyl (5CB). Its molecular structure is shown in Fig. 1.14: it has two aromatic groups, ensuring the rigidity of the core, a more flexible carbonated chain, and a cyano group. The rod-like molecules can be approximated by cylinders with typical dimensions of 2 – 3 nm in length and 0.4 nm in diameter. The nematic phase is formed in a certain temperature range between 18°C and 35°C. The values of the elastic constants at room temperature are: $K_1 \simeq 6$ pN, $K_2 \simeq 3$ pN, and $K_3 \simeq 9$ pN [132, 133].

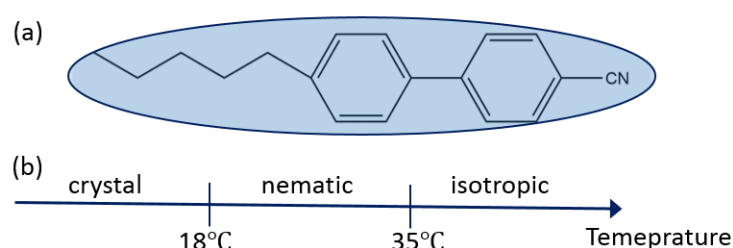


Figure 1.14: (a) Chemical structure of nematic liquid crystal 4-Cyano-4'-pentylbiphenyl (5CB). (b) Phase transition with temperature variation.

Thermotropic liquid crystals are typically oil-like, immiscible with water, thus stabilizers, also called emulsifiers, are needed to ensure the stabilization of liquid crystal shells/droplets. In our experiments, we add 1% of Polyvinyl alcohol (PVA) to both the innermost and outermost fluids to generate 5CB shells. This water soluble polymer, of chemical formula $[\text{CH}_2\text{CH}(\text{OH})]_n$, has hydrophilic -OH groups and a hydrophobic carbonated chain. As a result, the polymer lies parallel to a water-oil interface, with -OH groups pointing towards the aqueous phase. The emulsifying effect is then obtained when several layers of this polymer are adsorbed at the interface and induce contact repulsion between droplets [134]. The polymer not only acts as a stabilizer, it also imposes planar boundary conditions at the interface [101]. This is because 5CB contains an aromatic core, and a cyano group, which can participate in hydrogen bonding with the surrounding water, whereas the aliphatic chains at the mesogen end are avoided by the water [135]. In the case of shells, this parallel alignment is forced on both inner and outer surfaces.

Lyotropic chromonic liquid crystals: Sunset Yellow FCF (SSY)

Lyotropic chromonic liquid crystals (LCLCs) is a distinct family of lyotropic LCs, which are aqueous phases of supramolecular assemblies of small molecules, such as dyes, drugs, nucleic acids, and DNA [136]. The name “chromonic” was suggested because it connotes both color and chromosomes [137, 138]. Most LCLC molecules have a disk-like or plank-

like shape composed of polyaromatic cores surrounded by hydrophilic ionic or hydrogen-bonding solubilizing groups at the periphery [139, 140]. When dissolved in water, they undergo self-assembly via electrostatic forces between ionized polar groups, hydrophobic interaction, and $\pi - \pi$ interaction between aromatic cores to form elongated aggregates which act as building blocks of the mesophase [136, 141].

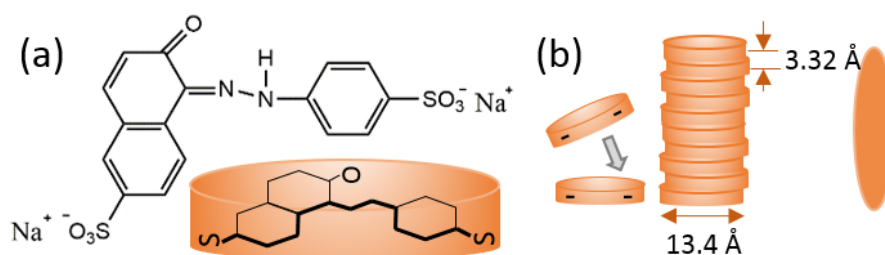


Figure 1.15: (a) Molecular structure of Sunset Yellow FCF (SSY) [142, 143]. (b) Schematic representation of aggregate formed by SSY molecules (orange disks) which act as the mesogens (orange ellipses). The aggregate diameter (13.4 Å) and the intermolecular separation (3.32 Å) were obtained from [144].

One of the best studied LCLCs is formed from concentrated solutions of sunset yellow FCF (SSY), a commonly used food coloring [142]. Fig. 1.15(a) shows the molecular structure of SSY. It contains central aromatic groups (phenyl and naphthyl rings linked via an azo group), with two solubilizing sulfonate groups attached to the end of the molecule. A schematic representation of the disk-like structure of the SSY molecule is shown in Fig. 1.15(a), by an orange-color disk. When SSY molecules are mixed with water, the molecules typically stack on top of each other face-to-face, leaving the solubilizing sulfonate groups at the aggregate/water interface. It has been shown that the aggregates are formed by a simple $\pi - \pi$ stacking [143, 145]. The aggregation process is believed to be isodesmic, that is, any addition or removal of molecules to the aggregate is always associated with the same energy cost. These aggregates act as mesogens, represented by the orange ellipses in Fig. 1.15(b), which can lead to liquid crystalline phases, as schematically shown in Fig. 1.16(a)-(c). At room temperature, the SSY aggregates form a nematic phase at concentrations between 30-40 wt%, and a columnar phase at concentrations above 40 wt% [144]. The phase diagram as a function of temperature and concentration is displayed in Fig. 1.16(d) showing the isotropic (I), nematic (N) and columnar (C) phases with broad coexistence regions. In the isotropic phase, Fig. 1.16(a), the SSY molecules are randomly oriented due to the low concentration of molecules, neither long-range positional nor orientational ordering are present. In the nematic phase, as the concentration of SSY increases, the aggregates multiply, grow, and align parallel to each other, as shown in Fig. 1.16(b). In the columnar

phase, Fig. 1.16(c), the aggregates form a hexagonal lattice in the plane perpendicular to n .

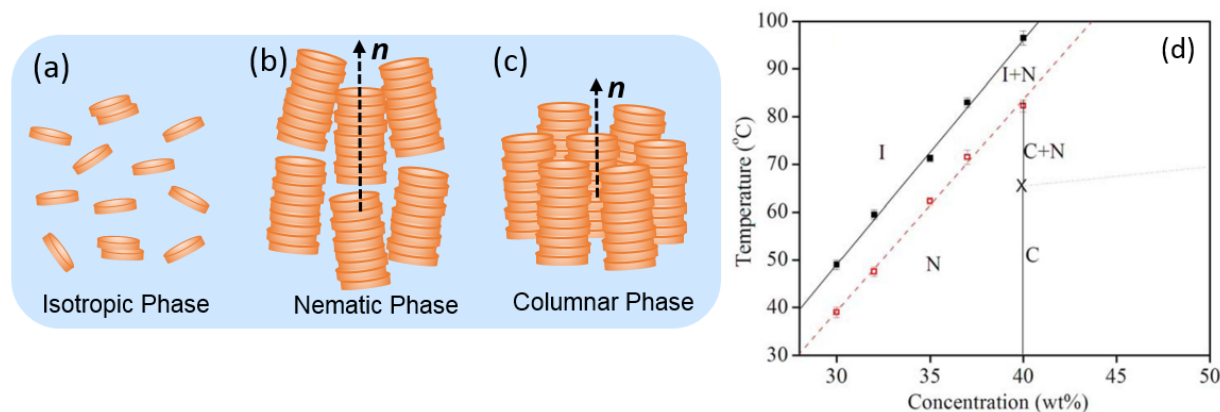


Figure 1.16: Schematic diagram of SSY aggregates in aqueous solution in (a) Isotropic phase, (b) Nematic phase, and (c) Columnar phase. (d) Phase diagram of SSY water solutions. The LC phase of SSY depends on the concentration (wt%) in horizontal axis and temperature in vertical axis. The two-phase coexistence are denoted by I + N (isotropic and nematic), N + C (nematic and columnar). Figure (d) adapted from [144].

Sunset Yellow FCF (SSY) was purchased from Sigma-Aldrich at a purity of 90%. SSY need to be purified before using. Briefly, raw SSY powder is well dissolved in Millipore water (resistivity $18.1 \text{ M}\Omega\cdot\text{cm}$) at $\sim 18 \text{ wt}\%$ in a large centrifuge tube with spare volume. Pure ethanol is added to cause the SSY to precipitate. The mixture is filtered by using a vacuum filtration method to isolate the precipitate. We keep the solids and dry them in the oven overnight. A mortar and pestle are used to break up the dried solids into powder. The above procedure was performed twice. Finally, the purified SSY is dehydrated by placing it in a vacuum oven for 2 days. We place the purified SSY in a well-sealed container.

Fluorinated oil and fluorosurfactant

Fluorinated oil is an inert fluid, often immiscible with both water and hydrocarbon oils. For this reason, it is very convenient for the production of stable double emulsions [146,147]. In this thesis, we use the mixture of fluorinated oil and fluorinated surfactant as either dispersed phase or continuous phase to generate liquid crystal double emulsions. The chemical structures of fluorocarbon oil and fluorinated surfactant that we use are shown in Fig. 1.17(a) and (b).

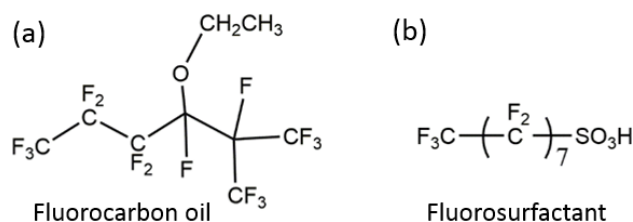


Figure 1.17: Molecular structure of fluorocarbon oil (a) and fluorosurfactant (b).

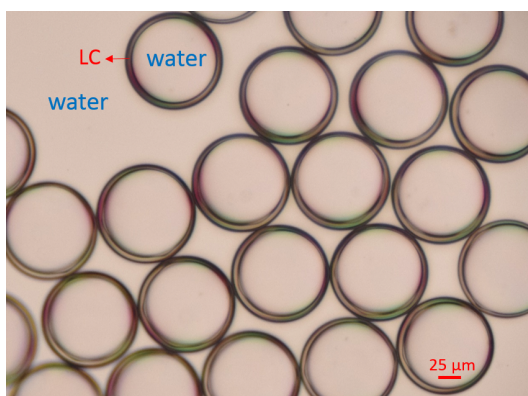


Figure 1.18: Optical micrograph of monodisperse liquid crystal shells.

1.6.2 Experimental methods

Production of shells by microfluidic techniques

We generate spherical shells of nematic liquid crystal using microfluidic techniques [148] that will be studied in detail in chapter 2 and 3. The shells are double emulsions with an aqueous droplet that is contained inside a bigger liquid crystalline droplet, which is, in turn, dispersed in an aqueous solution. A typical optical micrograph of monodisperse liquid crystal shells produced by microfluidic techniques is shown in Fig. 1.18(a). Chapter 2 and 3 will focus on the construction of different experimental setups and the establishment of necessary dimensional and operational conditions for liquid crystal shell production.

Liquid crystal optics and polarized optical microscopy

Polarizing microscopy allows us to extract information about the director field and characterize topological defects by their charge, as we will discuss in this section.

Because of their long-range orientational order, nematics are optically anisotropic. The optic axis is determined by the director. These optically anisotropic materials are found

to be birefringent: they present two different indexes of refraction corresponding to the different velocities of light propagation. When light enters a nematic sample, it will be broken up into two components, one is referred to as the “ordinary ray” which experiences a refractive index of n_o , and the other one is called the “extraordinary ray” experiences a refractive index of n_e . Let’s consider the case of a nematic sample placed between two crossed polarizers, the linearly polarized light emerging from the first polarizer is oriented at an angle φ with respect to the orientation of n (x-axis), as shown in Fig. 1.19. Because of the birefringence of the nematic, the light coming from the polarizer will be split into two components travelling at different velocities, one component is polarized along the optical axis and the other one in a perpendicular direction, as shown in Fig. 1.19. When the two components emerging from the sample recombine, they form a ray that is elliptically polarized. Now, when this ray reaches the second polarizer (analyzer), there is a component that can pass through and the region appears bright. If the transmission axis of the first polarizer is either parallel or perpendicular to the n , the light is not broken up into two components, and its polarization state does not change. In this case, there is no transmitted component and the region appears dark.

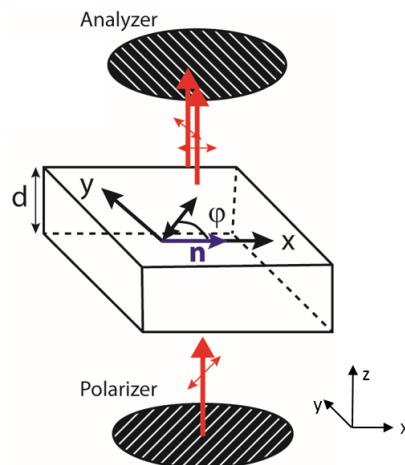


Figure 1.19: Schematic showing a nematic sample is between crossed polarizer and analyzer.

As described before, the defects can be characterized by their topological charge s , which describes the number of 2π -rotations of the director along a path encircling the defect. Experimentally, the charge of topological defects can be determined by analyzing its optical texture between crossed polarizers. Specifically, the topological charge of the defect is given by the number of extinction lines emerging from its core. For instance, $s = +1$ defects are characterized by 4 extinction lines, see Fig. 1.20 (c): since n undergoes a 2π -rotation around the defect, there are 4 directions where n is aligned either with the polarizer or the analyzer, see Fig. 1.20 (a), and thus, four regions where the light is not transmitted. Such optically extinct areas appear in the form of dark brushes because in

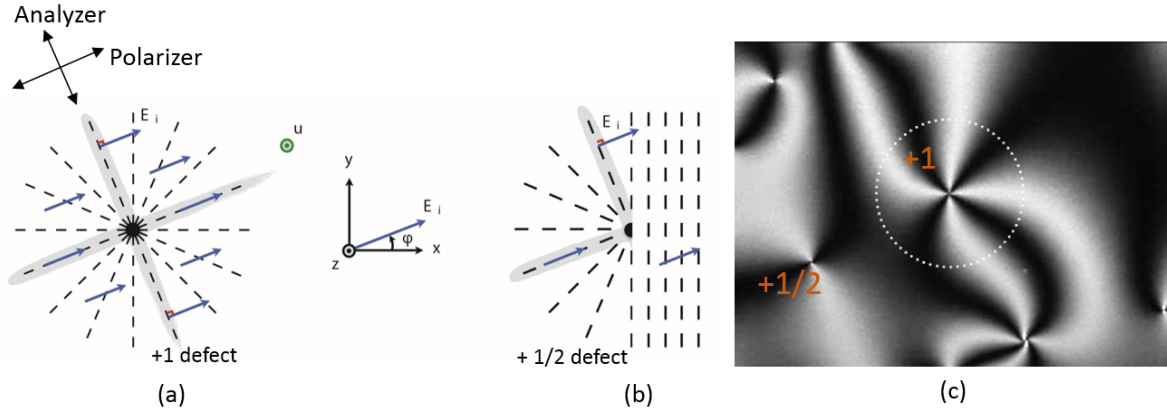


Figure 1.20: Black stripes around topological defects of charge $+1$ (a) and $+1/2$ (b), along and perpendicular to the incident direction of polarization E . (c) Cross-polarized image of typical schlieren texture of a nematic phase under planar anchoring conditions.

the regions further away from the point defect, the bands of molecules aligned with the polarizers are thicker. The same argument explains why $s = +1/2$ defects are characterized by two dark brushes, see Fig. 1.20(b) and (c). The number N of black stripes around a defect is $N = 4|S|$ [87, 149]. Accordingly, defects of charge $+s$ or $-s$ display the same optical texture. To distinguish the sign of the charge, one has to rotate the sample between the crossed polarizers and follow the evolution of the stripes: if the charge is positive (negative), they rotate clockwise when the sample is rotated clockwise (anticlockwise).

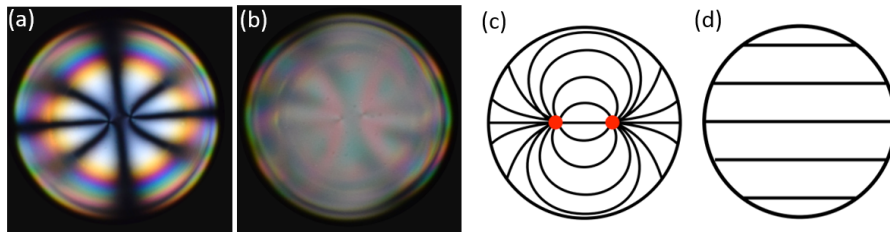


Figure 1.21: (a) and (b): Top-view images of a nematic shell between crossed polarizers. (c) Representation of the director field with two $s = +1$ defects at the top, as seen from above the shell. (d) Uniform director field at the bottom of the shell.

Let's finally consider the birefringent properties of the nematic shell. The optical texture of a typical experimental nematic shell is shown in Fig. 1.21(a). In this particular shell, there are two $s = +1$ boojums on the outer surface; each boojum can be identified by four black brushes. The director field is distorted on the top part around the defects, while it is rather uniform at the bottom, as schematically shown in Fig. 1.21(c) and (d). The

bottom of the shell behaves similarly to the nematic slab described in Fig. 1.19. When the director at the bottom part of the shell is aligned parallel or perpendicular to the incident polarisation, it does not induce any phase shift in the light, and we observe the optical texture of the thin part of the shell, with four black brushes around each defect, see Fig. 1.21(a). However, at other angles, the thick part of the shell introduces an additional phase shift that erases the optical texture characteristic of the defects located at the thin part of the shell, see Fig. 1.21(b). For a clear imaging of the shell texture, we need to place the sample in such a way that the director in the thick part of the shell is aligned either parallel or perpendicular to the polarizer.

1.6.3 Numerical methods

To get a detailed information on the molecular structure within the shell, we have compared our results with numerical simulations. The simulations have been performed by our collaborators from the University of Chicago (de Pablo's group). The calculations rely on a Landau–de Gennes (LdG) continuum model for the tensor order parameter Q , defined by $Q_{ij} = S(n_i n_j - \frac{1}{3}\delta_{ij})$ where n_i are the x, y, z components of the local director vector and S is the scalar order parameter [150]. The scalar order parameter S is given by an ensemble average of the second Legendre polynomials evaluated for the dot product between the molecular orientations and the director.

The total free energy of the system is given by

$$\begin{aligned}
 f = \int_{\text{bulk}} & \left(\frac{A}{2} \left(1 - \frac{U}{3} \right) Q_{ij} Q_{ji} - \frac{AU}{3} Q_{ij} Q_{jk} Q_{ki} \right. \\
 & \left. + \frac{AU}{4} (Q_{ij} Q_{ji})^2 \right) dV \\
 & + \int_{\text{bulk}} \frac{L}{2} \frac{\partial Q_{ij}}{\partial x_k} \frac{\partial Q_{ij}}{\partial x_k} dV + \int_{\text{surf}} W \left(\tilde{Q}_{ij} - \tilde{Q}_{ij}^\perp \right)^2 dS.
 \end{aligned} \tag{1.18}$$

where A and U are material constants. The parameter L represents the elastic constant. We have adopted one elastic constant approximation, indicating that the three basic deformation modes, splay, twist and bend are penalized equally for the systems considered in this thesis. The anchoring strength W ranges from 10^{-7} to 10^{-3} J/m², which are typical values for thermotropic liquid crystal-water interfaces. The elements of the Q tensor are given by $\tilde{Q}_{ij} = Q_{ij} + \frac{1}{3} S_{eq} \delta_{ij}$; \tilde{Q}_{ij}^\perp is the projection of \tilde{Q}_{ij} onto the surface, defined by a surface normal ν_i as $\tilde{Q}_{ij}^\perp = P_{ik} \tilde{Q}_{kl} P_{lj}$. The projection operator is given by $P_{ij} = \delta_{ij} - \nu_i \nu_j$. The first term in Eq. 1.18 represents the short range contributions to the free energy (or phase free energy). That term controls the equilibrium value of the nematic order parameter through $S_{eq} = \frac{1}{4} \left(1 + 3\sqrt{1 - \frac{8}{3U}} \right)$. The second term represents the elastic free energy, which governs long-range director distortions and penalizes elastic deformations from the helical phase in the undistorted bulk. The last term represents the surface energy, which

quantifies deviations from planar degenerate anchoring on both the inner and outer boundaries of the shells.

An iterative Ginzburg-Landau relaxation technique with finite differences on a cubic mesh (with a resolution of 7.15 nm) is implemented to minimize the total free energy. [151] The numerical parameters employed in the simulations are: $A = 1.17 \times 10^5 \text{ J/m}^3$, $U = 5$, $L = 6 \times 10^{-12} \text{ N}$, $W = 10^{-3} \text{ J/m}^2$, the radius of outer sphere is $R = 1 \mu\text{m}$.

To characterize the fine structure of the defects, we rely on a splay-bend parameter S_{SB} constructed from the second derivatives of the order parameter tensor $S_{\text{SB}} = \frac{\partial^2 Q_{ij}}{\partial x_i \partial x_j}$. [152] Assuming that there is no variation of the scalar order ($S = S_{\text{eq}}$) in the director field representation, S_{SB} is given by

$$S_{\text{SB}} = \frac{3S_{\text{eq}}}{2} \nabla(\mathbf{n}(\nabla \cdot \mathbf{n}) - \mathbf{n} \times \nabla \times \mathbf{n}) \quad (1.19)$$

The two terms in Equation 1.19 are related to the splay and bend deformations in the Frank–Oseen director representation [92]. Large positive values of S_{SB} indicate a pronounced splay deformation, while large negative values indicate a significant bend deformation.

Chapter 2

Exploring the limits of standard microfluidic techniques

Introduction

The experimental realization of “superatoms” from liquid crystal shells requires achieving some key milestones. One of these milestones is to be able to produce liquid crystal shells in a colloidal range of size. Until now, liquid crystal shells, with a characteristic size of 100 μm , have been produced by using standard microfluidic methods. In this chapter, we explore the small size limit of these standard microfluidic methods. We will first describe the main mechanisms for the production of single and double emulsions in two-dimensional devices fabricated by soft-lithography. We will, then, introduce axisymmetric glass capillary devices, customarily used for producing liquid crystal shells, and study how the geometry of the device imposes limitations to the size of the produced shells.

2.1 Standard microfluidic techniques for droplet production

Microfluidics is both the science that studies the behavior of fluids through micro-channels, and the technology of manufacturing microminiaturized devices containing chambers and tunnels through which fluids flow or are confined [153]. The microfluidic technology holds great promise due to its ability to use very small quantities of samples and perform typical laboratory operations with high resolution and sensitivity in significantly less time [154, 155]. One subcategory of microfluidics is droplet-based microfluidics [156, 157]. The manipulation of multiphase flows in a specially designed microfluidic device enables the generation and manipulation of droplets of a liquid phase in a continuous liquid stream. Researchers in the field have developed a variety of different droplet formation techniques. The most frequently used microfluidic geometries for droplet production are the so called

“co-flow” [158–160] and “flow-focusing” [161–164].

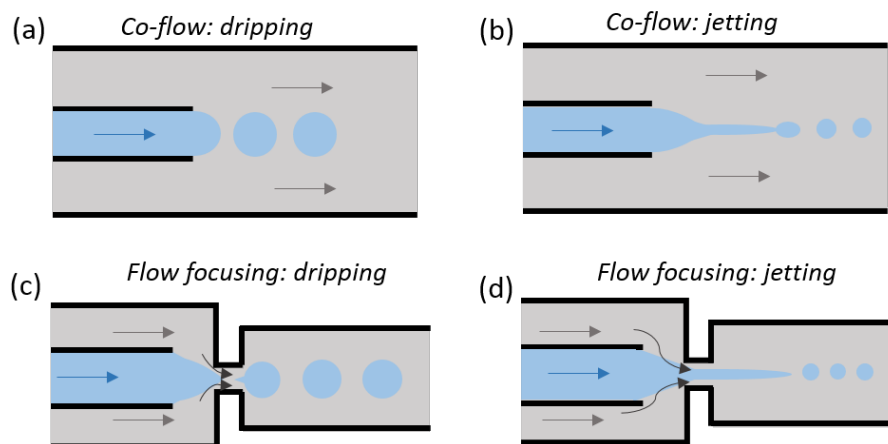


Figure 2.1: Illustration of two main microfluidic geometries used for droplet formation. (a) and (b) show dripping and jetting regimes in a co-flow device. (c) and (d) show dripping and jetting regimes in a flow focusing device. The blue and gray colors represent the dispersed phase and continuous phase, respectively.

In a co-flow geometry, droplets are generated when the dispersed phase is introduced via a channel or capillary into the co-flowing continuous phase. At lower flow rates, drops are formed at the tip of the channel in a process termed dripping, as shown in Fig. 2.1(a), whereas at faster flow rates, the dispersed phase forms a thin jet that breaks into drops downstream, as shown in Fig. 2.1(b).

In the flow-focusing device, shown in Fig. 2.1(c) and (d), the dispersed phase flows through a central channel while the continuous phase flows through two side channels. Those two phases are, then, forced to flow through a narrow orifice. In this geometry, the symmetric shearing forces imposed by the continuous phase on the dispersed one lead to the formation of a narrow thread, which breaks into droplets. In the dripping regime, see Fig. 2.1(c), drops are formed very close to the orifice of the channel. The jetting regime, see Fig. 2.1(d), is characterized by the formation of a jet that eventually breaks into drops further downstream from the orifice. Co-flow and flow-focusing geometries are founded on the same physical principles, with the only difference that, on the latter, the presence of an orifice brings the hydrodynamic focusing effect into play [163].

Most of microfluidic devices are fabricated by soft lithography, using cast-molded stamps made from flexible materials, mainly poly(dimethylsiloxane)(PDMS) due to its simplicity in fabrication, fairly low background fluorescence, and good bio-compatibility [167, 168]. The formation of double emulsions, which are droplets inside droplets, are typically generated in dripping and jetting regimes using microfluidic devices that employ different combinations of basic geometries, including two flow focusing [165, 169, 170], two

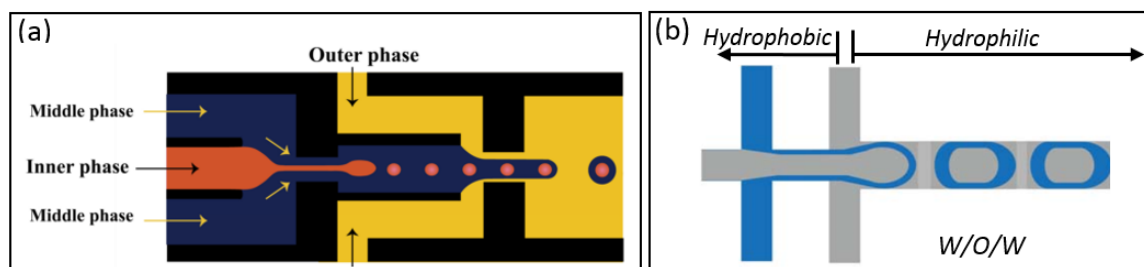


Figure 2.2: (a) Two consecutive flow-focusing drop generators with different wettability for producing core/shell drops. Figure adapted from reference [165]. (b) A poly(dimethylsiloxane) (PDMS) device with hydrophobic and hydrophilic properties in different regions for formation of W/O/W double emulsion. Figure adapted from reference [166].

co-flowing [171], or a combination of co-flow and flow-focusing [172, 173]. In order to controllably produce drops in two-dimensional PDMS devices, it is important to tune the wettability of the channel walls when switching between the generation of W/O and O/W emulsions or for the formation of double emulsions. For instance, Fig. 2.2(a) shows a PDMS device consisting of two consecutive flow-focusing drop makers for the production of double emulsions [165]. The inner and middle fluids are injected in the first drop maker, which is wetted by the middle phase. The outer phase is introduced in the two side inlets in the second drop maker to focus and break the middle phase jet. The double emulsions are formed downstream after the second orifice, which is wetted by the outer fluid. For the formation of W/O/W emulsion, the wettability of the channels needs to be patterned so that the first drop maker is hydrophobic and the second one is hydrophilic [166], as illustrated in Fig. 2.2(b).

PDMS devices can be precisely produced by soft lithography and replicated in large amounts at low cost and with complex channel configurations. However, they have some drawbacks, such as short life-time due to the difficulties in producing wetting patterns that are stable over time, or poor mechanical strength and chemical compatibility with strong organic solvents. [174]. Three-dimensional glass microfluidic devices have recently emerged as an interesting alternative to PDMS devices. Here the fluids flow inside assemblies of coaxial capillaries, which can be assembled in different configurations allowing for co-flow, flow-focusing or a combination of both geometries [148]. These glass microfluidic devices have attracted a lot of attention due to their solvent compatibility, optical properties and precise control of surface wettability. Also, in this axisymmetric device [159, 160, 162, 163], the dispersed phase is completely surrounded by the continuous phase, minimizing the contact of the formed droplets with the channel walls that normally occurs in two-dimensional devices. Both simple and double monodisperse emulsions composed of drops of controllable size can be produced. Glass capillary devices have been intensively used in the last decade to generate monodisperse double emulsions with applications in diverse fields. In

particular, they have been used to produce liquid crystal shells. [175–177].

2.1.1 Fabrication of liquid crystal shells using an axisymmetric glass-capillary device

The most efficient way of producing liquid crystal shells in a glass capillary device is to combine a co-flow with a flow-focusing geometry [148]. This configuration is shown in Fig. 2.3(c), where two tapered cylindrical capillaries are inserted, facing each other, inside a square capillary. Coaxial alignment is achieved by ensuring that the outer diameters of the cylindrical capillaries match the inner dimension of the square one, see the inset in Fig. 2.3(c). In our devices, the cylindrical capillaries have an outer diameter of 1 mm (inner $550\ \mu\text{m}$) and the square ones have an outer dimension of 1.2 mm (inner 1mm).

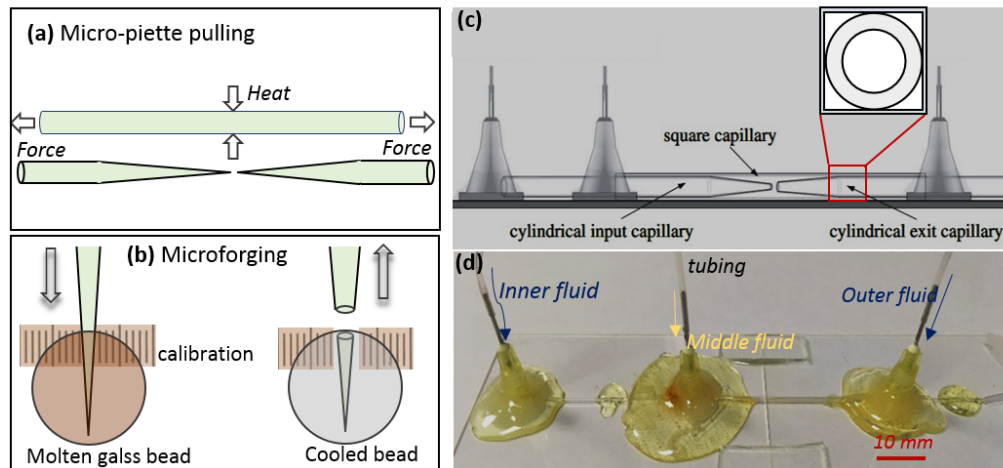


Figure 2.3: Fabrication of tapered-end glass capillaries using a micropipette puller (a) and a microforge (b). Figure (a) and (b) are adapted from reference [178]. (c) Schematic illustration of a glass capillary device showing how the capillaries are assembled inside. The inset is a cross section of the device, showing the coaxial alignment of the square and cylindrical capillaries. Figure adapted from reference [179]. (d) Image of an assembled capillary device ready for use.

The first step in the fabrication of the device consists of tapering off the central part of a cylindrical capillary by using a micropipette puller, see Fig. 2.3(a). In the puller, a heating filament locally melts the capillary at its central part, while pulling the two ends of the capillary away. This results into two shorter capillaries, each of them having a sharp end. Before inserting these two capillaries in the square one, we need to forge their tips to produce orifices of controlled size. This is done by using a microforge, which

is essentially a microscope, equipped with a heating filament whose position is controlled by a micro-manipulator that allows for three-dimensional motion. To produce orifices of controlled diameters, we dip the tip of the capillary in a molten glass bead, which lies on the heating filament of the microforge. We cut-off the immersed part of the tip by pulling the capillary away once the glass has been cooled down, see Fig. 2.3(b). The depth at which the tip is embedded in the glass bead determines the diameter of the tip. For the production of double emulsions, the collection capillary, on the right in Fig. 2.3(c), needs to have an orifice with a radius $R_{collection}$ larger than $R_{injection}$, which is the radius of the orifice of the injection capillary, on the left in Fig. 2.3(c). In a typical device, $R_{collection} = 50 \mu\text{m}$ and $R_{injection} = 25 \mu\text{m}$. In our liquid crystalline emulsions, the middle phase is the thermotropic liquid crystal, an oil-like phase, and thus, we need to treat the injection capillary to make it hydrophobic, for instance using n-octadecyltrimethoxil silane. After silanization, the two cylindrical capillaries are inserted inside the square one, by keeping a certain distance d between their tips. We fix their positions by using epoxy. In our device, three hypodermic needles hubs act as tube connectors for fluids, as shown in Fig. 2.3(d). The needle inputs are connected to syringes using tubing (Fig. 2.3(d)).

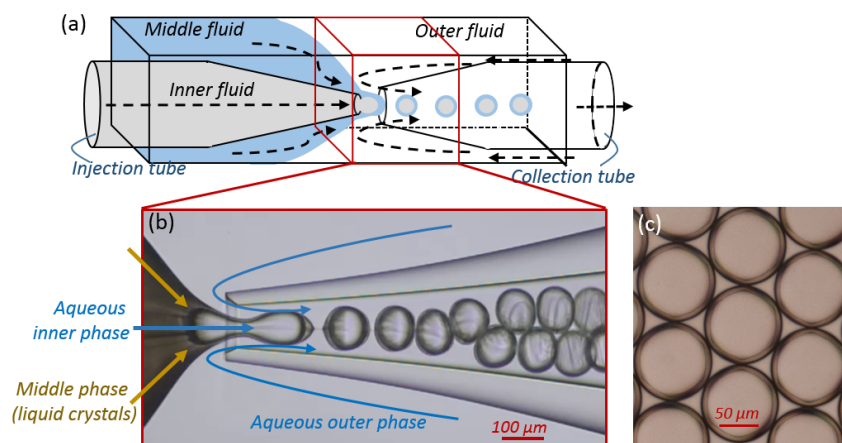


Figure 2.4: (a) Schematic of a glass capillary device that combines co-flow and flow focusing. (b) Production of liquid crystal shells in glass capillary device. (c) Optical micrograph of monodisperse liquid crystal shells.

We use syringe pumps to control the flow rates of the three fluids. The inner fluid is injected through the injection tube, and the middle fluid co-flows through the corner spaces between the cylindrical injection capillary and the square one, which results in a coaxial flow at the exit of the injection tube. The outermost fluid is injected through the outer coaxial region from the opposite direction to flow focus the coaxially flowing fluids, as shown in Fig. 2.4(a). As the three fluids merge near the entrance of the collection capillary, the outer fluid hydrodynamically focuses the inner and middle fluids [161, 180]. The coaxial flow passes through the orifice and subsequently ruptures to form drops due to

a Rayleigh-Plateau instability [181,182]. The production of liquid crystal double emulsions in a glass capillary device is shown in Fig. 2.4(b). The size of the produced droplets is of the order of 100 μm , see Fig. 2.4(c).

The regimes for double emulsion formation are mainly determined by the dimensionless capillary number, Ca , which measures the relative effect of interfacial tension forces with respect to viscous forces, defined as:

$$Ca = \frac{\mu_o U}{\sigma_i + \sigma_m} \quad (2.1)$$

where U is the characteristic fluid velocity, μ_o is the dynamic viscosity of the outer fluid, σ_i is the interfacial tension coefficient between the inner and middle fluids and σ_m represents the corresponding coefficient between the middle fluid and the continuous phase. Above a certain critical capillary number $Ca^* \sim O(1)$, droplet break off occurs [148,183,184]. To set a convenient production regime, it is important to choose fluids with favorable physical properties (surface tension and viscosity) and properly adjust the flow rates. The use of a viscous continuous phase usually facilitates the formation of droplets. For this reason glycerol is frequently added to the outer phase in the production of W/O/W double emulsions [148,173].

It has been established that the relative flow rates play a critical role in the double emulsion production. In the pioneering work by Utada *et al* [148], they show that the dripping and jetting modes appear for different flow rates ratios. If the flow rates of the inner and middle phases, Q_i and Q_m , are fixed, the dripping regime occurs for lower flow rates of the outer continuous fluid, Q_o . In contrast, a high Q_o increases the viscous force at the interface, yielding the formation of a coaxial jet. Further increase in Q_o leads to an elongation and thinning of the coaxial jet, which eventually breaks into smaller double emulsions due to Rayleigh-Plateau instabilities [181,182].

In addition to the flow rate ratios, the orifice sizes of the tapered cylindrical capillaries have a direct impact on the shell diameter. At low flow rate, the shell diameter has been estimated to be close to the orifice size [159]. According to Utada *et al* [148], in the dripping regime, mass flux is approximately proportional to the cross-sectional area, which gives:

$$\frac{Q_i + Q_m}{Q_o} = \frac{\pi(R_{jet})^2}{\pi(R_{collection})^2 - \pi(R_{jet})^2} \quad (2.2)$$

where R_{jet} is the radius of the compound jet near the orifice of the collection tube. In the jetting mode, the size of the double emulsion droplets can be estimated from:

$$R_{drop} = \left(\frac{15(Q_i + Q_m)R_{jet}\mu_o}{\pi\sigma_m} \right)^{1/3} \quad (2.3)$$

Therefore, the size of double emulsions can be predicted from the following parameters: jet size, orifice size, flow rates, interfacial tension and viscosities of the fluids involved. In

the next section, we will establish the limits of this technique in terms of the size of the double emulsions that can be produced, by playing with the flow rates and the geometry of the device.

2.1.2 Device testing through variation of inter-capillary distance

In the dripping regime, the outer radius of the double emulsions, R , is always close to the radius of the orifice, $R_{collection}$. Producing double emulsions in a colloidal range of sizes would imply using capillaries where $R_{collection}$ is of the order of $1 \mu\text{m}$, which is impracticable because of clogging issues. In the jetting regime, in contrast, R is set by the radius of the stretched jet, R_{jet} . In order to produce slender jets, we need to create high velocity gradients in the converging flow. With this aim, we have investigated the effect of increasing Q_o and reducing the inter-capillary distance, d . The devices used for this study have $R_{injection} \simeq 25 \mu\text{m}$, $R_{collection} \simeq 50 \mu\text{m}$ and an inter-capillary distance that varies between $50 \mu\text{m}$ and $350 \mu\text{m}$, approximately, as shown in Fig. 2.5. We used a combination of fluids whose physical properties are similar to those of the fluids used for generating liquid crystal shells. The different fluids used in the experiments, with their densities and viscosities, are listed in Table 2.1. A small amount of dye (Oil-Red O) was added to the middle phase to improve the optical contrast between the oil and aqueous phases.

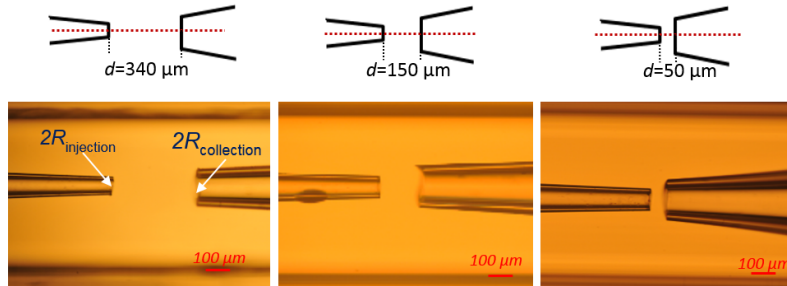


Figure 2.5: The inter-capillary distance d is varied to produce three different configurations, which are tested for double emulsion generation.

Table 2.1: Compositions and physical properties of the three fluids used in the experiments to generate W/O/W double emulsions.

| Fluid | Composition | $\rho(kg\ m^{-3})$ | $\mu\ (cP)$ |
|--------|--|--------------------|-------------|
| Inner | Water | 1000 | 1 |
| Middle | 99wt% Hexadecane + 1wt% Span 80 | 780 | 30 |
| Outer | 19wt% Water + 80wt% Glycerol + 1wt% Tween 20 | 1110 | 38 |

Fig. 2.6(a) shows the effect of increasing the outer flow rate on the size of the double emulsions produced in a microfluidic device with an inter-capillary distance $d = 340 \mu\text{m}$. The experimental points were obtained by varying Q_o from $1200 \mu\text{l/hr}$ to $2400 \mu\text{l/hr}$, while Q_i and Q_m were maintained at $60 \mu\text{l/hr}$. In Fig. 2.6(a), R has been scaled by $R_{\text{collection}}$ and Q_o has been scaled by $Q_{\text{sum}} = Q_i + Q_m$. Fig. 2.6(a) shows that an increase in Q_o considerably reduces both the inner droplet radius a and the outer droplet radius R . The reduction in droplet size as a result of increasing Q_o can be explained by an increase in the viscous stress exerted by the outer fluid to the compound jet, which reduces the drop formation time and thus, increases the droplet generation frequency, resulting in smaller radii [185]. Over the range of flow rates studied, in which the device is operative, the outer drop radius decreased from 45 to $28 \mu\text{m}$, while the inner drop decreased from 25 to $15 \mu\text{m}$.

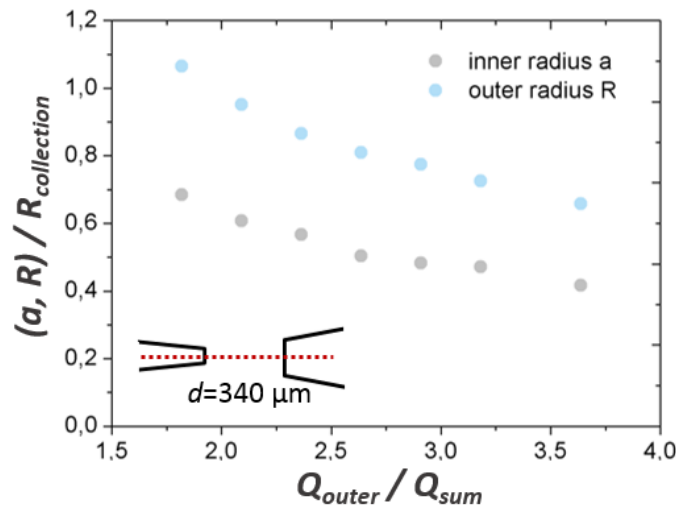


Figure 2.6: Inner and outer drop radii as a function of Q_o / Q_{sum} for double emulsions generated in a device with $d = 340 \mu\text{m}$. Q_i and Q_m are maintained at $180 \mu\text{l/hr}$ and $480 \mu\text{l/hr}$, respectively, whereas Q_o is varied from $1200 \mu\text{l/hr}$ to $2400 \mu\text{l/hr}$.

As the geometry of the device changes, the flow rates have to be re-adjusted to achieve stable regimes for double emulsion production. The device with $d = 150 \mu\text{m}$ led to a range of sizes similar to that obtained with the previous device, as shown in Fig. 2.7. The regime for double emulsion production was obtained for Q_o values between $3000 \mu\text{l/hr}$ and $5100 \mu\text{l/hr}$, while keeping $Q_i = Q_m = 600 \mu\text{l/hr}$. Over this flow rate ratio range, the outer drop radius decreased from 43 to $29 \mu\text{m}$, while the inner drop decreased from 28 to $16 \mu\text{m}$.

Interestingly, the range of sizes was considerably enlarged when $d = 50 \mu\text{m}$, see Fig. 2.8. In this case, the regime for double emulsion production was obtained for Q_o values between $300 \mu\text{l/hr}$ and $1100 \mu\text{l/hr}$, while keeping $Q_i = Q_m = 60 \mu\text{l/hr}$. Over this range,

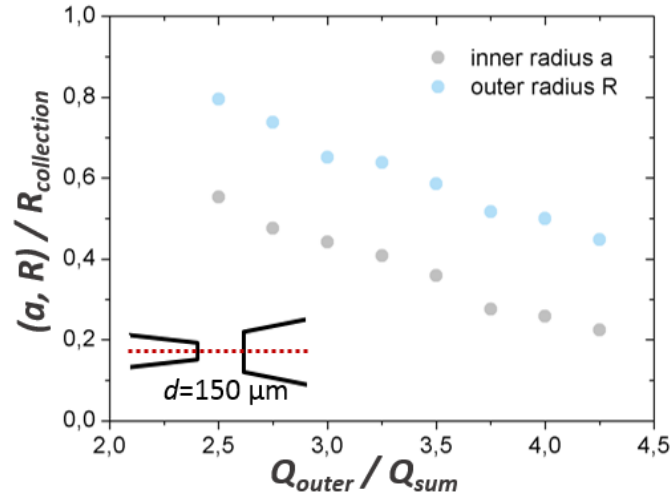


Figure 2.7: (a) Inner and outer drop radii as a function of Q_o / Q_{sum} for double emulsions generated in device with $d = 150 \mu\text{m}$. Both Q_i and Q_m are maintained at $600 \mu\text{l/hr}$, whereas Q_o is varied from $3000 \mu\text{l/hr}$ to $5100 \mu\text{l/hr}$.

the average outer drop radius decreased from 60 to $25 \mu\text{m}$, while the inner drop decreased from 42 to $15 \mu\text{m}$.

To compare the three geometries, Fig. 2.9 shows the range of a values (gray) and R values (blue) produced with the different devices as a function of the inter-capillary distance. While reducing d from $350 \mu\text{m}$ to $150 \mu\text{m}$ does almost not impact the sizes of the produced double emulsions, making $d = 50 \mu\text{m}$ considerably widens the possible values for the double emulsion inner and outer radius. However, the smaller double emulsions produced in this latter geometry are larger than those produced in the devices with larger inter-capillary distances. This could be explained by the model developed by Nabavi *et al* [185] for the generation of double emulsions in glass capillary devices. An increase in the distance between two capillaries causes the compound jet to slow down before it enters the collection tube. Therefore, the magnitude of the inertial force of the middle phase decreases compared to the interfacial force at the outer interface, which causes a reduction in size. From the data in Fig. 2.9, we can conclude that both the inner and outer radii of the double emulsions are mainly set by $R_{injection}$ and $R_{collection}$. In the most favorable configuration, the smaller double emulsion size is $0.5 D_{collection}$, which means a strong limitation in the production of colloidal double emulsions.

To push the glass capillary microfluidic technique to its working limits, we have designed a device in which $R_{injection}$ and $R_{collection}$ have very small values: $R_{injection} = 5 \mu\text{m}$ and $R_{collection} = 30 \mu\text{m}$. In this device the injection capillary has been inserted inside the

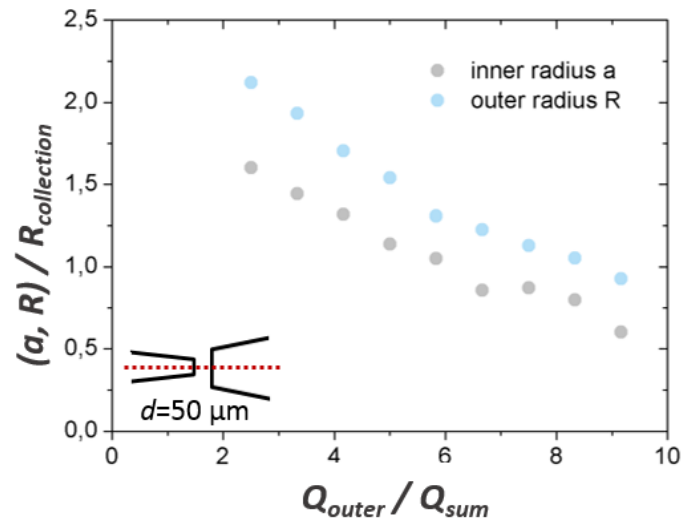


Figure 2.8: (a) Inner and outer drop radii as a function of Q_o / Q_{sum} for double emulsions generated in device with $d = 50 \mu\text{m}$. Both Q_i and Q_m are maintained at $60 \mu\text{l/hr}$, whereas Q_o is varied from $300 \mu\text{l/hr}$ to $1100 \mu\text{l/hr}$.

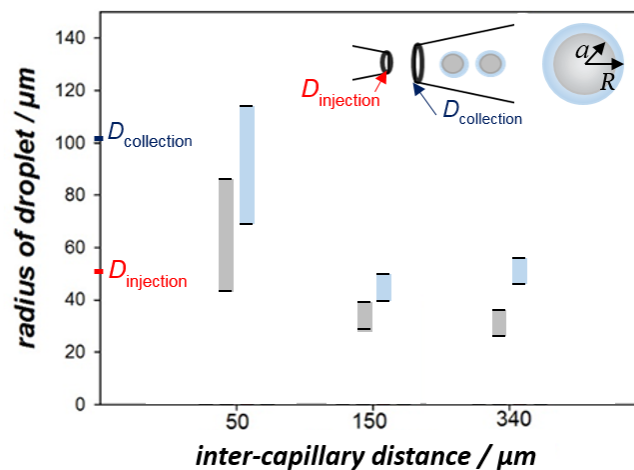


Figure 2.9: Ranges of values for the inner (grey color) and outer (blue color) radii of the double emulsions produced in glass capillary devices with different inter-capillary distances.

collection one, as shown in Fig. 2.10(a). In this geometry, the formation of double emulsion occurred only for a few combinations of the flow rates. Fig. 2.10(b) shows the double

emulsions produced when $Q_i = 120 \mu\text{l/hr}$, $Q_m = 120 \mu\text{l/hr}$ and $Q_o = 700 \mu\text{l/hr}$, which have an inner radius of $20 \mu\text{m}$ and an outer radius of $35 \mu\text{m}$. By increasing Q_o from 700 to $1200 \mu\text{l/hr}$ while maintaining inner and middle flow rates constant, a and R can be reduced to 10 and $18 \mu\text{m}$ respectively, as shown in Fig. 2.10(c). To scale the double emulsions further down to micrometric or sub micrometric dimensions, it might be possible to design devices made of capillaries with even smaller dimensions. For practical purposes, however, the production of emulsions with diameters below a few tens of microns is not possible, since the risk of clogging increases when narrowing the diameters of the orifices. The alignment of capillaries is also more difficult to achieve.

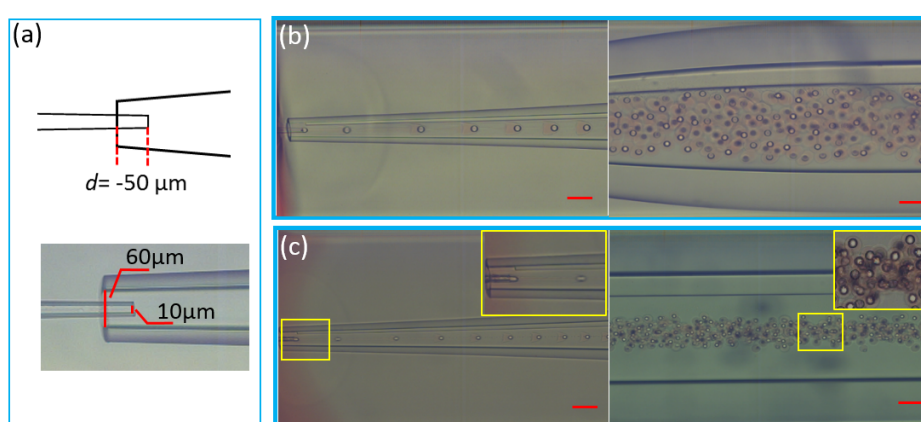


Figure 2.10: (a) Schematic (top) and snapshot (bottom) of a glass capillary device with a configuration in which the injection tube is inserted inside the collection tube by a distance of $50 \mu\text{m}$, with $R_{injection} = 5 \mu\text{m}$ and $R_{collection} = 30 \mu\text{m}$. (b) W/O/W double emulsion generation with inner, middle and outer phase flow rates set respectively at 120, 120 and $700 \mu\text{l/hr}$. (c) W/O/W double emulsion generation with inner, middle and outer phase flow rates set respectively at 120, 120 and $1200 \mu\text{l/hr}$. Scale bar, $50 \mu\text{m}$.

2.2 Conclusion

In this chapter we have described the experimental methods typically employed to produce liquid crystal shells and investigated in which the range of size they can be produced. We found that standard microfluidic techniques, such as glass capillary devices, allow us to produce shells in a controlled and flexible way, but they do not allow for a large scale variation of the shell diameter. New production techniques need to be developed to reduce the shell size to the colloidal level.

Chapter 3

Towards the production of micro-sized liquid crystal shells using pressure gradients

Introduction

Glass capillary devices enable the generation of monodisperse double emulsions in a controlled manner, however, this standard microfluidic technique does not allow for decreasing the shell diameter to the colloidal scale (submicron range). In this chapter, we review the microfluidic emulsification methods for the production of simple and double microemulsions, relying on generating highly stretched thin fluid jets with diameters in the micrometer/nanometer range by the action of either electrical forces or pressure gradients. We then implement and adapt the "Confined Selective Withdrawal" (CSW) technique for the production of liquid crystal shells. We explore the limits of the production regimes and test the validity of the scaling laws established for regular liquids. We show that the technique allows us to produce shells with a diameter that can be easily reduced to scales of the order of 10 microns, or even smaller, at higher frequencies.

3.1 New microfluidic techniques for droplet production

3.1.1 Micro- and nanoflows driven by electrical forces

Some techniques resort to the use of electrical stresses to stretch a stream of a conducting liquid to generate coaxial jets of immiscible liquids with diameters in the range of micrometer/nanometer sizes [180, 186–188].

In the electrospray (ES) technique, a conductive liquid is slowly injected through an electrified capillary tube. For appropriate values of the flow rate and the electric voltage applied between the capillary tube and a grounded electrode, the meniscus at the tube exit adopts a conical shape. Taylor explained the conical shape of the meniscus as a balance between electrostatic and capillary forces, since then such a liquid cone has been known as Taylor cone [189]. When a certain threshold voltage is reached, a thin microthread of liquid emerges from the tip of the Taylor cone, which will eventually break up forming a spray of highly charged droplets [190]. The experimental setup for the production of coaxial-jet electrosprays is sketched in Fig. 3.1(a) [180]. Two concentric needles are immersed in a dielectric host medium. The outer conductive (red) liquid is injected through the gap between the two needles while the inner (blue) liquid is injected through the inner needle. The outer needle is connected to an electrical potential of several kilovolts relative to a ground electrode. For a certain range of values of the electrical potential and flow rates, a structured Taylor cone is formed at the exit of the needles with an outer meniscus surrounding the inner one. The electrical shear stress acting on the interface drags the outer conductive liquid towards the cone vertex and sets it into motion. A steady jet then issues from the vertex. The meniscus at the end of the inner needle is deformed by the converging motion of the outer liquid and develops a steady state spout that evolves into a jet which flows coaxially with the outer liquid jet. Due to capillary instabilities, the coaxial jet breaks up at some point downstream giving rise to compound droplets, as shown in Fig. 3.1(a).

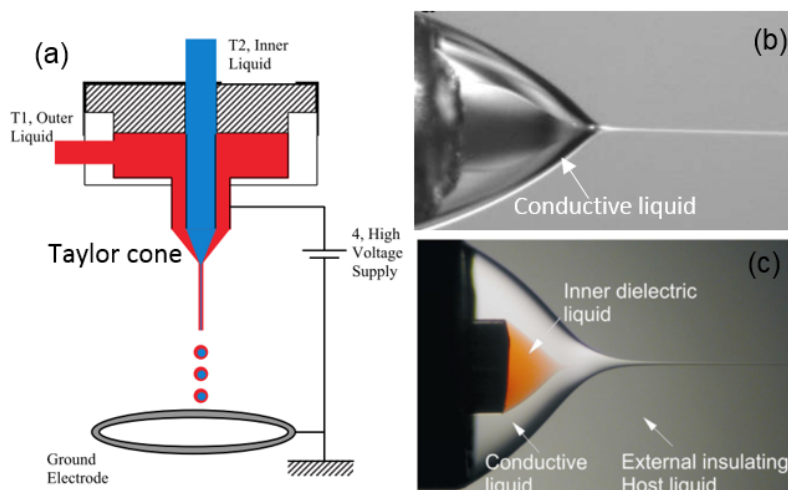


Figure 3.1: (a) Typical experimental setup for the formation of a structured Taylor cone. (b) Compound Taylor cone. Figure (a) and (b) adapted from [180]. (c) Compound meniscus and the coaxial jets. Figure adapted from [191].

Loscertales and co-workers reported a method to generate steady coaxial jets of immiscible liquids with diameters in the range of micrometer/nanometer size, see Fig. 3.1(b),

the eventual jet breakup results in an aerosol of monodisperse compound droplets [180]. Marn *et al* reported the generation of electrified coaxial jets of micrometric diameter in liquid media, as shown in Fig. 3.1(c), double (oil/water/oil) emulsions of typical sizes of the order of $1 \mu\text{m}$ can be obtained by this approach [191]. In this technique, the size of the droplets is not limited by the geometry of the injection needle. If the middle fluid conductivity is enhanced up to sufficiently high values, it is possible generate droplets with diameters down to the submicron range. However, its inevitable dependency on the electrical properties of the liquid greatly limits the physical-chemical parametric freedom of the method. In particular, the production of water/oil/water double emulsions, as it is the case for most of liquid crystal shells, seems quite challenging.

3.1.2 Microflows driven by pressure gradients

Some other approaches resort to the use of pressure gradients in order to obtain highly stretched micro-jets [192], which subsequently give rise to the formation of microdrops [193, 194], microbubbles [193–195] and micro-sized double emulsions [184], thanks to the action of capillary instabilities [160, 196, 197].

One of the earliest implementations of this type of flow is the so-called selective withdrawal [198–200]. The simplest version of this technique is schematically shown in Fig. 3.2(a): the tip of a tube of diameter D is located at a height H above an interface separating two immiscible, density-separated liquids. By applying a steady suction, only the upper fluid is sucked through the tube. An increase in the suction leads to a transition where the lower liquid is also withdrawn in the form of a steady-state thin jet of diameter d being much smaller than D . The capillary breakup of this jet gives rise to a stream of droplets with a mean diameter of the order of that of the jet. For a given pair of liquids and a given D , there are two controlling parameters: the pressure drop across the orifice, Δp , which controls the flow rate Q of the upper fluid, and the injected flow rate q of the lower fluid. For a given value of q , the increase of Δp results in a thinner jet.

Another implementation of this type of flow [158, 201] is displayed in Fig. 3.2(b), where a pressure drop Δp across a thin plate with an orifice of diameter D provokes the converging motion of the focusing fluid. A focused fluid is injected at a flow rate q through a tube of diameter D_t , whose end is located at a distance H in front of the orifice, $D_t \sim H \sim D$. For a given value of H , and an appropriate range of values of q , the liquid forms a conical-shape drop held by surface tension and attached to the edge of the capillary end. The resulting meniscus is stretched by a pressure drop ΔP through the focusing orifice until a tiny liquid jet is emitted. Eventually the jet give rise to a chain of nearly uniform drops.

In a recent experimental and theoretical study, Evangelio *et al* demonstrated that the pressure gradients can be employed for the production of micro-sized simple and double emulsions with controllable diameters at given frequencies [184]. The microfluidic device,

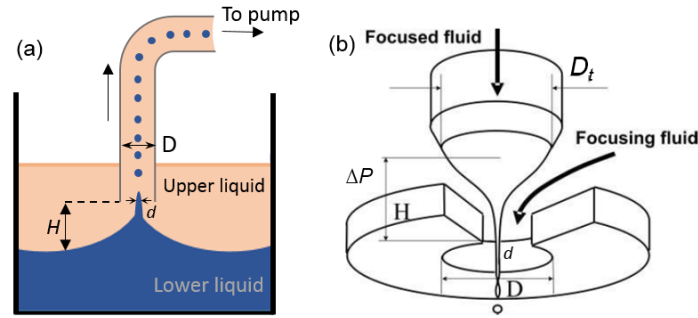


Figure 3.2: (a) A schematic of the apparatus used in selective withdrawal. (b) A schematic of the experimental flow-focusing setup. Figure adapted from [201].

sketched in Fig. 3.3(a), has a geometrical arrangement that shares similarities with both selective withdrawal [200] and flow focusing geometries [158]. In their experimental device, a cylindrical injection needle ① and a square extraction capillary ② are inserted into a pressurized chamber ③. The injection needle is aligned with the axis of the square capillary and separated by a distance H . An outer liquid ④, constituting the continuous phase, flows into the chamber with a pressure P_o larger than atmospheric, P_a . The imposed pressure difference $P_o - P_a$ fixes the mean liquid velocity U in the square tube and also generates a pressure gradient from the exit of the injection needle towards the entrance of the extraction duct.

In the case of generation of simple emulsions, see Fig. 3.3(a), the circulation of the outer liquid, from the chamber to the exterior through the extraction capillary, produces the suction of the inner fluid. The suctioned liquid forms a capillary jet and narrows down downstream, to reach a constant micrometer-sized diameter due to the action of the co-flowing outer liquid and the favorable pressure gradient that it produces. This simple jet breaks up, due to capillary instability, into droplets of the same order of magnitude as that of the jet, to produce a simple monodisperse micrometer-sized emulsion.

To generate double emulsions, a coaxial needle through which two concentric fluids (inner and middle fluid) are injected is used, see Fig. 3.3(b). Similar to what occurs with simple emulsions, the suction produces a coaxial capillary jet composed of the middle fluid, which forms the outermost layer of the jet, and the inner fluid, which is at the center. Likewise, the action of the outer co-flow and the favorable outer pressure gradient, jointly with the capillary pressure gradients exerted by the middle flow, lead to the formation of an inner fluid capillary jet which, due to capillary instability, breaks up into droplets. That induces the break-up of the middle fluid, and consequently, the formation of double emulsions.

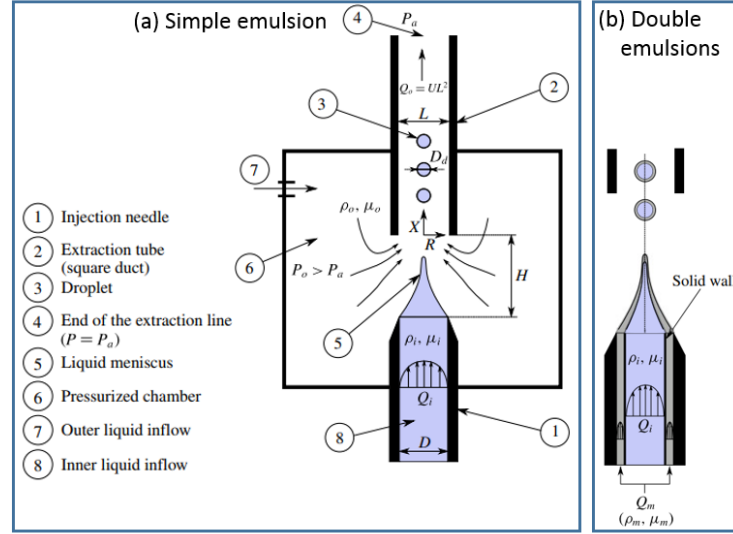


Figure 3.3: (a) Sketch of the microfluidic device, where an injection needle and a square extraction capillary are immersed into a pressurized chamber, for the production of simple emulsion. (b) Sketch illustrating the case of generation of double emulsions, where a coaxial injection needle through which two liquids are injected is used. Figure adapted from [184].

In [184], it has shown that monodisperse-sized double emulsions of newtonian liquids can be formed in a periodic way if the Reynolds number characterizing the flow of the continuous phase, Re_o , is of the order of unity or smaller,

$$Re_o = \frac{\rho_o UL}{\mu_o} \leq O(1) \quad (3.1)$$

Moreover, the generation of stable coaxial jets from which compound drops are produced requires that

$$Ca = \frac{\mu_o U}{\sigma_i + \sigma_m} > Ca^*(\lambda_i, q) \quad (3.2)$$

where σ_i is the interfacial tension coefficient between the inner and middle fluids, σ_m represents the corresponding coefficient between the middle fluid and the continuous phase, Ca^* is the critical capillary number above which long steady jets are produced, $\lambda_i = \mu_i/\mu_o$ is the ratio of viscosities between the inner and outer fluids and q denotes the flow rate ratio,

$$q = (Q_i + Q_m)/Q_o \quad (3.3)$$

with $Q_o = (L^2 U)$. For values of the viscosity ratio $\lambda_i \sim O(10^{-3})$ and of the flow rate ratio $q \ll 1$, it is found that the value of the critical capillary number is such that $Ca^* \sim O(1)$ [184].

The geometrical configuration of this technique, called *confined selective withdrawal* (CSW), is conceptually similar to that for the generation of electrified coaxial jets [180,191],

but dispenses with the use of electric fields, making possible the use of a larger number of fluids. The CSW technique, which enables effective and stable production of micro-sized simple and double emulsions, is a promising approach for the generation of micro-sized liquid crystal shells.

3.2 Implementation of CSW technique for the production of liquid crystal shells

3.2.1 Design and construction of the setup

Our experimental setup for the production of liquid crystal shells, inspired by the design in reference [184], is displayed in Fig. 3.4. The setup consists of: a) pressure system, which comprises an air source, pressure regulators, manometers and pressurized reservoirs, b) an injection system which comprises syringe pumps and designed injection lines for fluids, c) an optical system which comprises a combination of halogen light sources, cameras and an objective lens, and d) the fabrication parts of the setup, which comprise a pressurized chamber and a coaxial injection needle. The microfluidic setup is placed on a micrometric positioning plate. Images and videos are captured using a Phantom V711 high-speed camera, which operates between 4000 and 10000 frames s^{-1} .

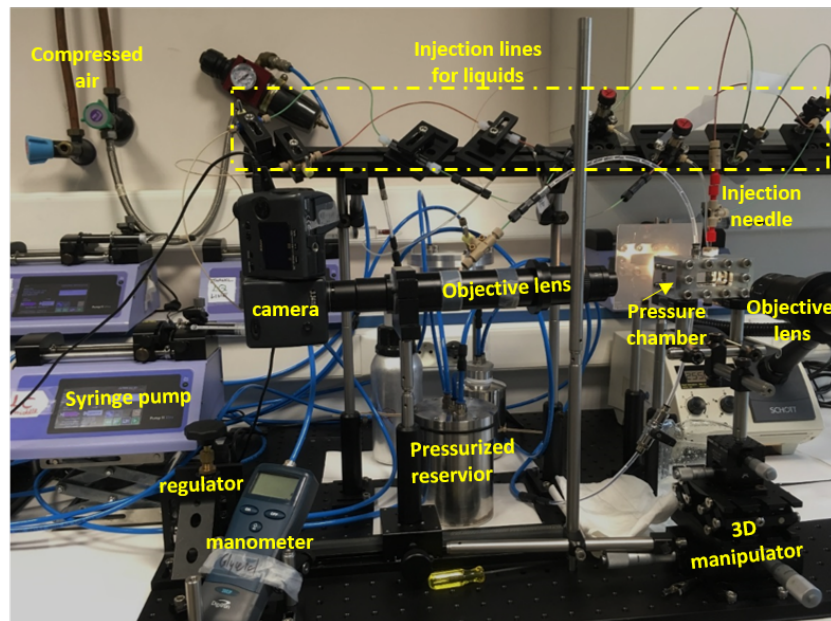


Figure 3.4: Photograph of the experimental setup for the production of nematic liquid crystal shells.

Pressurized chamber

One of the important pieces in the setup is the high-pressure chamber. We have designed the chamber as an assembly of aluminum and glass pieces with inner dimensions of $2 \times 2 \times 7$ cm, see Fig. 3.5.

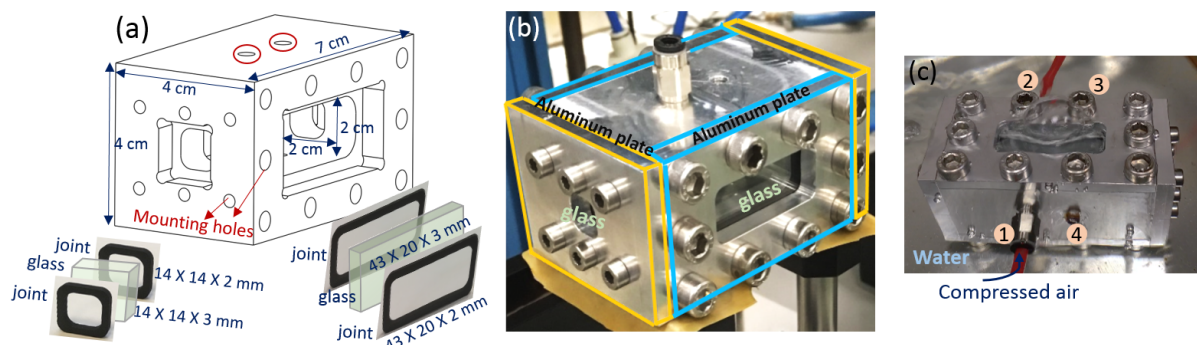


Figure 3.5: (a) Schematic of the chamber and the sealing components (glass and joints). (b) Photograph of assembled aluminum chamber. (c) Test of the chamber sealing.

The body of the chamber, see Fig. 3.5(a), has mounting holes for laterally attaching 4 aluminum plates and two pairs of windows, one pair is located in the front and back sides of the chamber and the other one is located on the left and right sides of the chamber. The top and the bottom parts of the chamber are designed to have two orifices, respectively, as marked in red circles in Fig. 3.5(a), in order to be used as inlets and outlets. Two pairs of glass slides (3 mm-thick), are used as glass windows, allowing for macroscopic observation, see the schematics in Fig. 3.5(a). Rubber joints are placed between the glass and metal walls to protect the glass and to seal the chamber. Two pairs of aluminum plates, highlighted in yellow and blue in Fig. 3.5(b), are screwed to the chamber to hold the glass slides and joints.

After the assembly, we test the sealing of the chamber. We completely block three of the orifices (②, ③ and ④ in Fig. 3.5(c)) and immerse the chamber into a water bath, as shown in Fig. 3.5(c). We test the sealing of the assembly by observing whether there is any leakage when air is injected into the chamber through the orifice ①. In order to obtain a good chamber sealing, each of the aluminum plates should be properly set up, all the cap screws should be installed symmetrically and tightened firmly. It should be mentioned that each component used to assemble the chamber must be cleaned with Milli-Q water, ethanol and acetone before the installation. The pressure chamber is especially suited for manipulation in the range from 0 to 5 Bar (0-500 KPa).

Coaxial needle

A coaxial steel needle is used to inject both the inner and middle fluids. It is composed of an inner capillary tube, which has a diameter $d_i = 0.4$ mm and a length of 12.5 cm, and an outer tube, which has a diameter $d_o = 1.1$ mm and a length of 5 cm. The inner capillary tube is centered inside the outer one, as schematically represented in Fig. 3.6(a). The coaxiality is assured by the presence of a spring that is wrapped around the inner tube, see the cross-section of the needle in Fig. 3.6(b). The coaxially aligned tubes are then equipped with fittings and T-connectors to enable the injection of the inner liquid through the inner tube and the injection of the middle fluid through the outer tube, as shown in Fig. 3.6(c). A square glass capillary tube, with an inner dimension of 1 mm and a length of 3.8 cm, is used as the extraction tube to collect the samples, see Fig. 3.6(d).

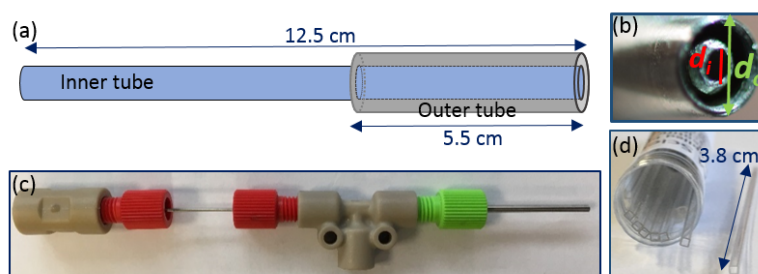


Figure 3.6: (a) Schematic illustrating a coaxial injection needle composed of an inner tube, which is coaxially centered inside a second outer tube. (b) Cross-section of the coaxial stainless needle with an inner diameter d_i and outer diameter d_o . (c) Assembled injection needle with fittings and T-connector. (d) Square glass capillary tube with an inner dimension of 1 mm and a length of 3.8 cm.

Connections

The function of the four inlets/outlets of the chamber are indicated in Fig. 3.7(a): the inlet ① enables to fill the chamber with the continuous phase, while the outlet ② is used to exact the air bubbles that are formed when the chamber is being filled. On the right side of the chamber, inlets ③ and ④ enable the connection of the injection needle and collection tube, respectively. The injection needle is equipped with a ferrule and fitting, as shown in Fig. 3.7(b), to enable its insertion into the chamber through the inlet ③. In this way, we could install the needle and adjust its position in a flexible way. Before inserting the assembled injection needle, we run water, and then ethanol through it for at least 15 minutes. Then we blow air through the needle for 5 minutes to remove any possible dust. To connect the capillary tube to the chamber, we use a segment of tygon tube whose inner diameter matches the outer dimension of the square capillary to prevent it from sliding among the fitting, see Fig. 3.7(c). Teflon is used to wrap together the capillary and the

fitting and to avoid leakage. After that, the complete assembly of square glass capillary is inserted into the chamber through orifice ④. The injection needle is co-axially aligned with the extraction tube, both being separated by a distance H . The coaxial alignment is assured by checking the front view and side view using two independent cameras, as shown in Fig. 3.7(d)-(f).

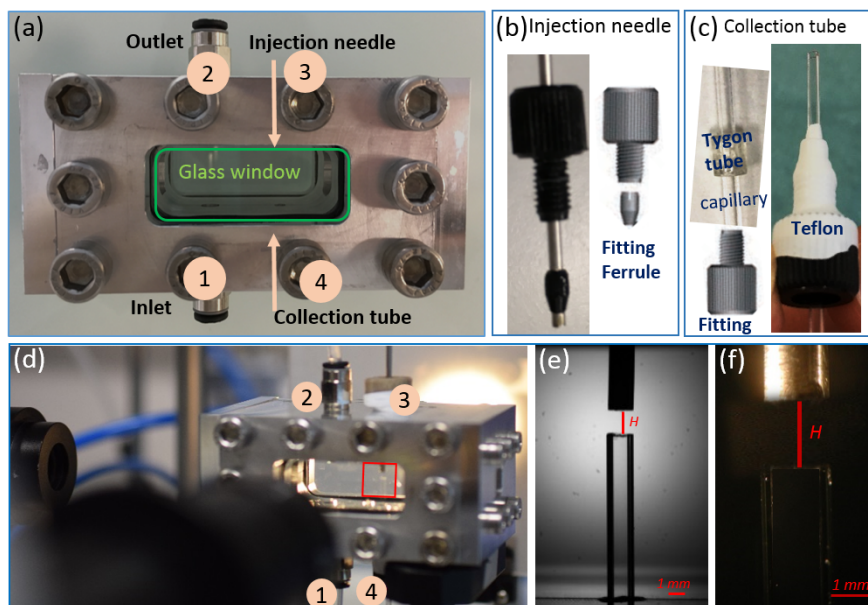


Figure 3.7: (a) Inlets and outlets of the chamber. (b) Injection needle equipped with a fitting and a ferrule. (c) Assembly of square extraction tube. (d) Two-axes objective lens that allows to image the coaxial alignment of injection needle and collection tube. Front view (e) and side view (f) of the alignment.

3.2.2 Controlled injection of outer, middle and inner fluids

Outer fluid injection: filling the chamber

To generate liquid crystal shells, the chamber is firstly filled with the outer fluid. The outer fluid is supplied from a pressurized reservoir. The precise control of the flow rate of outer fluid is achieved by using a high precision air pressure regulator and a manometer, as schematically shown in Fig. 3.8(a). A viscous outer liquid flows into the chamber at a low working pressure of 150 mbar, in order to avoid air bubbles and let the outer fluid completely wet the chamber inner walls. During the filling process, the injection of the inner and middle fluids were imposed at a pressure of 400 mbar in order to fill the feeding lines, but the injection inlets are temporally closed. The air bubbles formed when the chamber is filled are evacuated through the tubing connected to outlet ②. This connection is closed using a valve, see the inset in Fig. 3.8(b), once the chamber is completely

filled without any air bubbles. In our experiment, the high-pressure chamber was fixed on a mounting stage so that its position could be manipulated in the three dimensions, by using a XY-axis manipulator and a mounting platform with a smooth vertical adjustment range, as shown in Fig. 3.8(c). The mounting system allows us to have a fine tuning of the position of the chamber and to track the objects inside the chamber. In addition, in order to remove the air bubbles from the chamber in an easy and flexible way, we also used a goniometer (Fig. 3.8(c)), which allows us to rotate the chamber precisely, within a small angular range, about a fixed point in space.

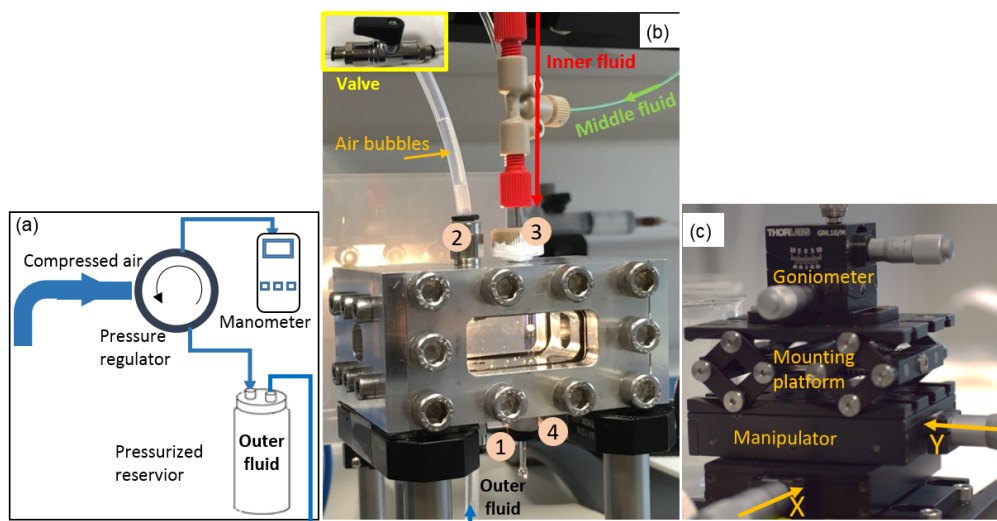


Figure 3.8: (a) Schematic diagram of the pressure-controlled liquid supply for filling the chamber. (b-c) Photographs of the experimental setup: (b) The high-pressure chamber is filled with the outer fluid. (c) 3D mounting system.

Inner and middle fluids injection: forming the coaxial jet

In order to have a fine control on the flows of the inner and middle fluids, we have designed feeding lines for both the inner (red line) and middle fluids (green line), as schematically shown in Fig. 3.9.

The inner and middle fluids supplied from the pressurized tanks are routed through a series of valves and PEEK tubing before entering into the injection needle. A shut-off valve, shown in Fig. 3.9(a), is used to stop the flow stream when the chamber is being refilled and to restart it right after the chamber is completely filled with the outer fluid. Additionally, a back pressure regulator holder, highlighted in Fig. 3.9(b), is used to restrict the flow to one direction, preventing the inner or middle fluid from flowing backwards under high outer

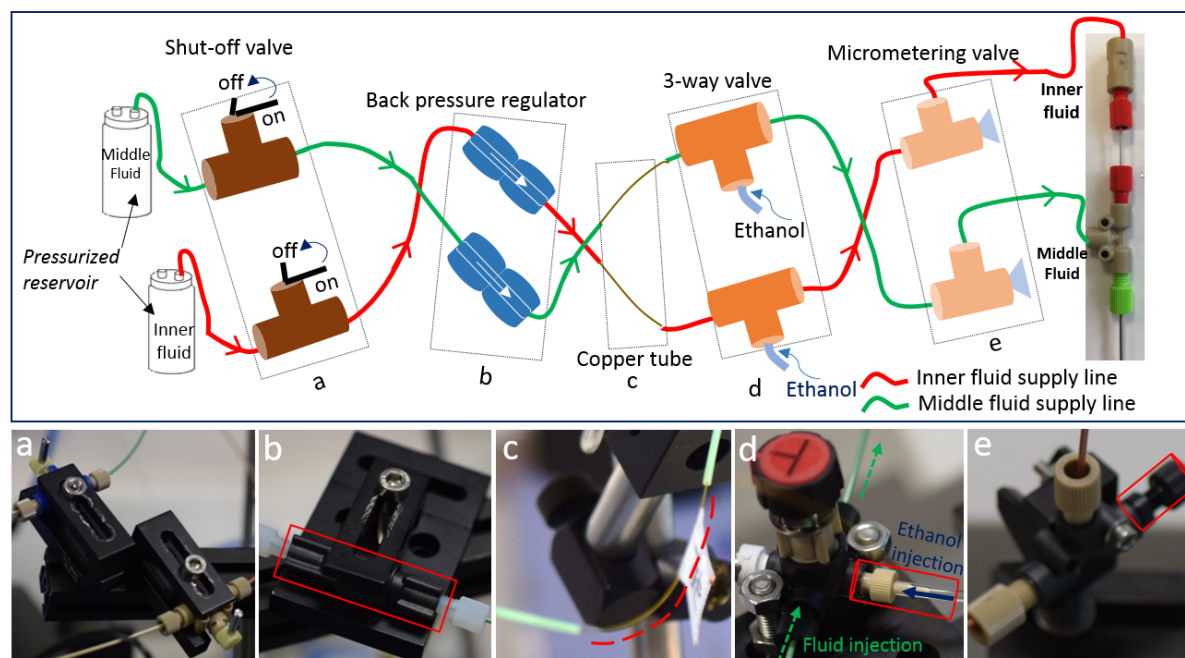


Figure 3.9: Schematic diagram of inner fluid and middle fluid feeding lines. (a) Shut-off valve. (b) Back pressure regulator holder. (c) Thin copper tube. (d) 3-way flow manual switching valve. (e) High pressure micrometering valve.

pressure working conditions. A large pressure drop ΔP is introduced in both the inner and middle feeding lines by inserting a thin copper tube with inner dimension of $100 \mu\text{m}$ along the PEEK tube, as shown in Fig. 3.9(c). This makes possible to have a precise control on pressure when tuning the regulators and to avoid fluctuations of the resulting flow rate. A 3-way flow manual switching valve is used after the pressure-drop, as shown in Fig. 3.9(d). This valve is specially designed for cleaning the injection needle with ethanol since the needle inevitably gets contaminated by the highly viscous outer fluid, and thus needs to be cleaned after the experiments. Using such a valve eliminates the need to remove, plug and reconnect adapters and tubing, which increases the flexibility of manipulation. For fine control on the flow rates, we also placed a high pressure micrometering valve, see Fig. 3.9(e), for both inner and middle fluids before the injector. By manipulating a thumbscrew, highlighted in red in Fig. 3.9(e), we can reduce the outgoing fluid flow rate much more slowly and finely than by directly manipulating the pressure regulators.

3.2.3 Operational conditions for the production of nematic shells

Before establishing the operational conditions of our microfluidic setup, let us summarize how it works and which are the relevant physical parameters involved. It mainly consists

of a pressurized chamber where a coaxial injection needle and a square extraction capillary are inserted facing each other, as sketched in Fig. 3.10. Two immiscible fluids, inner and middle are injected, at respective flow rates Q_i and Q_m through the coaxial needle, which is aligned with the axis of the extraction capillary of width L . The injection needle and extraction capillary are separated by a distance $\sim O(L)$. A flow rate Q_o of an outer liquid with density, ρ_o and viscosity, μ_o , constituting the continuous phase, and immiscible with the intermediate fluid, flows into the chamber, where the pressure P_o is larger than atmospheric, P_a . The imposed pressure difference $P_o - P_a$ fixes the mean velocity U at the square extraction tube, and also generates a pressure gradient from the exit of the injection tube towards the entrance of the extraction duct, favoring the downstream stretching of the coaxial liquid ligament. The resultant monodisperse nematic shells have an inner diameter D_i , outer diameter D_o and an average thickness $h = (D_o - D_i)/2$.

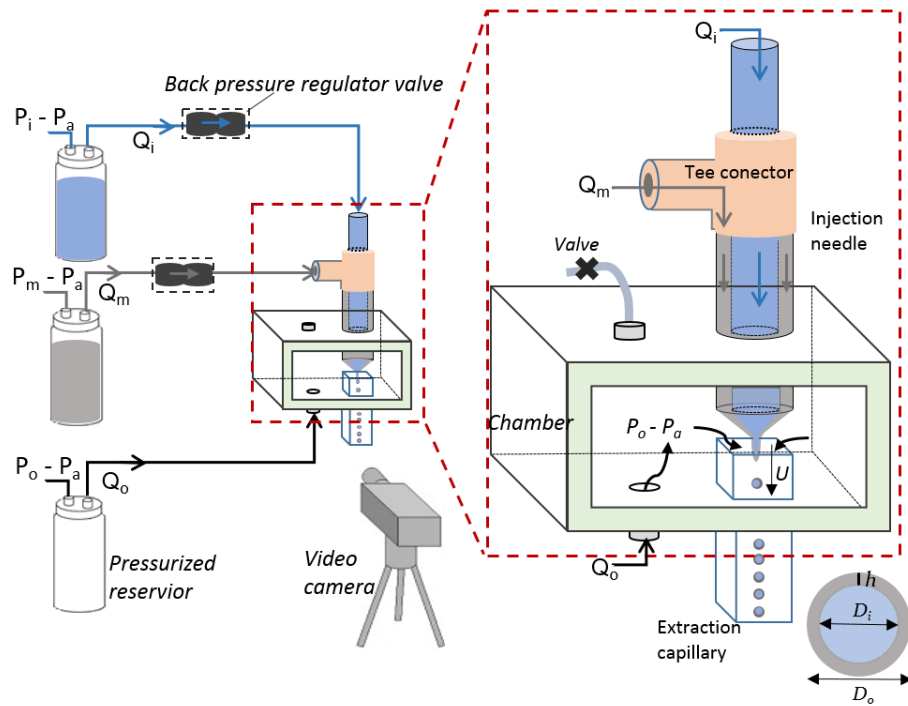


Figure 3.10: Sketch of the experimental setup for the production of nematic liquid crystal shells.

Physio-chemical properties of the fluids

The production of double emulsions is subject to the requirements expressed in equations 3.1 and 3.2, which impose certain limitations to the Reynolds and capillary numbers. Additionally, the surface tensions at the inner-middle (σ_{i-m}), middle-outer (σ_{m-o}), and

inner-outer (σ_{i-o}) interfaces need to satisfy certain conditions to guarantee the stability of the double emulsions. In order to avoid the appearance of Marangoni stresses associated to the axial gradient of the interfacial tension coefficient, we decided not to use surfactants. Indeed, Marangoni flows, which are difficult to control, interact with those originated by capillary pressure gradients and, therefore, alter the periodic production of monodisperse nematic shells from the capillary breakup of the jet.

Even in the absence of surfactants, the stability of the double emulsions can be guaranteed if the following condition is fulfilled:

$$\sigma_{i-o} > \sigma_{i-m} + \sigma_{m-o}, \quad (3.4)$$

Indeed, if condition 3.4 is fulfilled [202], in the case that a “hole” appears in the shell isolating the inner drop from the outer fluid, the action of the interfacial tension σ_{i-o} , which overcomes the sum of the interfacial tension σ_{i-m} and σ_{m-o} , would tend to close such “hole”, avoiding the the inner fluid to be expelled from the shells, see figure 3.11.

In order to satisfy the conditions expressed in 3.1, 3.2 and 3.4, we need to select a combination of fluids with suitable physico-chemical properties. The liquid crystal used is 5CB, which is customarily used, since it has a nematic phase at room temperature and its physico-chemical properties are well known. Its chemical structure has been introduced in chapter 1, section 1.6. For this liquid crystal, the conditions 3.1 and 3.2 can be simultaneously met when pure glycerol is chosen as the outer fluid because of its large viscosity. Fluorinated oil was used as the inner liquid due to the fact that, with this choice, $\sigma_{i-m} \simeq 7 \times 10^{-3} \text{N m}^{-1}$, $\sigma_{m-o} \simeq 19 \times 10^{-3} \text{N m}^{-1}$, and $\sigma_{i-o} \simeq 29 \times 10^{-3} \text{N m}^{-1}$ and, therefore, the condition given by equation 3.4 is also fulfilled. The physical properties of all the liquids used in this experimental study are provided in Table 3.1.

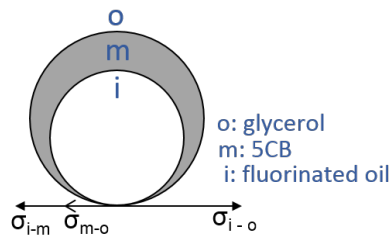


Figure 3.11: Sketch showing the force balance at the interface in the case of the inner drop contacting the outer fluid.

Suitable ranges for $P_o - P_a$, $P_m - P_a(Q_m)$, $P_i - P_a(Q_i)$

In our experiments, the outer fluid, glycerol, supplied from the pressurized reservoir, always fixes the pressure difference $P_o - P_a$ between the pressurized chamber and the atmosphere.

Table 3.1: Compositions and physical properties of the three fluids used in the experiments to generate liquid crystal shells.

| Fluid | Composition | $\rho(kg\ m^{-3})$ | $\mu\ (cP)$ |
|--------|-----------------------|--------------------|-------------|
| Inner | Fluorinated oil | 1614 | 0.77 |
| Middle | Liquid crystals (5CB) | 1008 | 30 |
| Outer | Glycerol | 1270 | 1000 |

The flow rates of fluorinated oil and 5CB, i.e. Q_i and Q_m , are controlled either by syringe pumps or by the imposed pressure $P_i - P_a$ and $P_m - P_a$. Pump control is suitable for comparing with theory, because it provides us with the values of Q_i and Q_m , while pressure control is better for stabilizing the meniscus since it eliminates the perturbations introduced by the pump motors. In both cases, we have performed experiments to find the regime we are interested in. The details on how the setup works and the suitable ranges of the control parameters are provided below.

In the pressure-control case, the outer working pressure $P_o - P_a$ is 150 mbar when refilling the pressurized chamber with the outer fluid, glycerol. As we mentioned, the injection of the inner fluid (fluorinated oil) and middle fluid (5CB) were imposed but temporally closed during the refilling process. Once the chamber is completely refilled, the injection of the two fluids are restarted while $P_o - P_a$ is maintained at 150 mbar. Middle pressure $P_m - P_a$ is then increased from the initially imposed 400 mbar to 1500 mbar abruptly so that 5CB can completely wet the intersection space between the two tubes. Simultaneously, the outer pressure $P_o - P_a$ is increased from 150 mbar to 400 mbar until a steady capillary jet of 5CB is formed. Then we maintain the outer pressure $P_o - P_a$ and middle pressure $P_m - P_a$ constant, while increasing the inner pressure $P_i - P_a$ to 1000 mbar in order to form an inner capillary jet. Due to capillary instability, the fluorinated oil capillary jet breaks up into droplets, which flow downstream in a wide 5CB capillary jet, see the captured image in Fig. 3.12(a). The generation of fluorinated oil droplets inside the 5CB jet causes the interface between 5CB and glycerol to deform. By increasing $P_o - P_a$ in a gradual manner to 1000 mbar, the deformation grows and eventually causes the 5CB jet to break up as a consequence of the action of the co-flowing glycerol and the increasing pressure gradient that it exerts on 5CB, thereby forming monodisperse liquid crystal shells, as shown in Fig. 3.12(b).

When syringe pumps are used for the injection of the fluorinated oil and 5CB, the flow rates of inner, Q_i and middle fluids, Q_m , are tuned to produce a stable coaxial jet, which subsequently gives rise to the formation of liquid crystal shells. Both Q_i and Q_m are set at a large flow rate of 10 ml/hr but the injection is temporally stopped during the refilling process at $P_o - P_a = 150$ mbar. Once the chamber is refilled, the injection of fluorinated oil and 5CB are restarted and a wide coaxial jet is formed. $P_o - P_a$ is then slowly increased from 150 mbar to 500 mbar while Q_i and Q_m are maintained. In such a way, the initial coaxial jet gets thinner. After that, $P_o - P_a$ is continuously increased to a value of 800

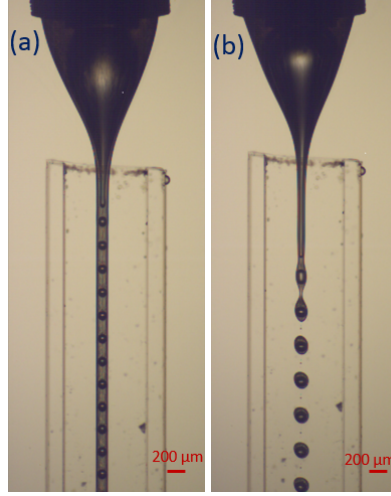


Figure 3.12: (a) Snapshot showing inner droplet formation in the middle fluid capillary jet when $P_i - P_a = 1000$ mbar, $P_m - P_a = 1500$ mbar and $P_o - P_a = 400$ mbar. (b) Snapshot showing the generation of liquid crystal double emulsions after the break-up of the middle capillary jet by increasing $P_o - P_a$ from 400 to 1000 mbar, while $P_i - P_a$ and $P_m - P_a$ were maintained at 1000 and 1500 mbar respectively.

mbar in a gradual manner. Simultaneously, both Q_i and Q_m are decreased to 5 ml/hr. The coaxial jet breaks up into shells with larger diameters. Then, by decreasing Q_i , Q_m respectively to $Q_i = 1$ ml/hr, $Q_m = 2.5$ ml/hr and additionally increasing $P_o - P_a$ to 1000 mbar (1bar), shells with smaller diameters and good monodispersity are formed.

In order to confirm whether the dimensionless parameters, $Ca = \mu_o U / (\sigma_i + \sigma_o)$ and $Re_o = \rho_o U L / \mu_o$ at a given flow rate ratio $q = (Q_i + Q_m) / Q_o$ with $Q_o = L^2 U$ satisfy the conditions 3.1 and 3.2 in our experiments, we have measured the mean velocity U for every set of P_o , Q_i , and Q_m . The velocity is measured as the displacement of the shells along the collection tube d divided by the considered time interval: $d / N \Delta t$, where N is the number of frames between the initial and final positions of the shell and $1 / (\Delta t)$ is the camera frame rate. The experimental values of capillary number and Reynolds number as a function of $q = (Q_i + Q_m) / L^2 U$ are plotted in Fig. 3.13(b), which shows that the continuous production of shells only take place when $Ca > 1$ and $Re_o \leq 1$.

3.3 Size and thickness of the produced double emulsions

The inner D_i and outer diameters D_o of the nematic liquid crystal shells can be modulated by varying the different flow rates (pressures): Q_i ($P_i - P_a$), Q_m ($P_m - P_a$) and Q_o ($P_o - P_a$). Fig. 3.14 shows the influence of varying $P_o - P_a$ (Q_o) on the production of nematic shells.

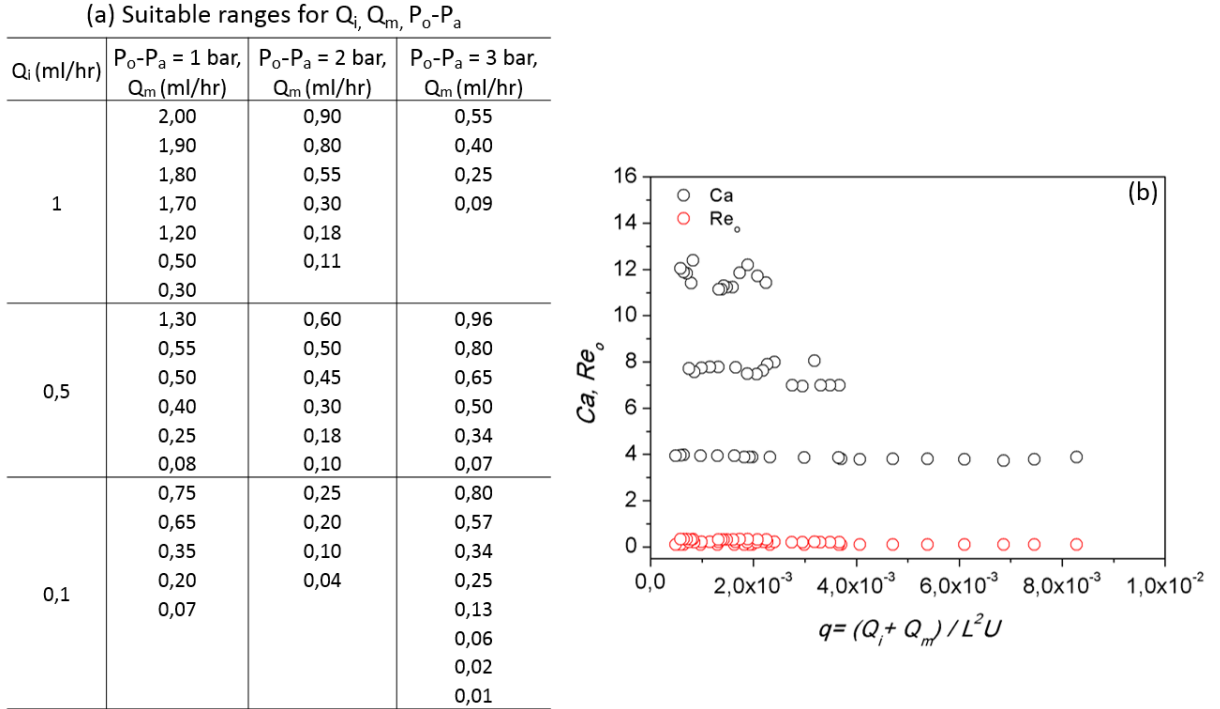


Figure 3.13: (a) Suitable ranges for $P_o - P_a$, Q_m , Q_i for the production of liquid crystal shells. (b) Experimental values of the capillary number (black symbols) and Reynolds number (red symbols) as function of the flow-rate ratio.

We observe that the diameter of the coaxial jet decreases for increasing values of $(P_o - P_a)$. The nematic shells result from the capillary break up of the coaxial jet, and therefore, their outer diameter D_o is set by the jet diameter. By sufficiently increasing $(P_o - P_a)$, we are able to produce shells with D_o values below $10 \mu\text{m}$, approaching the colloidal range of sizes, as it can be seen in Fig. 3.15. Additionally, D_o can be controlled by varying either Q_i or Q_m for fixed $(P_o - P_a)$. We observe that an increase in either Q_i or Q_m , leads to the formation of droplets with increasing values of the outer diameter, D_o , see Fig. 3.16. Fig. 3.17 (a)-(c) also reveals that, for a fixed value of Q_i , the thickness of the nematic shell, h , can be decreased by decreasing Q_m . By making Q_m sufficiently small, we have been able to produce very thin shells, with $h \simeq 1 \mu\text{m}$, see Fig. 3.17 (d)-(f). Next section is devoted to study how D_o , D_i and the shell production frequency, f , depend on the control parameters Q_i , Q_m and $P_o - P_a$.

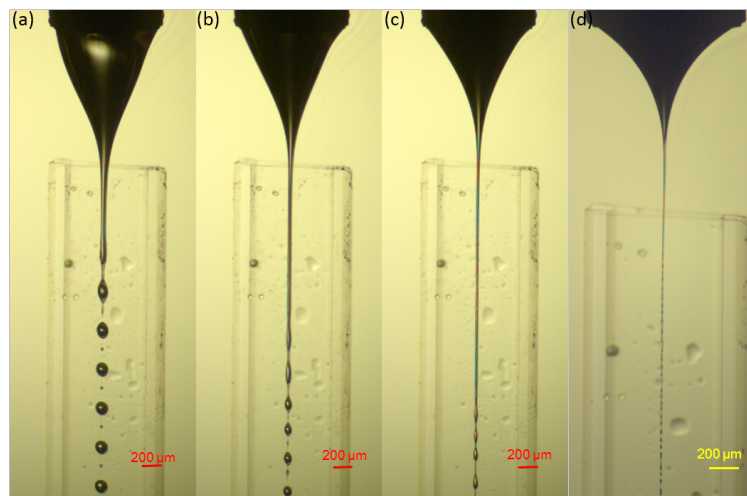


Figure 3.14: Effect of the pressure difference ($P_o - P_a$) on the generation of liquid crystal shells. Here, the inner and middle flow rates are controlled using syringe pumps. (a-c): $Q_i = 1$ ml/hr, $Q_m = 0.5$ ml/hr, $\lambda_i = 7.7 \times 10^{-4}$. (a) $P_o - P_a = 500$ mbar, $q = 0.012$, $Re_o = 0.044$, $Ca = 1.35$. (b) $P_o - P_a = 1$ bar, $q = 0.005$, $Re_o = 0.1$, $Ca = 3.07$. (c) $P_o - P_a = 2$ bar, $q = 0.002$, $Re_o = 0.19$, $Ca = 5.78$. (d) $Q_i = 0.05$ ml/hr, $Q_m = 0.025$ ml/hr, $P_o - P_a = 3.5$ bar, $q = 2.8 \times 10^{-4}$, $Re_o = 0.36$, $Ca = 11.15$.

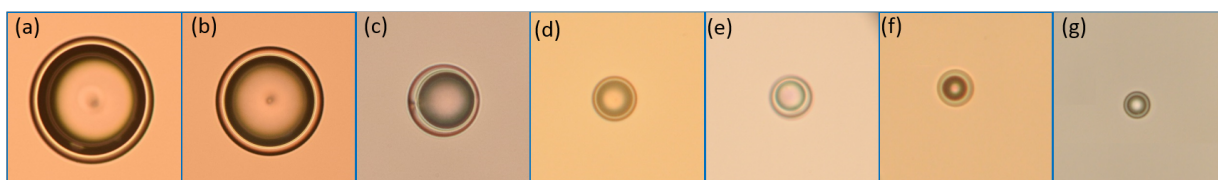


Figure 3.15: Bright-field images of 5CB shells. (a) $q = 4.8 \times 10^{-3}$, $q_i = 3.47 \times 10^{-3}$, $Ca = 3.07$, $Re_o = 0.1$, $D_o = 112 \mu\text{m}$, $h = 8 \mu\text{m}$. (b) $q = 1.8 \times 10^{-3}$, $q_i = 9.26 \times 10^{-4}$, $Ca = 5.76$, $Re_o = 0.19$, $D_o = 96 \mu\text{m}$, $h = 7 \mu\text{m}$. (c) $q = 3.4 \times 10^{-4}$, $q_i = 1.85 \times 10^{-4}$, $Ca = 5.76$, $Re_o = 0.19$, $D_o = 46 \mu\text{m}$, $h = 6 \mu\text{m}$. (d) $q = 2.4 \times 10^{-4}$, $q_i = 4.79 \times 10^{-5}$, $Ca = 11.15$, $Re_o = 0.36$, $D_o = 20 \mu\text{m}$, $h = 2 \mu\text{m}$. (e) $q = 1.25 \times 10^{-4}$, $q_i = 3.47 \times 10^{-5}$, $Ca = 15.3$, $Re_o = 0.504$, $D_o = 14.5 \mu\text{m}$, $h = 2.5 \mu\text{m}$. (f) $q = 1.04 \times 10^{-4}$, $q_i = 2.7 \times 10^{-5}$, $Ca = 15.3$, $Re_o = 0.5$, $D_o = 10.5 \mu\text{m}$, $h = 1.75 \mu\text{m}$. (g) $q = 8.68 \times 10^{-5}$, $q_i = 4.34 \times 10^{-5}$, $Ca = 12.3$, $Re_o = 0.4$, $D_o = 8.5 \mu\text{m}$, $h = 1.2 \mu\text{m}$. Here, $h = (D_o - D_i)/2$ indicates the thickness of the nematic shell.

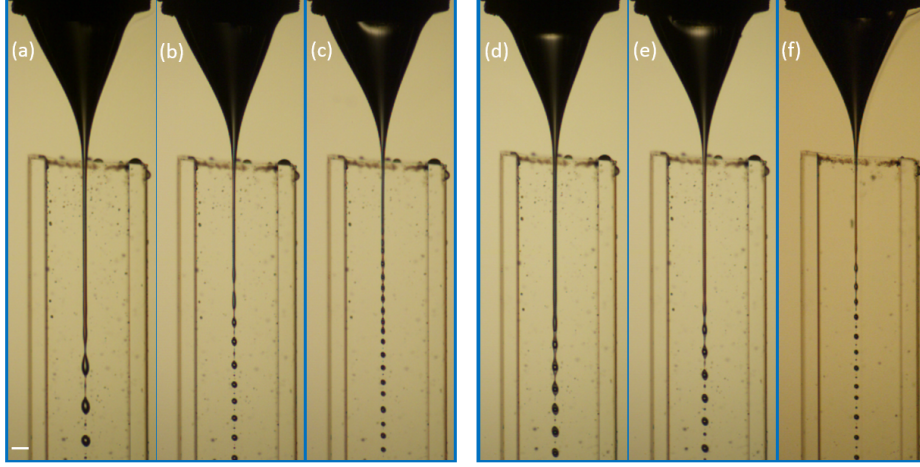


Figure 3.16: (a-c) Effect of varying Q_i for fixed $P_o - P_a = 1$ bar, and $Q_m = 0.25$ ml/hr ($Ca = 3.07$, $Re_o = 0.1$). (a) $Q_i = 1$ ml/h, (b) $Q_i = 0.1$ ml/hr and (c) $Q_i = 0.01$ ml/hr. (d-f): Effect of varying Q_m for fixed values of $P_o - P_a = 1$ bar and $Q_i = 0.1$ ml/hr, ($Ca = 3.07$, $Re_o = 0.1$). (d) $Q_m = 0.9$ ml/hr, (e) $Q_m = 0.5$ ml/hr and (f) $Q_m = 0.4$ ml/hr. The scale bar indicates $200 \mu\text{m}$.

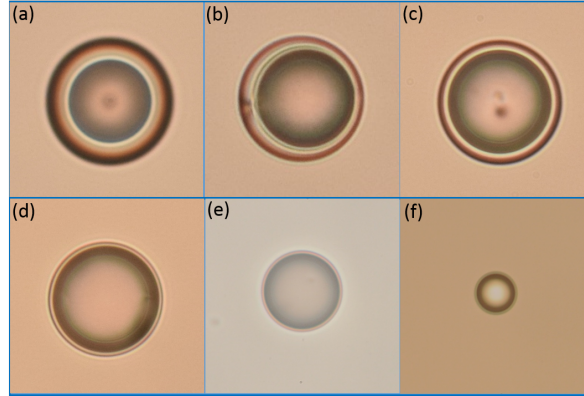


Figure 3.17: (a-c): Optical images of 5CB shells produced when $P_o - P_a = 2$ bars, $Q_i = 0.1$ ml/hr and Q_m is varied. (a) $Q_m = 0.12$ ml/hr, $q = 3.82 \times 10^{-4}$, $q_i = 1.85 \times 10^{-4}$, $D_o = 43 \mu\text{m}$, $h = 6.5 \mu\text{m}$. (b) $Q_m = 0.1$ ml/hr, $q = 3.47 \times 10^{-4}$, $q_i = 1.85 \times 10^{-4}$, $D_o = 46 \mu\text{m}$, $h = 5.5 \mu\text{m}$. (c) $Q_m = 0.08$ ml/hr, $q = 3.33 \times 10^{-4}$, $q_i = 1.85 \times 10^{-4}$, $D_o = 46 \mu\text{m}$, $h = 4 \mu\text{m}$. In figures (d)-(f), the values of the control parameters are: (d) $Q_i = 0.1$ ml/hr, $Q_m = 0.07$ ml/hr, $P_o - P_a = 2$ bars, $q = 2.86 \times 10^{-4}$, $q_i = 1.68 \times 10^{-4}$, $D_o = 42 \mu\text{m}$, $h = 1.5 \mu\text{m}$. (e) $Q_i = 0.08$ ml/hr, $Q_m = 0.03$ ml/hr, $P_o - P_a = 3$ bars, $q = 1.625 \times 10^{-4}$, $q_i = 1.18 \times 10^{-4}$, $D_o = 32 \mu\text{m}$, $h = 1.5 \mu\text{m}$. (f) $Q_i = 0.08$ ml/hr, $Q_m = 0.08$ ml/hr, $P_o - P_a = 4$ bars, $q = 1.04 \times 10^{-4}$, $q_i = 5.55 \times 10^{-5}$, $D_o = 16 \mu\text{m}$, $h = 2 \mu\text{m}$.

3.4 Scaling laws for the shell diameter and shell production frequency

3.4.1 Linear dependence between $P_o - P_a$ and U

Since the Reynolds number characterizing the flow in the extraction tube verifies the condition $Re_o \leq 1$, the flow rate at the extraction tube $Q \simeq Q_o = UL^2$, where, as already

stated, U is the mean velocity of the outer liquid in the extraction tube, is expected to depend linearly on $P_o - P_a$. Indeed, Poiseuille's equation relating the flow rate with the pressure drop along a pipe, yields:

$$UL^2 \simeq \frac{\pi L^4}{128 \mu_o} \frac{P_o - P_a}{L_T} \rightarrow U \simeq K \frac{L}{\mu_o} (P_o - P_a) \quad (3.5)$$

with $K = \frac{\pi}{128} \frac{L}{L_T} \simeq 6.5 \times 10^{-4}$.

where the square tube has been approximated by a cylinder of diameter $L = 10^{-3}$ m and length $L_T = 3.8 \times 10^{-2}$ m. To deduce equation 3.5, it has been taken into consideration that the flow rate $Q_o \gg (Q_i + Q_m)$, being this the reason why equation 3.5 is independent of both Q_i and Q_m , see reference [184] for more details.

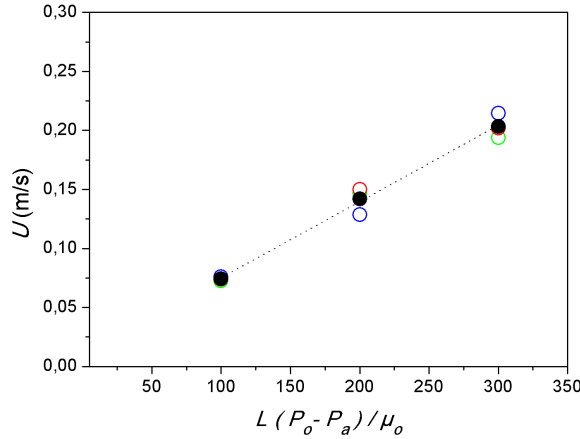


Figure 3.18: The velocity of the liquid at the center of the extraction capillary, U , depends linearly on the pressure difference $P_o - P_a$, as expected from the fact that $Re_o < 1$. The blue, red, and green circles represent, respectively a fixed Q_i at 0.1 mh/hr, 0.5 mh/hr, and 1 mh/hr.

To investigate whether equation 3.5 is satisfied in our experiments, we have plotted the experimental values of the mean velocity U as a function of $L(P_o - P_a)/\mu_o$. Each point in Fig. 3.18 has been calculated from a suitable production regime provided in Fig. 3.13(a). For every set of values $(P_o - P_a, Q_i, Q_m)$, we measured a velocity $U(P_o - P_a, Q_i, Q_m)$. If we consider Q_i and Q_m negligible with respect to $Q_o(P_o - P_a)$, we can average $U(P_o - P_a, Q_i, Q_m)$ with respect to Q_i and Q_m . The points obtained in this way are represented by black symbols in Fig. 3.18. We find a linear relationship, with a proportionality constant $K = (6.46 \pm 0.17) \times 10^{-4}$ and a regression coefficient $R^2 = 0.998$, which validates our assumption and the use of equation 3.5. If we average $U(P_o - P_a, Q_i, Q_m)$ only with respect to Q_m , we obtain a slight dispersion in the $U(P_o - P_a, Q_i)$ values, as

shown in Fig. 3.18 by color open symbols. We conclude that the mean velocity in the extraction capillary, U , is proportional to the pressure difference. Then, from now on, we will express the expected scaling laws for the drop production frequencies and drop diameters as a function of U instead of the variable $P_o - P_a$.

3.4.2 Production frequency f

To predict the production frequency of nematic shells, f , we first need to calculate the normalized radius of the inner jet $r_\infty = R_\infty/L$, where R_∞ is the radius of the emitted jet, in a region located in the extraction capillary far downstream, where the compound jet is cylindrical. For that purpose, we make use of the continuity equation for the inner fluid, taking advantage of the fact that Q_i results from the addition of the flow rate corresponding to an uniform velocity profile with a value $\simeq 2U$ (which is the velocity of the outer fluid at the axis of the extraction capillary), plus the flow rate corresponding to the Poiseuille velocity profile induced by the pressure gradient in the extraction capillary [184]:

$$\begin{aligned} q_i &= \frac{Q_i}{UL^2} = [2 - 8r_\infty^2] \pi r_\infty^2 + 4 \frac{\pi r_\infty^4}{\lambda_i} \simeq 2\pi r_\infty^2 + 4 \frac{\pi r_\infty^4}{\lambda_i} \Rightarrow \\ \Rightarrow r_\infty &= \left[\frac{\lambda_i}{4} \left(-1 + \sqrt{1 + \frac{4q_i}{\pi \lambda_i}} \right) \right]^{1/2}, \end{aligned} \quad (3.6)$$

with the fact that $\lambda_i = \mu_i/\mu_o = 7.7 \times 10^{-4} \ll 1$ has been taken into account. Once the value of the dimensionless radius of the fluorinated oil jet, r_∞ , is determined as a function of the control parameters through equation 3.6, we need to know the wavelength ℓ_0 of the perturbation leading to the formation of a fluorinated oil drop of diameter D_i . The wavelength ℓ_0 is calculated as:

$$\ell_0 = \frac{2\pi L}{k_{max}} r_\infty \quad (3.7)$$

with k_{max} the wavenumber that maximizes the temporal growth rates of the capillary perturbation, namely, $Real(-i\omega)$, with $\omega(k)$ given by the dispersion relation:

$$\begin{aligned} D(\omega, k) &= -i\omega \left(2 + \frac{k^2}{4\lambda_i} \right) + ik \left[2u_{x\infty} + f_\infty r_{j\infty}^2 \left(4 - \frac{2}{\lambda_i} \right) \right] - \frac{k^2}{8\lambda_i Ca} + \\ &+ ik^3 \left(\frac{u_{x\infty}}{4\lambda_i} + \frac{f_\infty r_{j\infty}^2}{4\lambda_i} \right) + \frac{k^4}{8\lambda_i Ca} = 0, \end{aligned} \quad (3.8)$$

deduced in [184]. In equation 3.8 k is a real number and denotes the wave number-made dimensionless using the characteristic length R_∞ , and ω is the complex frequency-made dimensionless using U and R_∞ as characteristic scales for the velocity and length respectively, $u_{x\infty} = 2$, $f_\infty = -8$ and r_∞ is the solution of the continuity equation 3.6.

Therefore, using equation 3.8, k_{max} is determined from the condition

$$\begin{aligned} Max [Real(-i\omega)] &= Max \left(\frac{1}{8\lambda_i C a_o} \frac{k^2 - k^4}{2 + k^2/(4\lambda_i)} \right) \\ &= Max \left(\frac{k^2 - k^4}{8\lambda_i + k^2} \right) \\ &\rightarrow k_{max} \simeq (8\lambda_i)^{1/4}, \text{ for } \lambda_i \ll 1. \end{aligned} \quad (3.9)$$

The shell production frequency is thus given by

$$f = \frac{2U}{\ell_0} = \frac{2U k_{max}}{2\pi L r_\infty} = K_1 \frac{U}{L r_\infty}, \quad (3.10)$$

with K_1 a constant since, in view of equation 3.9, λ_i and, therefore, k_{max} , remain constants in this experimental study. To test this relationship in our system, we plot the shell production frequency f obtained in our experiments as a function of U/Lr_∞ , see Fig. 3.19. U has been measured before, q_i and r_∞ are calculated from equation 3.6, and f is measured as the number of shells produced at a given time interval: $n_{shell}/N\Delta t$, where, as already stated, N is the number of frames in the considered time interval and $1/(\Delta t)$ is the camera frame rate. We obtained a linear relationship with a proportionality constant equals to $K_1 = 0.089 \pm 0.003$, which is close to what expected from equation 3.10, that is, $K_1 = 0.09$. These results validate our approach, albeit some experimental points deviate from the expected trend.

3.4.3 Inner (D_i) and outer (D_o) diameters of the nematic shells

To predict the inner (D_i) and outer (D_o) diameters of the nematic shells, we make use of the continuity equation, which demands that,

$$\frac{\pi D_i^3}{6} f = Q_i \quad \text{and} \quad \frac{\pi D_o^3}{6} f = Q_i + Q_m, \quad (3.11)$$

with f given by equation 3.10. Therefore, D_i and D_o can be respectively expressed as a function of the control parameters as

$$\frac{\pi D_i^3}{6} f = Q_i \Rightarrow K_1 \frac{\pi D_i^3}{6} \frac{U}{L r_\infty} = Q_i \Rightarrow \frac{D_i}{L} = \left(\frac{6 r_\infty}{\pi K_1} \right)^{1/3} q_i^{1/3}, \quad (3.12)$$

$$\frac{\pi D_o^3}{6} f = Q_i + Q_m \Rightarrow K_1 \frac{\pi D_o^3}{6} \frac{U}{L r_\infty} = Q_i + Q_m \Rightarrow \frac{D_o}{L} = \left(\frac{6 r_\infty}{\pi K_1} \right)^{1/3} q^{1/3}, \quad (3.13)$$

where $q_i = Q_i/(U L^2)$ and $q = (Q_i + Q_m)/(U L^2)$.

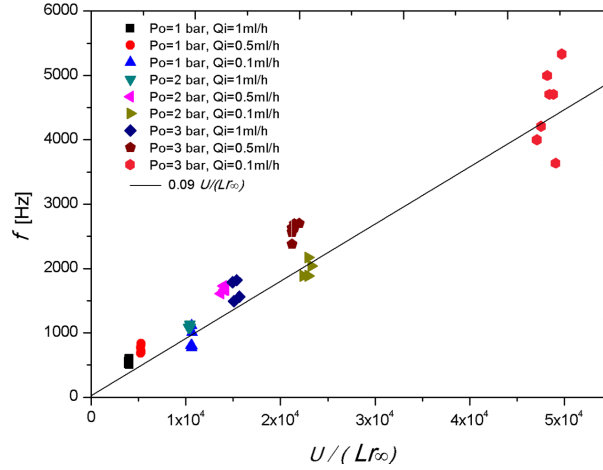


Figure 3.19: The experimentally measured frequencies depend linearly on $U/(Lr_\infty)$, as predicted by equation (3.10), with $K_1 = 0.096$, which is quite close to the predicted value $K_1 = 0.09$.

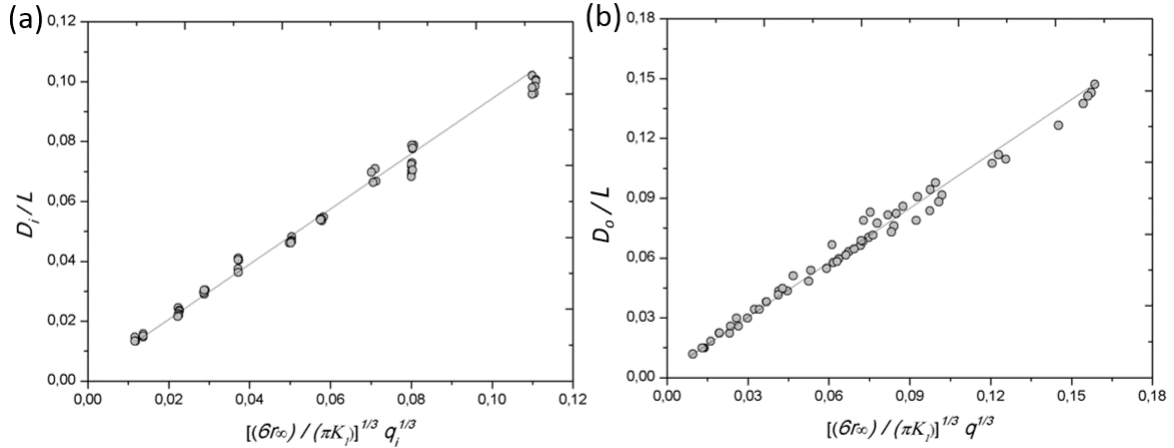


Figure 3.20: (a) Experimentally measured inner diameters D_i/L as a function of $[(6r_\infty)/(\pi K_1)]^{1/3} q_i^{1/3}$. (b) Experimentally measured outer diameters D_o/L as a function of $[(6r_\infty)/(\pi K_1)]^{1/3} q^{1/3}$.

The experimentally measured inner and outer drop diameters, D_i and D_o , are compared with the predictions given by equations 3.12 and 3.13 in Fig. 3.20, respectively. We find an excellent agreement between experiments and theory. We conclude that this new technique enables to produce liquid crystal shells of controllable thickness with $D_o \geq 10 \mu\text{m}$ when the inner and middle liquids are injected into the pressurized chamber using syringe pumps. Furthermore, equations 3.12 and 3.13 can be used to predict the shell diameter.

To further decrease the diameters of the drops produced, the flow rates of both the

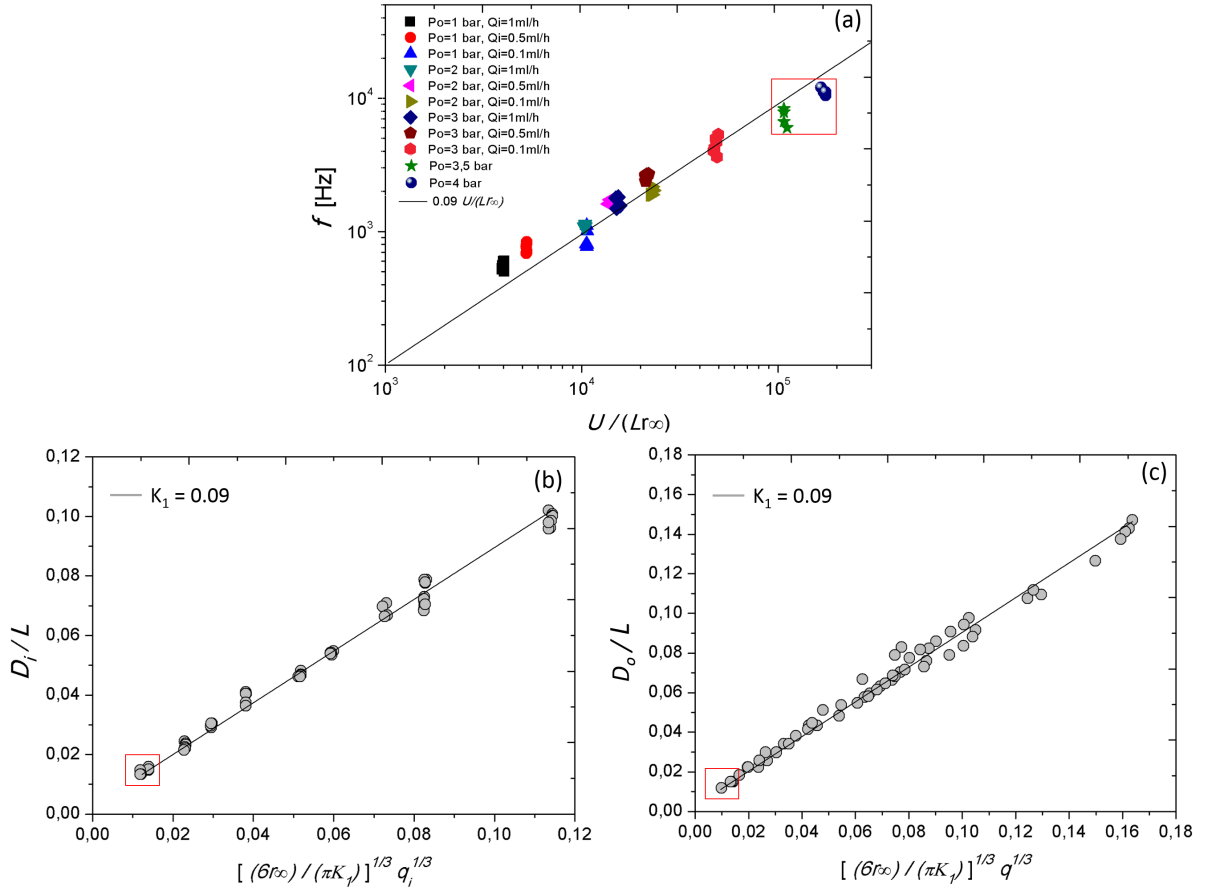


Figure 3.21: (a) The experimentally measured frequencies depend linearly on $U/(Lr_\infty)$, as predicted by equation (3.10). (b)-(c) The experimentally measured inner and outer drop diameters D_i and D_o respectively, are compared with the predictions given by equations 3.12 and 3.13, finding an excellent agreement between observations and theory. The data points highlighted in a red box in (a), (b) and (c) represent that liquid crystal shells that were generated when the injection of the three fluids is controlled by pressure.

inner and middle liquids need to be extremely small (below 0.01 ml/h). Pressure-control is better for stabilizing the meniscus of the coaxial jet, and then, reducing the size of the nematic shells. For this reason, we performed a set of experiments in which both 5CB and the fluorinated oil were injected by controlling the pressures differences $P_i - P_a$ and $P_m - P_a$. In these cases, appreciably larger experimental frequencies (f) and smaller shell diameters (D_i and D_o), highlighted in the red square in Fig. 3.21 (a)-(c), are obtained, which also follow the scaling laws described in equations 3.10, 3.12 and 3.13. The use of a narrow injection needle (the one employed in this study has an outer orifice of 1.1 mm) is expected to yield even smaller nematic shells.

3.5 Conclusion

In this chapter, we presented a production method based on the capillary breakup of highly stretched long coaxial capillary jets, which is capable of producing nematic shells with diameters of the order of 10 microns, or even smaller, at frequencies exceeding 1 KHz. The so called confined selective withdrawal technique, possesses advantages with respect to other microfluidic techniques. It eliminates the difficulties associated with tedious fabrication process and dependence on any geometrical scale, making possible producing shells in a wide range of sizes and thicknesses, with controllability and high production frequencies. We have checked that the theoretical predictions for the outer diameters of the shells, their thicknesses and the generation frequencies are in good agreement with the experimental observations.

Chapter 4

Controlling the valency of liquid crystal shells through shell geometry

Introduction

As discussed in the Introduction of this thesis, nematic shells offer great possibilities to produce multivalent colloids. In these systems, the spherical symmetry of the particle is broken due to the presence of topological defects, which result from frustrations in the nematic order induced by the spherical confinement. These topological defects are part of the ground state of the system, and thus, appear spontaneously, offering a robust way for imprinting well defined interaction sites on a sphere. A key milestone in the realization of this idea is to develop tools that allow us to produce particles with targeted coordination number and valence angles by controlling the number and position of the defects on the shell surface. Shell thickness inhomogeneity [71, 203] and elastic anisotropy [67, 203] have been successfully employed to tune the position of defects. In this chapter, we will explore the possibility of inducing changes, not in the bonding directionality (position of defects), but in the valence (number of defects) of the shell by provoking drastic variations in the shell geometry. We will investigate the energy landscape in the system and evaluate the role of metastability.

4.1 Defect configurations in nematic shells

4.1.1 Simulated nematic shells

Numerical studies have shown that the energy landscape for the different defect structures observed in the shells depends very much on the shell geometry [129–131]. As mentioned in Chapter 1, section 1.6.2, our experimental shells have an asymmetric geometry. Due to buoyancy effects, the inner droplet floats or sinks inside the outer one, leading to shells that are heterogeneous in thickness. Fig. 4.1(a) shows a side view of a experimental shell,

obtained by rotating the microscope 90° with respect to gravity. For this asymmetric geometry, numerical simulations predict two possible configurations, whose relative energies depend on the average thickness of the shell $h \equiv R - a$, where R is the outer and a the inner radius of the shell, respectively. For thin shells, a defect structure with four $s = +1/2$ disclination lines (referred to as tetravalent) is observed, see Fig. 4.1(b). When the shell is thicker, a new defect configuration (referred to as trivalent) appears, which is characterized by two $s = +1/2$ disclinations, or line defects, and a pair of $s = +1$ boojums, or surface defects, see Fig. 4.1(c). In the tetravalent shell, the four disclination lines are close together at the thin part of the shell. As reported in previous studies [66, 71, 204], their equilibrium positions depend on the shell thickness gradient. By bringing the inner droplet to the center, the disclination lines move apart to reach the sought-after tetrahedral symmetry. In the trivalent structure shown in Fig. 4.1(c), the pair of disclinations is located at the thinner part of the shell, while the boojums are located at the thicker part. The antipodal symmetry of trivalent simulated shell is, in contrast, independent of the thickness gradient. Fig. 4.1(d) shows the free energy densities of the tetravalent and trivalent configurations as a function of the dimensionless thickness h/R . The free energy of the tetravalent structure (red curve) increases with h/R , while the free energy of the trivalent structure (black curve) decreases. Both curves cross over at $h^* = 0.55R$. These results suggest that it might be possible to induce transitions between the trivalent and tetravalent configurations by playing with h/R .

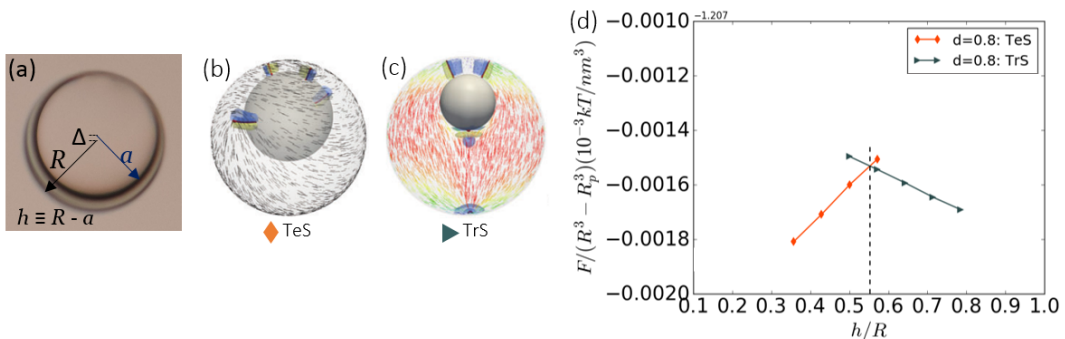


Figure 4.1: (a) Experimental nematic shell with heterogeneous thickness. (b) Simulated tetravalent defect structure with four $s = +1/2$ disclination lines. (c) Simulated trivalent configuration with one pair of $s = +1$ boojums at the thicker part of the shell, and two $s = +1/2$ disclination lines at the thinner part of the shell. (d) Free-energy density graph as a function of the shell thickness (h/R) for the tetravalent and trivalent structures.

4.1.2 Experimental nematic shells

To investigate the possibility of inducing transitions between different valence states, we used shells with a characteristic diameter of $100 \mu\text{m}$, produced in a glass capillary device,

as shown in Chapter 2. The liquid crystal employed was 5CB, whose chemical formula and physical properties have been introduced in Chapter 1, Section 1.6. At room temperature, 5CB displays a nematic phase. We added PVA to the inner and outer aqueous phases to stabilize the emulsions and impose planar molecular anchoring at the boundaries, see Chapter 1, Section 1.6 for more information. In shells with $h/R = 0.16$, we observed the tetravalent structure predicted by the simulations, in addition to other coexisting structures already reported. These structures are shown in Fig. 4.2, which are cross-polarized images of the three different types of shells. The tetravalent structure is shown in Fig. 4.2(a), which is a top view of the shell. Here, each of the four disclinations carries a topological surface charge $s = +1/2$ and can be identified by the presence of two black brushes when observed between crossed polarizers, as explained in Chapter 1, Section 1.6.2. Besides the tetravalent configuration, there is another configuration (referred to as bivalent) characterized by two pairs of $s = +1$ boojums, which appear located at the thin part of the shell. Fig. 4.2(c) shows the two boojums located on the outer surface of the shell, each of them, displaying four black brushes. The trivalent defect configuration containing two $s = +1/2$ disclination lines and one pair of $s = +1$ boojums is also observed, see Fig. 4.2(b). However, the defects are not arranged in the bipolar structure shown in Fig. 4.1(c), but they appear again confined at the thin part of the shell.

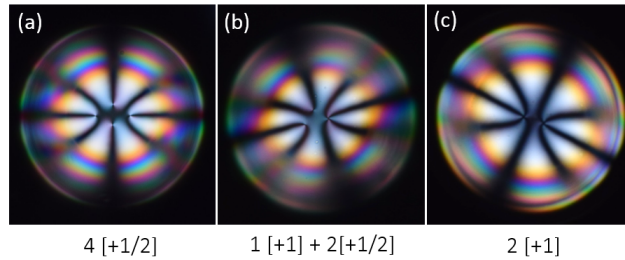


Figure 4.2: Defect configurations in experimental liquid crystal shells. The images are cross-polarized micrographies showing a top view of three shells ($h/R = 0.16$) displaying (a) tetravalent, (b) trivalent, and (c) bivalent configurations.

The equilibrium distance between the defects results from the balance between (i) a repulsive defect interaction of elastic nature and (ii) an attractive force due to the shell thickness gradient [66, 71, 204]. For this reason, in homogeneous shells, where the second term is zero, the defects maximize their separation distances, while in heterogeneous shells, where the second term is dominant, they appear confined at the thin part of the shell. As already mentioned, this effect is captured in simulated shells only for the case of the tetravalent structure. All these results, in particular the fact that we observe the coexistence of different defect structures for a given value of h/R , suggest the existence of metastability. In the next section, we explore the range of h/R in which the different structures can exist and investigate the possibility of inducing transitions between different configurations by changing h/R .

4.2 Osmotic effects

To induce a continuous variation of h/R in the shell, we use osmotic effects. Through the addition of salt, in particular, CaCl_2 , we induce a difference in osmotic pressure between the inner and outer aqueous phases, see the schematics in Fig. 4.3. As 5CB has certain permeability to water, it allows for water transport between the inner and outer phases. In particular, the addition of salt to the outer phase, makes the inner droplet de-swell. In this way, the inner radius a progressively decreases, and therefore, h/R increases. By controlling this difference in osmotic pressure, we can control the kinetics of the process and ultimately the range of variation of h/R . Fig. 4.4(a)-(e) shows a continuous transformation of the core-shell structure of a regular water/oil/water double emulsions towards a simple droplet geometry, by the progressive de-swelling of the inner droplet. Upon salt addition to the continuous phase, the inner water droplet de-swells with time (black circles in Fig. 4.4(f)), making the shell progressively thicker (blue circles in Fig. 4.4(f)), until the inner droplet completely disappears.

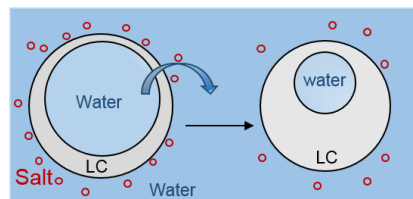


Figure 4.3: Schematic illustration of the osmotic mechanism used to continuously vary the thickness of nematic shells.

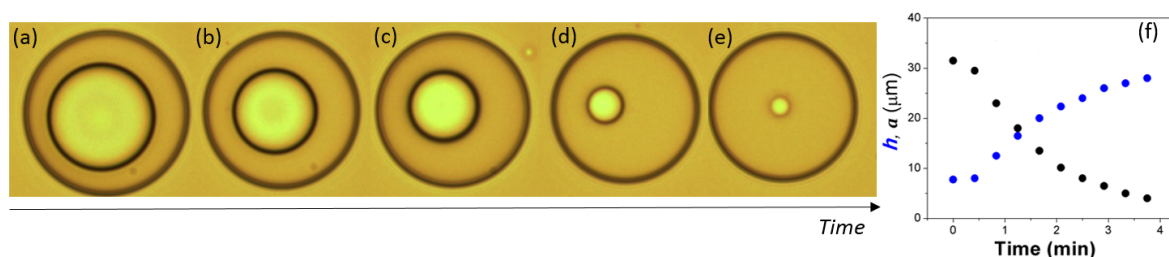


Figure 4.4: (a)-(e) De-swelling process in a water/oil/water double emulsion after the addition of a salt to the outer phase. (f) During the process, the radius of the inner droplet a (black symbols) decreases, while the shell thickness h (blue symbols) increases.

4.3 Topological transitions between different defect configurations

When nematic shells undergo the geometrical transformation, as shown in Fig. 4.4, the energy associated to the initial defect configuration typically increases, triggering transitions towards states that are lower in energy. We observe different transitions depending on the initial defect configuration of the shell.

4.3.1 De-confinement transitions in bivalent nematic shells

Increasing the shell thickness of a bivalent shell induces a re-location of the two pairs of boojums, as shown in Fig. 4.5. When the shell is relatively thin, the two pairs of boojums are not at antipodal positions, but confined to the thinnest part of the shell, as described before and shown in Fig. 4.2(c). As the inner droplet de-swells, the shell becomes thicker, and the attractive term associated to the thickness gradient becomes more important, making the defects get closer [204], see Fig. 4.5(a). When the inner radius reaches a critical value, we observe an abrupt transition, where one pair of boojums remains at the thinnest part of the shell, while the other rapidly migrates towards the opposite pole, see Fig. 4.5(b). This process, in which the boojum pairs maximize their separation [205], will be referred to as the de-confinement transition. In the final state, the shell has a bipolar configuration, where the two pairs of boojums are diametrically aligned, as shown in Fig. 4.5(d). This structure remain unaltered as the inner droplet keeps shrinking, eventually yielding a bipolar nematic bulk droplet.

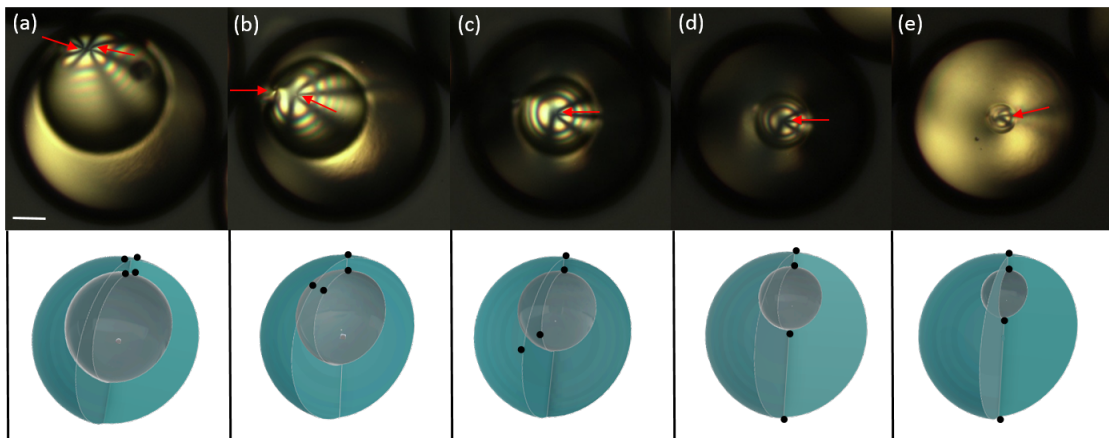


Figure 4.5: (a)-(e) Cross-polarized images of a shell (top view) with two pairs of $s = +1$ boojumss at different stages of the de-swelling process. The red arrows indicate the location of the defects. The schematics below indicate the approximate position of the two pairs of boojums (black dots) for each cross-polarized image. Scale bar: $25 \mu\text{m}$.

4.3.2 De-confinement transitions in trivalent nematic shells

This de-confinement transition, which is almost systematic in bivalent shells, can also occur in trivalent shells. In the latter case, two $s = +1/2$ disclination lines and a pair of $s = +1$ boojums are initially placed at the thinnest part of the shell, see Fig. 4.6(a). As the inner drop decreases, the defects get closer in order to reduce bulk distortions, as explained before. At a certain critical value of the inner radius, the pair of boojums migrates toward the bottom of the shell, leaving the two disclinations at the top of the shell, see Fig. 4.6(c). The resulting final configuration corresponds to the simulated structure shown in Fig.1 (e). The rest of the process involves the shrinkage of the inner droplet, see Fig. 4.6(d) and (e), and the final recombination of the two $s = +1/2$ disclinations with the $s = +1$ boojum associated to the inner droplet, to give the bipolar boojum structure of the final nematic droplet.

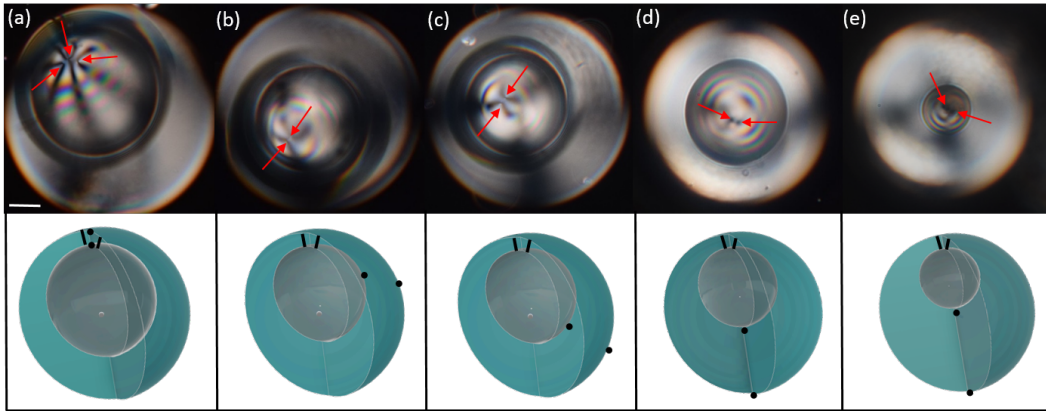


Figure 4.6: (a)-(e) Cross-polarized images of a shell (top view) with one pair of $s = +1$ boojums and two $s = +1/2$ disclinations at different stages of the de-swelling process. The red arrows indicate the location of the defects. The schematics below show the approximate position of $s = +1/2$ defects (black lines spanning the shell) and $s = +1$ boojums (black dots) on the outer sphere and its counterpart on the inner sphere. Scale bar: $25 \mu\text{m}$.

4.3.3 Expulsion of inner droplets from nematic shells

Interestingly, the de-swelling process is completely different in tetravalent shells, as shown in the sequence of bright-field images of Fig. 4.7(a)-(f). Similarly to the experiments described above, the inner droplet de-swells and the shell becomes progressively thicker when increasing the osmotic pressure of the outer phase, see Fig. 4.7(a)-(c). However, when the inner radius decreases to a critical point, see Fig. 4.7(d), the inner droplet suddenly pops out of the shell, which abruptly transitions to a bulk nematic droplet, see Fig. 4.7(f). This geometrical transformation produces a series of topological changes in the nematic field, as shown in Fig. 4.8. Initially, the four $s = +1/2$ disclinations are

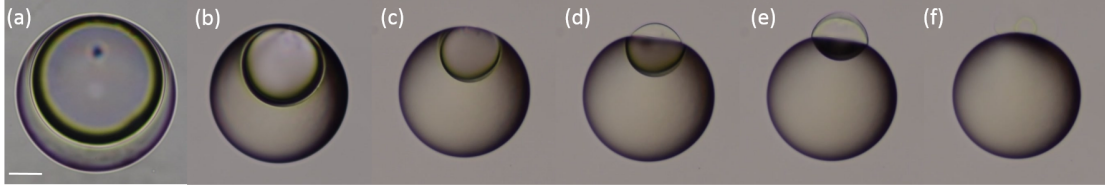


Figure 4.7: (a)-(f) Bright-field images showing the de-swelling and expulsion of the inner droplet in a tetraivalent nematic shell. Images (a)-(c) show how the inner droplet de-swells with time until it reaches a critical point, then the inner droplet goes across the interface, as shown in (d) and (e), finally the nematic shell becomes a nematic simple droplet, as shown in (f). Scale bar is $25 \mu\text{m}$.

located at the top of the shell, see Fig. 4.8(a). These defects remain tightly clustered as the shell becomes thicker, see Fig. 4.8(b). When the inner droplet starts travelling across the outer one, the initial $s = +1/2$ disclinations disappear and two half $s = +1$ boojums nucleate at the contact line between the inner and outer droplets, see Fig. 4.8(c). These two boojums eventually unpin from the contact line and move away from each other, due to the repulsion existing between like-charged defects [65] to eventually relocate at the two poles of the final nematic droplet, see Fig. 4.8(d)-(f).

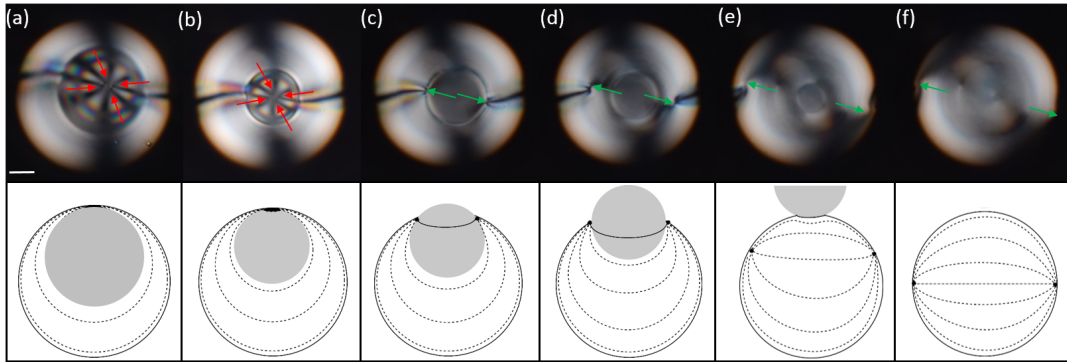


Figure 4.8: Topological transformations undergo by a shell with four $s = +1/2$ disclinations upon the de-swelling of the inner droplet. The upper part of the figure shows cross-polarized images of the shell (top view), while the lower part of the figure shows the corresponding schematics of the director field (side view). (a) Initially the shell has four $+1/2$ disclinations indicated by red arrows. (b) As the shell becomes thicker, the $1/2$ disclinations become closer. (c) When the inner droplet is expelled out of the outer one, the $+1/2$ disclinations transform into half-boojums of charge $+1$, indicated by green arrows. (d) and (e) While the inner droplet goes across the interface, the boojums move away from each other. (f) In the final state, the boojums are placed at opposite sides of the remaining nematic bulk droplet. Scale bar is $25 \mu\text{m}$.

4.4 Origin of expulsion of inner droplets from nematic shells

4.4.1 Energy barrier for the expulsion

The expulsion of the inner droplet does not occur in regular W/O/W double emulsions, so it seems to be somehow triggered by the elasticity of the nematic liquid crystal. To test this hypothesis, we repeat the de-swelling experiment at a temperature above the isotropic-nematic transition temperature where the elastic forces are zero. As expected, the inner droplet is never expelled, which indicates that nematic elasticity is a driving force for the expulsion of inner droplet.

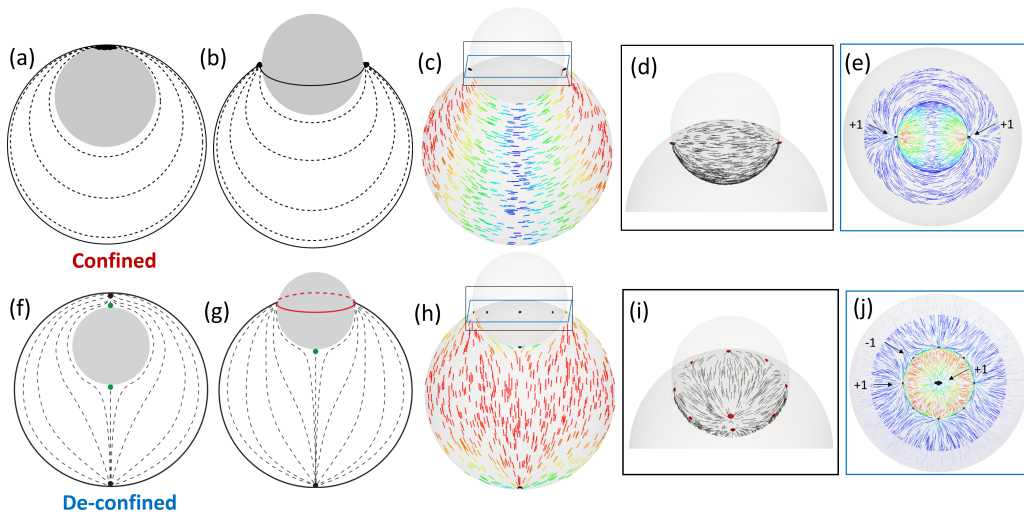


Figure 4.9: (a) Schematic director field of shell in a confined state. (b) Schematic transient structure with two half-boojums at opposite sides of the contact line. (c) Simulated transient structure with two half-boojums at opposite sides of the contact line. (d) Director field on the inner sphere and (e) a top view of the shell, corresponding to the transient state (c). (f) Schematic director field of shell in a de-confined state. (g) Schematic transient structure with a singular ring. (h) Simulated transient structure with a ring of point defects. (i) Director field on the inner sphere and (j) a top view of the shell, corresponding to the transient state (h).

It seems that the symmetry of the shell also plays a key role. Note that during the de-swelling experiment, if the defects, irrespectively of the number, stay confined all along the process, the inner droplet will be expelled from the shell. However, if the defects relocate at opposite poles along the process, the expulsion never occurs. Accordingly, we consider and compare two distinct states: (i) a confined state in which the defects are placed at

the thinnest part of the shell, yielding a director field with the symmetry shown in Fig. 4.9(a) and (ii) a de-confined state where the defects are arranged diametrically, yielding a director field with the symmetry shown in Fig. 4.9(f).

To inquire about the effect of the director field symmetry in the expulsion process, we performed numerical simulations in collaboration with de Pablo's team at the University of Chicago. We considered a shell either in a confined or a de-confined state and calculated the evolution of the director field, and the free energy associated, as the inner drop was shifted out of the shell. The numerical method used for these simulations is shown in Chapter 1, Section 1.6.3. In the case of a shell in a confined state, we observe a transient structure with two half-boojums at opposite sides of the contact line, as expected. This structure is shown in Fig. 4.9(c), which shows the director field on the outer surface, Fig. 4.9(d) shows the director field on the inner sphere, and Fig. 4.9(e) shows a top view of the shell, where we can see the director field around the defect. In the case of a shell in a de-confined state, we observe the structure shown in Fig. 4.9(h), where the expected singular ring destabilizes into a ring of point defects. Since the total topological charge has to be conserved, we observe an alternation of positive and negative defects, as indicated in Fig. 4.9(j).

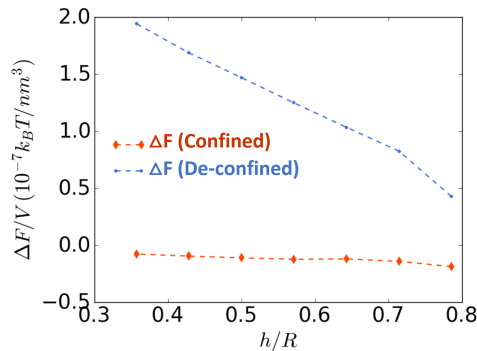


Figure 4.10: Energy barriers associated to the droplet expulsion for de-confined path and confined path.

Fig. 4.10 shows the energy difference between the transient state (Fig. 4.9(c)) and the confined state (Fig. 4.9(a)), denoted as $\Delta F(\text{confined})$ and the energy difference between the transient state (Fig. 4.9(h)) and the de-confined state (Fig. 4.9(f)), denoted as $\Delta F(\text{de-confined})$, as a function of h/R . We observe that there is an important energy barrier that prevent shells in the de-confined state from expelling the inner droplet (blue curve), while this barrier is almost zero when the shell is the confined state (red curve). In some sense, in the de-confined state the shells are topologically protected against expulsion, which explain why we never observe such phenomenon experimentally. In the confined state, we observe expulsion at values of h/R between 0.5 and 0.6, depending on the salt concentration. These values are reasonable close to the critical point ($h/R = 0.55$)

where the simulations predict the transition between the tetravalent and trivalent configurations, see Fig. 4.1(d) [129, 131, 206].

4.4.2 Effect of water flux

In our experiments, the inner drop is expelled at a critical inner radius a^* . The results of the de-swelling experiments using different concentrations of salt CaCl_2 show that the radius of the inner drop continuously decreases with time up to a point at which the expulsion occurs, see Fig. 4.11(a). The critical radius depends on the osmotic pressure (salt concentration) of the outer phase: the higher the osmotic pressure, the smaller the radius of the droplet at the expulsion time, as shown in Fig. 4.11(b). This might be related to the dynamics of the de-swelling process. Indeed, the flux of water through the shell might play a relevant role in the destabilization of the nematic film separating the inner droplet from the continuous phase.

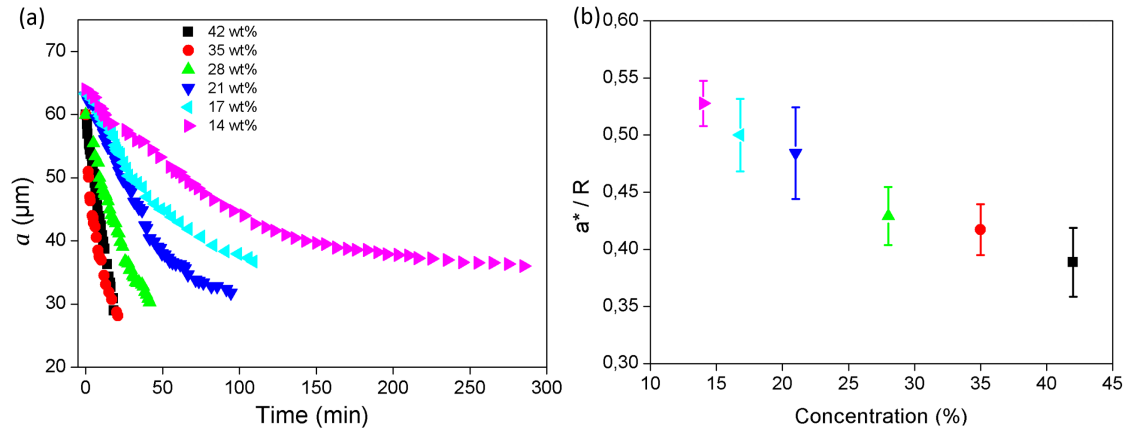


Figure 4.11: (a) Variation of inner radius a as a function of time for different salt concentrations. (b) Critical inner radius a^* at the expulsion time as a function of salt concentration. Scale bar: $25 \mu\text{m}$.

To investigate a possible correlation between the critical expulsion time and flow dynamical effects, we calculate the water flux through the shell along the de-swelling process. In the experiment, after salt addition, the inner droplet flattens at its thinner part to facilitate the water transport, as shown in Fig. 4.12(a). We assume that the flux of water mainly occurs through this thin nematic film. We then simulate a 100 nm film of 5CB, which is in contact with the inner and the outer phases, and compute the flux of water through this thin film under different salt concentrations, as schematically represented in Fig. 4.12(b).

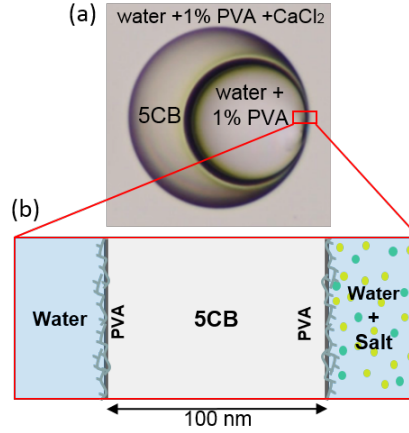


Figure 4.12: (a) Bright-field image of a nematic shell upon de-swelling the inner droplet. (b) Schematic illustration of thin part of the shell, a film of 5CB with a thickness of 100 nm.

Computation of the time-dependent flux of water through the LC film

One can describe the time-dependent flux of water through a thin LC film, upon addition of salts to the outer aqueous phase, using the following equation:

$$J = \int \frac{\partial \rho}{\partial t} dz + D e^{-\frac{W}{k_B T}} \frac{\Delta C}{L} \quad (4.1)$$

here, ρ is the water density, t is time, D is the water diffusion constant, W is the potential of the mean force (PMF) for the transfer of a water molecule from the bulk water phase to the bulk LC phase [207], k_B is Boltzmann's constant, T is temperature, L is the thickness of the film, and ΔC is the effective concentration difference. The evolution of the water density inside the LC film can be simulated using the Smoluchowski (drift-diffusion) equation [208]:

$$\frac{\partial \rho}{\partial t} = \nabla \cdot (D \nabla \rho) - \nabla \cdot (\zeta^{-1} \vec{F} \rho) \quad (4.2)$$

here, $\zeta^{-1} = D/k_B T$ is the mobility and $\vec{F} = -\nabla W$ is the mean force. Assuming a location-independent diffusion constant D for water, the Smoluchowski equation in one dimension reduces to the following expression:

$$\frac{\partial \rho}{\partial t} = D \frac{\partial^2 \rho}{\partial z^2} + \frac{D}{k_B T} \frac{dW}{dz} \frac{\partial \rho}{\partial z} + \frac{D}{k_B T} \frac{d^2 W}{dz^2} \rho \quad (4.3)$$

We approximate the solution of the Smoluchowski equation numerically using a finite difference approach following our previously described procedure [207]. First, we compute the equilibrium profile of the water density inside the LC film in the absence of salts. Because the LC film is in contact with pure water on both sides, the PMF profiles on both sides

of the film are identical. Accordingly, we fit a \tanh function $W = \frac{A}{2}\tanh(B(z - z_0)) + \frac{A}{2}$ to the PMF curve (see reference [207] for more details), and employ that profile in our calculations. In this function, A is the free energy cost for relocation of a single water molecule from the water phase to the LC phase, $B = 0.5$, and $z_0 = 5$. Next, we compute the evolution of the water density upon addition of salts to the outer phase. Here, the equilibrium profile of the water density (from the first step) serves as our initial configuration. Upon addition of salts to the outer phase, the PMF profiles on the water side and the electrolyte side will differ because the free energy cost for transfer of a water molecule from the aqueous phase into the LC phase increases after addition of salts. This difference in the free energy cost can be estimated using $k_B T \ln a_w$, where a_w is the water activity of the electrolyte solution [209]. The PMF profile on the electrolyte side now follows the form $W = \frac{A}{2}\tanh(B(z - z_0)) + (A - \frac{C}{2})$. Here, C is the free energy cost for the transfer of a water molecule from the bulk electrolyte solution to the bulk LC phase. Our calculations rely on the tabulated water activity of calcium chloride CaCl_2 solutions in reference [209].

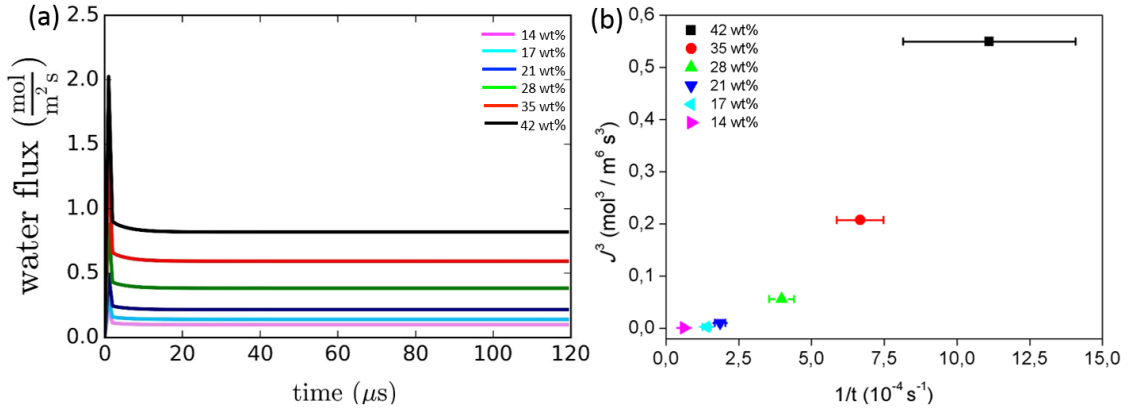


Figure 4.13: (a) Time-dependent flux of water through the thin film after addition of different concentrations of CaCl_2 . (b) The correlation between the expulsion time of the inner drop and water flux at the steady state under different concentrations of CaCl_2 .

The profiles of the water flux through the thin film, see Fig. 4.13(a), show that addition of salt to the outer phase leads to a burst of water flux within the first few microseconds of salt addition [207], the system then reaches a steady state where the flux of water remains constant. The magnitude of the water flux at the steady state depends on the concentration of the salt. We hypothesize that the expulsion time could be related to the kinetic energy applied to the film due to the water transport. The correlation between the expulsion time of the inner drop and the magnitude of the steady state flux can be described using $t \simeq \frac{2 \cdot \rho^2 \cdot E_b}{J^3}$, where t is expulsion time, ρ is the water density, E_b is the energy required to break the film, and J is the water flux. Fig. 4.13(b) shows how J^3 varies as a function of $1/t$. Although the dependence is not sharply linear, this result demonstrates a clear effect of the water flux in the film destabilization. We note that the expulsion of the

inner drop under an osmotic pressure is a relatively complex process with some stochastic nature. Several factors including (i) the diffusion of salts from the continuous phase to the outer surface, (ii) the variable thickness of the liquid crystal film due to water transport, (iii) three-dimensional diffusion of water from the inner drop to the outer phase, and (v) formation of water channels between the inner and outer phases may all play relevant roles. The specific details of such mechanisms will be the subject of a future investigation.

4.5 Conclusions

In this chapter, we have investigated the possibility of inducing topological transitions between different defect configurations by playing with the shell geometry. We conclude that transitions involving a change in the particle valence, which means a conversion of defects of one type into another one, are energetically forbidden. Interestingly, increasing the overall thickness of the shell, by de-swelling the inner droplet, can lead to two different topological paths depending on the initial state of the system, involving: (i) the re-location of topological defects and (ii) dramatic transition in which the inner droplet is expelled from the shell when a critical average thickness is reached. We find that this critical average thickness depends on the osmotic pressure of the outer phase. We have finally investigated, by means of numerical simulations, the role of elasticity and osmotically driven water fluxes through the shell on the expulsion of the inner droplet.

Chapter 5

Controlling the valency of liquid crystal shells through elastic anisotropy

Introduction

In Chapter 4, we have studied the influence of the shell geometry on its defect structure. Here, we will study the effect of having anisotropy in the elastic constants of the liquid crystal. Previous simulations have shown that elastic anisotropy can have an important effect on the distribution of defects within the shell. For instance, in a 2D nematic shell, if $K_1 = K_3$, theory predicts a tetrahedral configuration, where the four $+1/2$ disclinations sit at the vertices of a tetrahedron [61]. Interestingly, if $K_3 \gg K_1$, the four disclinations re-locate along a great circle of the shell, in a square configuration [63, 64]. In the limit $K_3/K_1 \rightarrow \infty$, simulations show that the system changes the square configuration into a rectangular one [64]. Studying the effect of elastic anisotropy experimentally is not trivial, since in most liquid crystals $K_1 = K_2 = K_3$. One possible strategy is to bring the system close to a phase transition, where certain elastic constants might diverge. For instance, by bringing a nematic shell close to the nematic-smectic phase transition, where K_3 diverges, it has been possible to experimentally study how K_1/K_3 impacts the defect structure of the shell [67]. The effect of varying K_2 has not been explored yet.

A new type of liquid crystals, called lyotropic chromonic liquid crystals (LCLCs), seems to offer very interesting possibilities for this kind of studies. Indeed, recent studies have shown that LCLCs have a nematic phase where K_2 is extremely low compared to K_1 and K_3 [210, 211]. This leads to spontaneous twist as soon as the system is constrained, for instance, due to confinement. For this reason, confining a LCLC to a curved space gives rise to complex three-dimensional organizations that have just started to be explored [212–215]. In this chapter, we will study the defect structures emerging when a LCLC is confined to droplets and spherical shells. For this study we have used a LCLC called Sunset Yellow

FCF (SSY), whose properties have been described in Chapter 1, section 1.6. We characterize our system in terms of the concentrations of SSY at which each phase transition takes place, and then, study these phase transitions under confinement. We will investigate three geometries: (i) spherical droplets, (ii) sessile droplets and (iii) spherical shells.

5.1 Lyotropic chromonic liquid crystals

Lyotropic chromonic liquid crystals are aqueous phases of supramolecular assemblies of small molecules. When dissolved in water, they undergo self-assembly via electrostatic forces between ionized polar groups, hydrophobic interaction and $\pi - \pi$ interaction between aromatic cores. This self-assembly leads to the formation of elongated aggregates which act as building blocks of the mesophase [141]. The organization of the aggregates, in turn, give rise to the formation of liquid crystal phases: a nematic phase (N), in which the aggregates are aligned along their long axis, a columnar phase (C), where the aggregates form a two-dimensional hexagonal crystalline structure, and a three-dimensional crystalline structure at even larger concentrations of the aggregates [137,216]. The formation of a given phase depends not only on concentration, but also on temperature [217], ionic additives [144], pH of the solution [144,218], or type of the side groups [141], making LCLCs very different from thermotropic liquid crystals, where the phase diagram is only controlled by temperature. Due to their solubility in aqueous medium and their optical properties, LCLCs are interesting systems for applications such as biosensing [219], micro-patterning [220], nano-fabrication [221], etc.

Table 5.1: Elastic constants of SSY (29 wt%) and 5CB at 25°C.

| LC | K_1 [pN] | K_2 [pN] | K_3 [pN] | Reference |
|-----|------------|------------|------------|-----------|
| SSY | 8.1 | 0.8 | 8.7 | [210] |
| 5CB | 6.6 | 3 | 10 | [92] |

As explained in Chapter 1, Section 1.1.3, the nematic phase is characterized by three main elastic constants: K_1 , K_2 , and K_3 associated to splay, twist and bend deformations respectively. While in conventional thermotropic nematics K_1 , K_2 , and K_3 have similar values, in LCLCs, K_2 is much lower than the other two elastic moduli. Table 5.1 shows the values of the elastic constants for SSY (29 wt%) as compared to conventional thermotropic nematics such as 5CB at 25°C.

SSY not only exhibits optical birefringence, as thermotropic nematics, but also linear dichroism, because of the presence of an azobenzene molecule in its chemical structure [217], as described in Chapter 1, Section 1.6. Linear dichroism is an optical property observed when the liquid crystal is placed on a microscope with polarizer, but without analyzer. Depending on the orientation of the molecules with respect to the polarizer, the amount

of light absorbed by the sample is more or less important. In particular, the absorption is greater in those directions where the director is perpendicular to the polarizer [220, 222]. Those regions where the director is aligned with the polarizer appear, then, brighter, as shown in Fig. 5.1(a) and (b). Thereby such absorption anisotropy can also be used to assign director orientation.

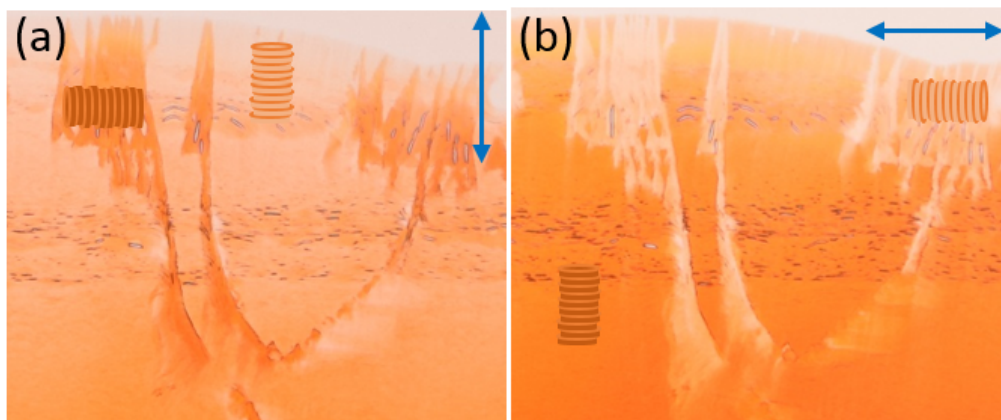


Figure 5.1: Optical textures of a SSY solution in the columnar phase observed with a polarizing microscope. Linear dichroism is shown: the color intensity depends on the orientation of the molecules relative to the direction of the axis of the polarizer. The schematic columns represent the orientation of the aggregates formed by the SSY molecules.

5.2 Spherical droplets

5.2.1 Phase diagram for the SSY-water system

To prepare SSY solution, we firstly purify and dehydrate SSY by following the procedures that have been described in Chapter 1, Section 1.6. Then we mix known amounts of purified SSY powder and Millipore water in a small centrifuge tube, and quickly seal the container. In order to dissolve SSY efficiently, a vortex mixer is employed. Then, we heat the mixture at 45°C for a few minutes in order to disperse the molecules and homogenize the sample.

We obtained the phase diagram for our system by analyzing the optical birefringence of the sample at different concentration of SSY, c_{SSY} (wt%). Fig. 5.2 shows the different phases that the system goes through as c_{SSY} increases: coexisting isotropic and nematic phases ($28\% \leq c_{SSY} < 30\%$, Fig. 5.2(a)), homogeneous nematic phase ($30\% \leq c_{SSY} <$

35%, Fig. 5.2(b)), coexisting nematic and columnar phases ($35\% \leq c_{SSY} < 40\%$, Fig. 5.2(c)), and columnar phase ($c_{SSY} \geq 40\%$, Fig. 5.2(d)). This phase diagram was obtained by leaving the glass cell open to allow slow water evaporation and condensation of the SSY solution. The nematic phase produces schlieren textures and the columnar phase shows characteristic developable domains [92]. Our data are in agreement with the previous phase diagrams reported [144]. The small discrepancy with the values provided in literature might be caused by the degree of SSY purification and dehydration, or by a different initial purity of SSY.

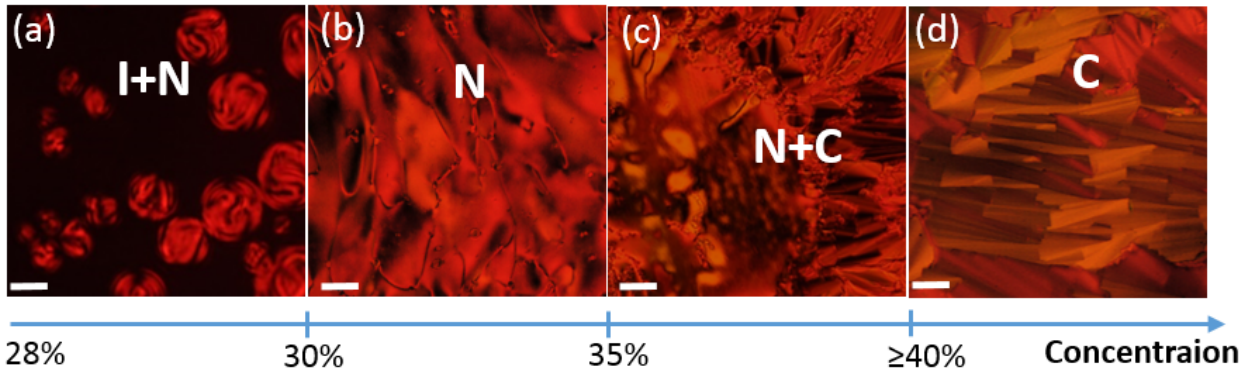


Figure 5.2: Phase diagram of our SSY water solution. The evolution of the optical texture of the SSY solution observed with polarized microscopy at room temperature (25°C). (a) Coexistence of isotropic and nematic (I + N) phases: nematic droplets surrounded by an isotropic phase. (b) Schlieren texture of a homogeneous nematic (N) phase. (c) Coexistence of nematic and columnar (N + C) phases. (e) Laminar texture in columnar (C) phase.

5.2.2 Stable emulsions of SSY-water solutions in oil

We produce stable emulsions of a SSY-water solution in hexadecane by adding sorbitan monooleate (Span 80) as surfactant. To make SSY droplets, we mix the aqueous nematic SSY solution (30.5 wt%) into hexadecane containing Span 80 (2.0 wt%) by pipetting and shaking. The volume fraction of SSY solution in hexadecane is $\sim 1\%$. The prepared samples are placed between a glass slide and a cover slip separated by spacers ($180\ \mu\text{m}$ thick), as shown in Fig. 5.3(a), to avoid fast water evaporation. Bright-field and cross-polarized images of nematic SSY droplets in hexadecane are shown in Fig. 5.3 (b) and (c). All the samples were observed immediately after preparation at room temperature (25°C). Water in the SSY solution undergoes a slow evaporation through the oil phase leading to an increase of the SSY concentration and an eventual phase transition from the nematic to the columnar phase.

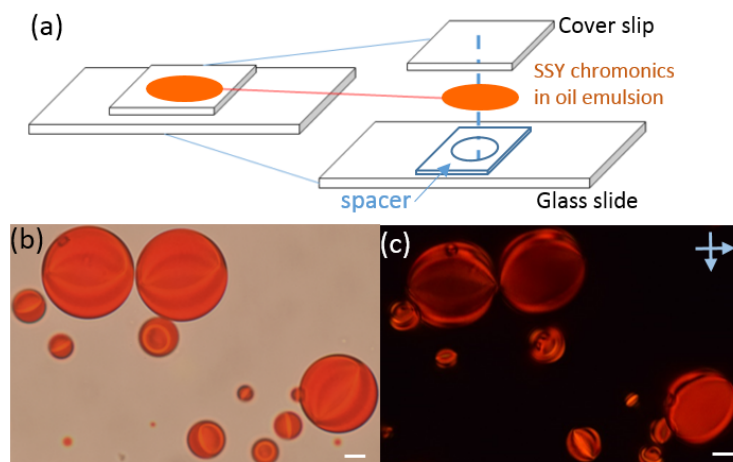


Figure 5.3: (a) Glass cell for sample observation. Bright-field (b) and cross-polarized (c) image of SSY droplets in hexadecane. Scale bar: 25 μm .

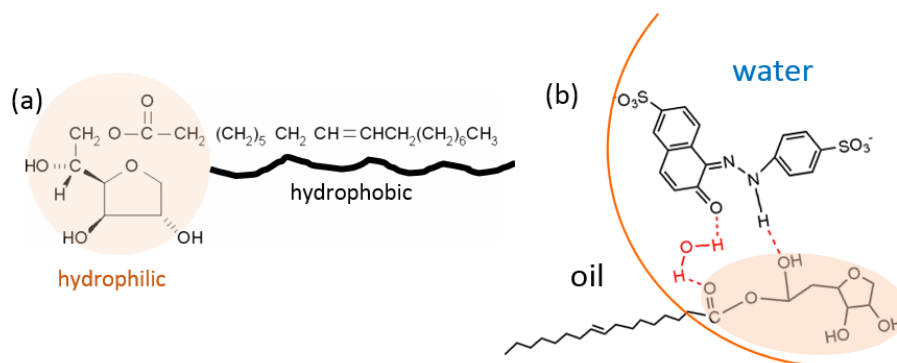


Figure 5.4: (a) Chemical structure of Sorbitan monooleate (Span 80). (b) Schematic of SSY droplets in an oil background phase, showing the orientation of a SSY and Span 80 molecule at the interface.

The effect of surfactants on how the SSY aggregates orientate themselves with respect to the interface (anchoring) is not entirely clear [223]. As it is not clear how the presence of surfactants impacts the molecular self-assembly of the LCLC. Span 80 is a nonionic surfactant, with a hydrophobic tail and hydrophilic head, as shown in Fig. 5.4(a). It has been suggested that hydrogen bonding contributes to the interaction of hydrazone dyes, such as SSY, with nonionic surfactants, such as Span 80, in aqueous media [224]. Span 80 molecules reduce the oil-water interfacial tension by orienting themselves perpendicularly to the interface, with the head pointing to the water phase, and the tail to the oil phase.

On the other hand, the carbonyl group and hydroxyl group of Span 80 interact with the carbonyl group of SSY through hydrogen bonding in water media, as indicated with red color in Fig. 5.4(b). Consequently, we expect Span 80 to induce tangential anchoring of the SSY aggregates.

5.2.3 Defect structures in a spherical SSY-water droplet

Generally, the structure of the director in a confined space provides key information about the properties of the liquid crystal. When thermotropic nematics are confined to a bulk droplet, we observe a bipolar configuration, provided that the anchoring is planar. The optical texture and molecular structure of such configuration is shown in Fig. 5.5(a)-(c). This structure induces splay distortion at the level of the defects and bend distortion along the meridional lines, as discussed in Chapter 1, Section 1.4.

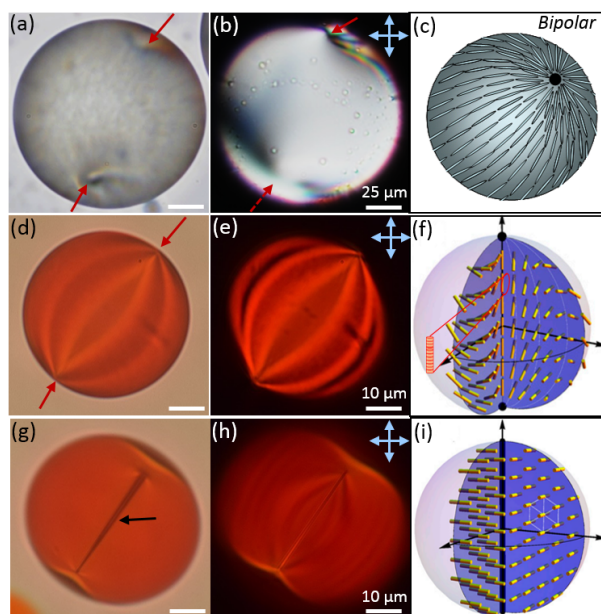


Figure 5.5: Optical microscopy images of different types of liquid crystal droplets. (a) Bright-field and (b) polarized light micrographs of 5CB droplet in poly(vinyl alcohol) (PVA) solution. The red arrows indicate boojums at the aqueous-LC interface of the droplet. (c) Schematic illustration of the bipolar configuration of the LC droplet corresponding to (a) and (b). (d) Bright-field and (e) cross-polarized images of twisted nematic SSY droplet. (f) Jones matrix-simulated twisted bipolar configuration. (g) Bright-field and (h) cross-polarized images of columnar SSY droplet. The black arrow indicates the core line defect. (i) Jones matrix-simulated concentric configuration with a central disclination defect. Figure (f) and (i) adapted from [212].

Interestingly, the nematic SSY droplet exhibits a pair of $s = +1$ boojums, as standard bipolar droplets, but a completely different optical texture, as shown in Fig. 5.5(d) and (e). Such optical texture correspond to a twisted bipolar structure, with the director field shown in Fig. 5.5(f) [212]. The presence of this structure demonstrates that Span 80 induces planar anchoring at the droplet boundary. According to previous studies, the twisted bipolar structure becomes energetically favorable to the standard bipolar one when the elastic constants satisfy the following inequality: $K_2 \leq K_1 - 0.43K_3$ [124, 125]. According to Table 5.1, this condition is satisfied in our system. Because of the low K_2 of the system, the rods (aggregates) twist to adapt themselves to the spherical confinement. The twist occurs along the lines from the bipolar axis to the droplet's surface, as shown in Fig. 5.5(f). Usually a twisted bipolar structure can be induced by the addition of a small amount of a chiral twist agent. For example, twisted structures within droplets of chiral nematic (cholesteric) liquid crystals have been experimentally observed. Interestingly, in SSY-based systems, there is spontaneous chiral symmetry breaking without the presence of chirality at the molecular level [212].

As the concentration of SSY in the drop increases further, the LCLC evolves from the nematic phase to the columnar phase. Fig. 5.5(g) and (h) show the optical texture of a droplet in the columnar phase. The presence of a disclination line connecting opposite poles of the droplet is a signature of a concentric configuration, as discussed in Chapter 1, Section 1.4. The concentric configuration becomes energetically favorable to the bipolar one when $K_3/K_1 \leq 1.0$ [124, 126]. In the nematic phase, at the initial concentration of 30.5 wt%, the ratio K_3/K_1 is slightly above 1.0, according to the values in Table 5.1, but as soon as the concentration of SSY increases due to water evaporation, the ratio becomes lower than 1.0. For instance, we know that in a 31.5 wt% SSY solution, $K_3/K_1 \sim 0.91$, $K_2/K_1 \sim 0.09$ [210]. That would explain why we observe a transformation from the twisted bipolar structure to the concentric structure. According to the director field model of the concentric configuration shown in Fig. 5.5(i), in the columnar phase, the rods align into hexagonal arrays and keep parallel to the boundary, encircling the disclination line in the drop's central axis [212].

The transition between the twisted bipolar configuration and the concentric configuration is shown in the sequence of images in Fig. 5.6(a)-(c). A Jones matrix formalism could provide further information on the evolution of the director field between the two limit configurations. Fig. 5.6(e) shows a top view of a concentric droplet. The size of the defect core seems to be larger than in conventional thermotropic nematics, which could be related to the larger size of the LCLC mesogens.

As the concentration of the drop increases further, the surface of the columnar droplet develops facets, as shown in the sequence of images of Fig. 5.7(a)-(d) [212]. The faceted droplet maintains a rotational symmetry about the core line defect. Facets are a common feature of naturally occurring crystals. Facets appear because of anisotropic growth along different crystallographic directions. Occasionally irregular facets appear due to the non-

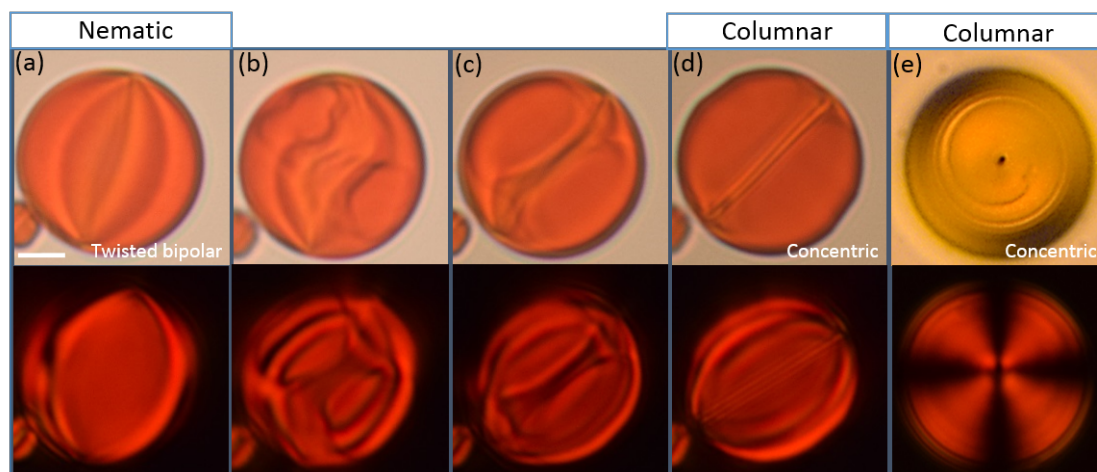


Figure 5.6: Bright-field images (top) and cross-polarized images (bottom) of nematic SSY droplets experiencing a phase transition from the nematic to the columnar phase. (a) SSY droplets in the nematic phase. (b) and (c) Nematic SSY droplets going through the coexistence region. (d) Side-view of a columnar SSY droplet. (e) Top-view of a columnar SSY droplet. Scale bar, $25 \mu\text{m}$.

uniform evaporation of water. The regular facets and the other possible equilibrium crystal shapes can be understood using the Wulff construction [225]. Upon further increase of SSY concentration, the droplet enters the crystalline phase, as shown in Fig. 5.7(e).

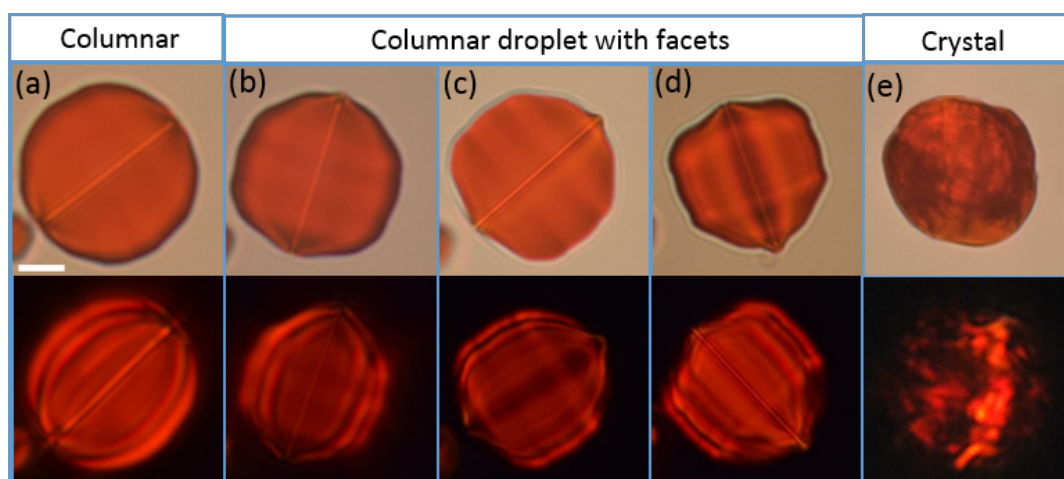


Figure 5.7: Bright-field images (top) and cross-polarized images (bottom) of a columnar SSY droplet experiencing a transition from the columnar to the crystalline phase. As water evaporates, the droplet develops facets. (a) SSY droplet in the columnar phase. (b-d) Columnar SSY droplet developing facets. (e) SSY droplet in the crystalline phase. Scale bar, $25 \mu\text{m}$.

5.3 Sessile droplets

5.3.1 Sessile SSY-water droplet in contact with air

Evaporation controls the concentration of SSY, and thus, the thermodynamic phase in the chromonic system. In spherical droplets, we have reported interesting structural transformations induced by water evaporation which, in this spherical geometry, is roughly isotropic. We consider now sessile droplets, where the evaporation rate depends on the radial distance to the center of the droplet. This creates internal flows that can lead to very interesting effects if the droplet contains suspended particles inside, as it is the case for a SSY water solution. Drying droplets containing suspended particles, salts, polymers, DNA and proteins can lead to deposition patterns that are complex, yet reproducible [226]. Dilute solutions typically exhibit the so-called coffee ring effect [227]. This coffee ring effect is illustrated in Fig. 5.8, where a particle-laden droplet dries on a solid surface, the rate of evaporation is typically highest near the droplet's outer rim, i.e. the contact line. This line is usually pinned to the substrate because of microscopic surface roughness, meaning that it must draw liquid from the droplet's interior to replace what is lost due to evaporation. The particles in the droplet are thereby dragged to the contact line, where they form a ring that helps to maintain the line pinning.

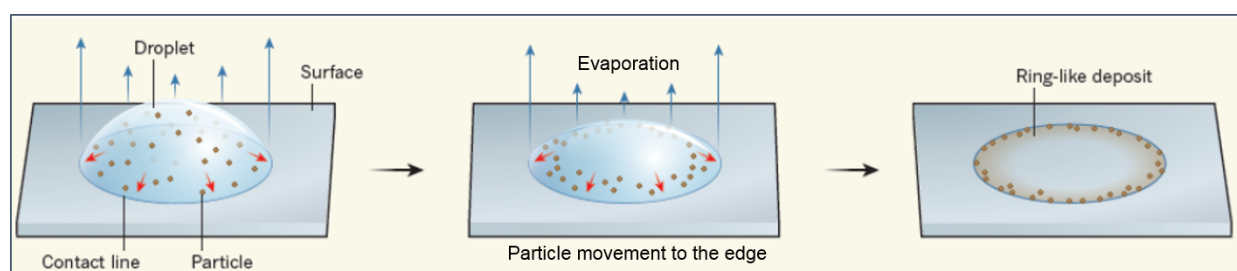


Figure 5.8: Schematic process of the coffee ring effect. Figure modified from [228].

In the case of SSY droplets, the particle concentration gradient generated by the heterogeneous evaporation of the droplet is expected to trigger the coexistence of several thermodynamic phases within the droplet. To study this phenomenon, we produce sessile SSY droplets by depositing a small amount of SSY-water solution on the surface of a glass slide, as schematically shown in Fig. 5.9(a). Since the evaporation flux is greatest near the droplet edge, a nematic-isotropic phase front, and later a columnar-nematic phase front, propagate radially inward, as schematically shown in Fig. 5.9(b). These three phases can be clearly distinguished using polarized microscopy, as shown in Fig. 5.9(d). As evaporation proceeds, four stages of the drying process are simultaneously revealed from outer edge to the drop center: crystal (Cr), columnar (C), nematic (N) and isotropic (I), as shown in Fig. 5.9(c) and (e). The drying multiphase drop exhibits different deposition patterns due to the concentration-dependent isotropic, nematic, and columnar phases in water, which

is consistent with the observations by Zoey *et al* [229].

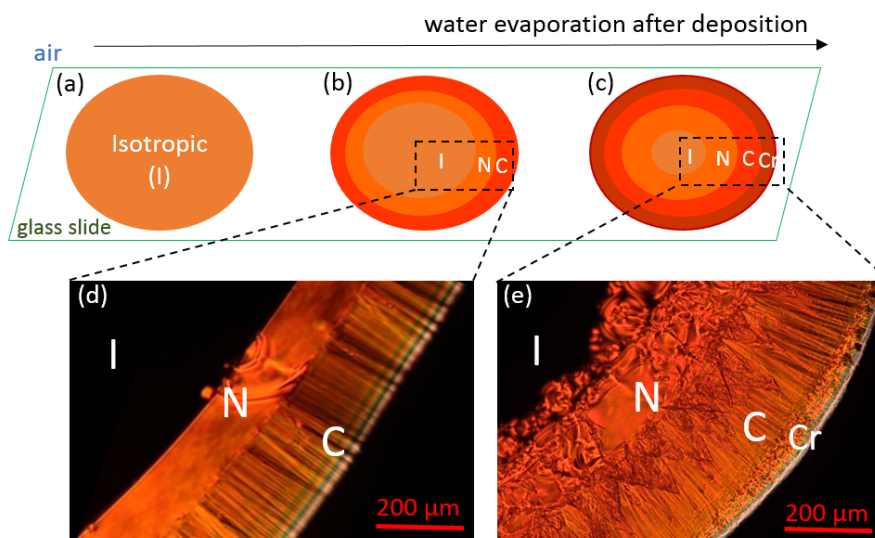


Figure 5.9: Schematic representation of the drying process of a SSY droplet laying on a glass slide at room temperature. (a) The SSY droplet has an initial concentration of 27% by weight and it is in the isotropic phase. (b) The nematic and columnar phases begin to propagate towards the drop center. (c) Final multiphase droplet revealing simultaneously: crystal (Cr), columnar (C), nematic (N) and isotropic (I) phases from the boundary line to the droplet center. (d) Polarized image showing the optical texture corresponding to the state (b). (e) Polarized image showing the optical texture of drying droplet of SSY in the state (c).

5.3.2 Sessile SSY-water droplet in contact with oil

A different phenomenology emerges when the sessile droplet is immersed in oil, so the air-SSY interface is substituted by an oil-SSY interface. To prepare such system, we use a non-ionic triblock polymer surfactant with hydrophilic polyethylene oxide (PEO) in the ends and a hydrophobic polypropylene oxide (PPO) in the middle, such as Pluronic 31R1, whose chemical structure is shown in Fig. 5.10(a). This surfactant makes the SSY-water solution to wet the glass slide, and produce sessile droplets with low contact angle, see Fig. 5.10(b). To make the emulsion, we mix the aqueous isotropic SSY solution (27 wt%) into hexadecane with Pluronic 31R1 (2 wt%) by pipetting and shaking. The volume fraction of SSY solution in hexadecane is $\sim 1\%$ and the resulting sessile droplets have diameters ranging from 1 to 100 μm .

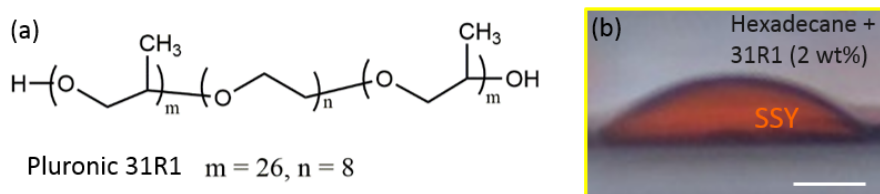


Figure 5.10: (a) Chemical structure of Pluronic 31R1. (b) Side-view of sessile SSY droplet deposited on glass substrate. Scale bar, 25 μm .

Droplet observation was performed at room temperature at slow-drying conditions by placing the droplet in a glass cell with cover slip sealing, as previously described in Fig. 5.3. Fig. 5.11 schematically shows that the sessile SSY droplets immersed in oil, evolve from dilute isotropic liquid phase to the ordered liquid crystal phases during the evaporation process.

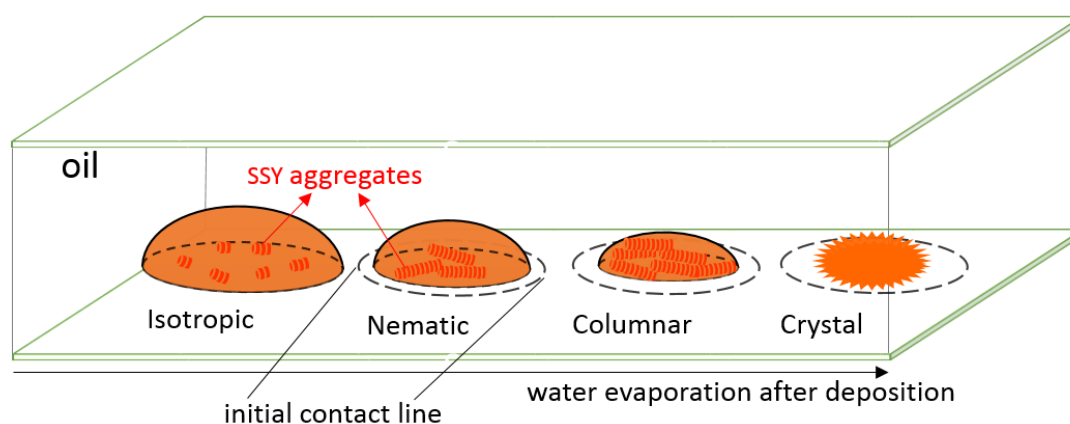


Figure 5.11: Schematic illustration of drying SSY sessile droplets in an oil background. The four depicted sessile droplets on glass substrate represent the evolution of different liquid crystal phases due to water evaporation, the dashed line indicates the initial contact line of the deposition.

At the very early stage of the evaporation process, the SSY concentration in the drop remains below the critical value for the isotropic-nematic phase transition. The SSY suspension has neither translational nor orientational order, the drop is not birefringent, it appears black when viewed through crossed polarizers, as shown in Fig. 5.12(a), where the yellow dashed line indicates the initial contact line. As water evaporates slowly from the droplet, we observe a biphasic region where nematic tactoids (drops with bipolar structure) nucleate, see Fig. 5.12(b), and grow, see Fig. 5.12(c), in an isotropic bulk phase.

These tactoids have spherical shape and bipolar structure. Eventually the nematic tactoids coalesce and gather at the center of the sessile droplet, as shown in Fig. 5.12(d), while additional nematic tactoids keep nucleating at the outer rim. With the growing of the central tactoid, the nematic-isotropic phase front moves radially from the center of the sessile droplet to its periphery, until the whole droplet is in the nematic phase, as shown in Fig. 5.12 (e) and (f). Due to the evaporation of water from the droplet during the phase transition, there is a retraction of the contact line, as indicated by the dashed yellow line.

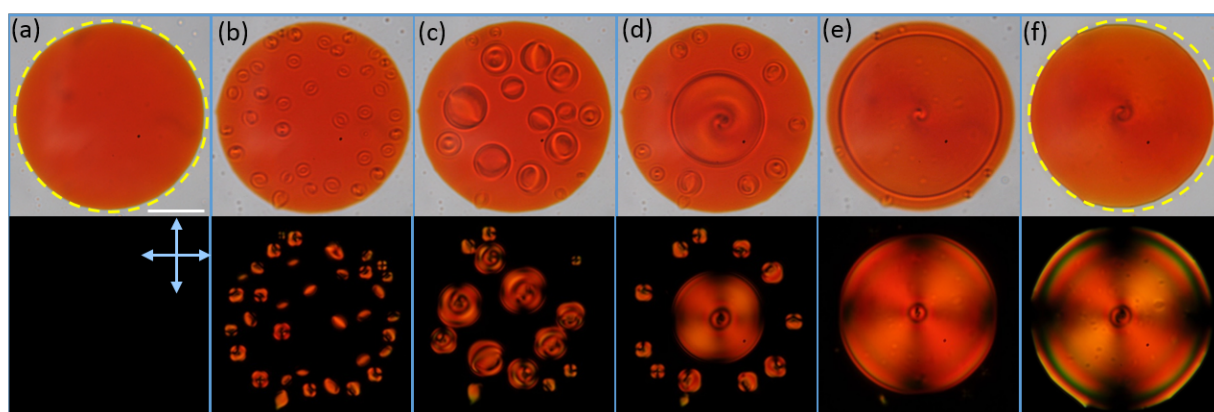


Figure 5.12: (a-f) Bright-field images (top) and cross-polarized images (bottom) of a dilute sessile droplet of SSY in hexadecane experience a phase transition from isotropic to nematic phase. Scale bar, $25 \mu\text{m}$.

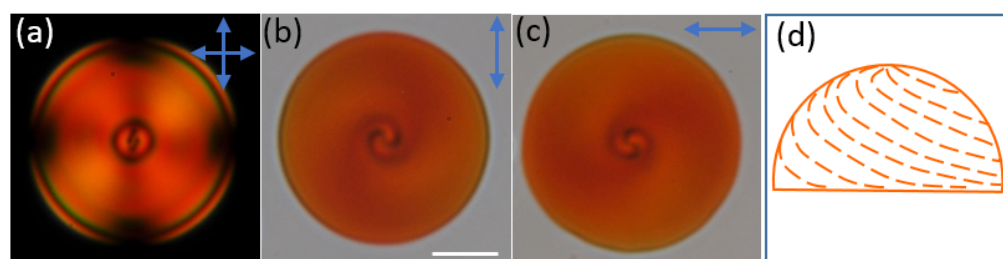


Figure 5.13: (a) Cross-polarized image of SSY sessile droplets. Optical images of SSY sessile droplets in nematic phase observed under polarizing microscope with only a polarizer (b) and only an analyzer (c). (d) Schematic side-view of director field on the curved boundary of the droplet. Scale bar, $10 \mu\text{m}$.

The optical texture and director configuration of the nematic sessile droplet is shown in Fig. 5.13. The texture observed under cross-polarizers is displayed in Fig. 5.13(a), while Fig. 5.13(b) and (c) show the dichroism effect for two different orientations of the

polarizer. These images suggest that the anchoring of the SSY-water solution with the glass slide is planar, resulting in a twisted structure with two $s = +1$ defects, the tentative director field of such a structure is shown in Fig. 5.13(d).

As the evaporation of the nematic sessile droplet (Fig. 5.14(a)) proceeds, the droplets experienced a phase transition from the nematic to the columnar phase through a coexistence region, where we observe developed domains, highlighted in Fig. 5.14(b) with a red dashed line, revealing a clear boundary between the nematic and the columnar phase. It can also be observed that the droplet shrinks and the contact line, indicated by the yellow dashed line, keeps receding due to the water evaporation. The nucleation of the columnar phase can be optically detected by the formation of a crossed brush texture, see Fig. 5.14(b) and (c) (bottom). The presence of this extinction cross suggests the existence of a concentric structure, schematically represented in Fig. 5.14(d), as observed in spherical SSY droplets. The dichroism images, shown in Fig. 5.14(b) and (c) (top), point in the same direction. A similar texture has been previously observed while studying DNA organization in dense 2D hexagonal (columnar) LC phases [230].

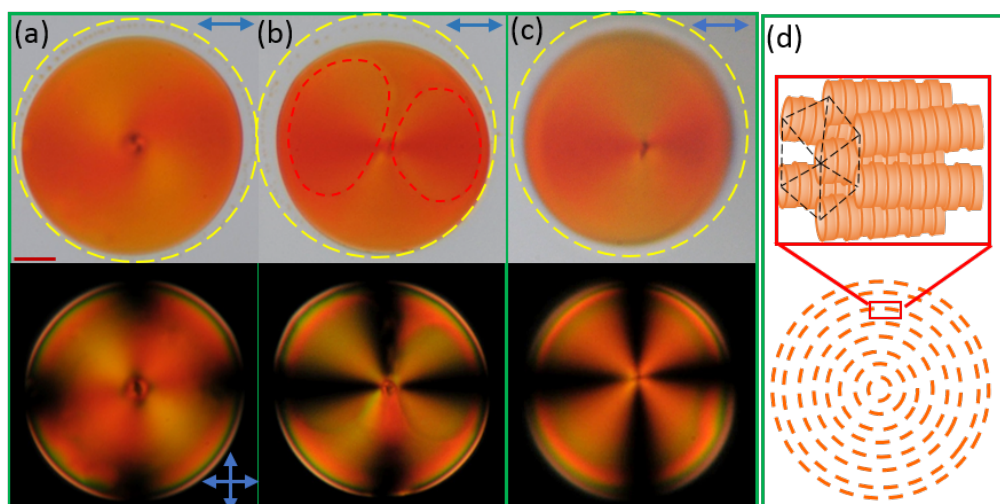


Figure 5.14: Top: optical images of SSY sessile droplets with horizontal polarization and bottom: cross-polarized images of SSY sessile droplets in nematic phase (a), coexistence of nematic and columnar phases (b), and columnar phase (c). (d) An illustration of the expected directions of SSY aggregates in columnar phase. The SSY aggregates are drawn by columns of orange disks that represent SSY molecules. The aggregates are expected to be aligned in a hexagonal lattice. Scale bar, $10 \mu\text{m}$.

More complex textures are produced with the drying of the columnar sessile droplet, as shown in Fig. 5.15. To understand the origin of the emerging structures, we shall recall that in the 2D hexagonal phase, the columns are aligned parallel to each other in a hexagonal lattice. Accordingly, we assume that the drying of the system combined with

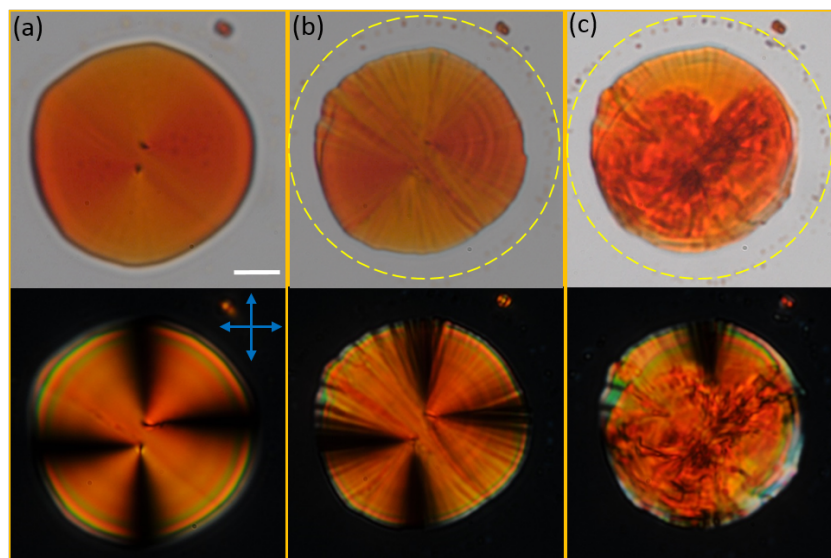


Figure 5.15: Top: bright-field images of SSY sessile droplets and bottom: cross-polarized images of SSY sessile droplets in columnar phase (a), columnar phase with bucklings (b), and crystalline phase (c). Scale bar, $10 \mu\text{m}$.

the high viscosity of columnar phase [229] leads to columnar domains that are unable to rearrange to form regions without distorting the hexagonal lattice. Thus, instead of continuous deformation, we expect to see independent domains that are separated by domain walls, as shown in Fig. 5.15(a), in which the two black dots correspond to two neighboring regions of columnar phase that are separated. Interestingly, the continued drying results in a buckling instability, as shown in Fig. 5.15(b). Upon further evaporation of water, the droplet enters the crystalline phase, as shown in Fig. 5.15(c).

The structure observed from the cross-polarized image shown in Fig. 5.15(b) is reminiscent of the herringbone texture induced by a mechanical stress in columnar LCs [231]. A herringbone texture is a paramorphotic feature that arises when the columnar phase is produced by concentrating the preceding nematic phase. As the solution is progressively concentrated, it is easier for an existing column to be extended than for a new column to form. This creates a differential strain in the mesophase which is relieved when the structure buckles and then fractures, as sketched in Fig. 5.16(a). This could explain why the columnar sessile droplet buckles and fractures, as displayed in Fig. 5.16(c). The schematic representation of the herringbone texture of the sessile droplet is shown in Fig. 5.16(e).

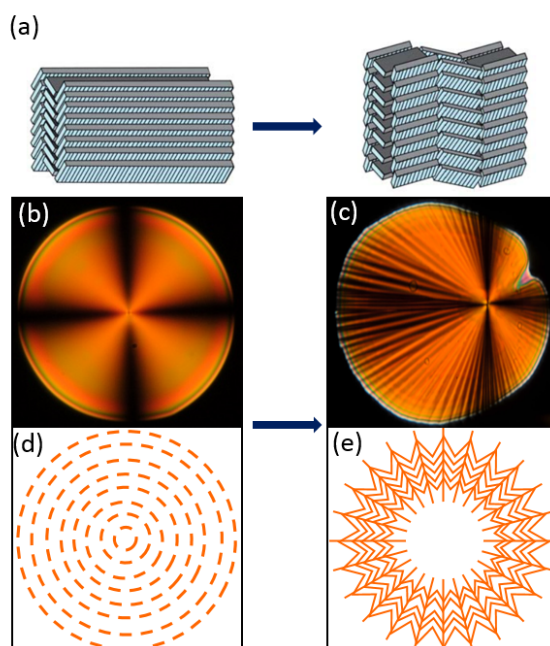


Figure 5.16: (a) The origin of the herringbone texture of columnar phase. Figure adapted from [231]. (b) Cross-polarized image of sessile droplet of SSY in columnar phase and the corresponding model for the director configuration in (d). (c) The herringbone texture of columnar phase formed by concentrating nematic phase. (e) Suggested mechanism for the development of herringbone texture.

5.4 Chromonic SSY shells

We performed some preliminary studies in order to test the viability of making LCLC shells. To fabricate this type of shells, we had to generate oil/water/oil double emulsions, which are known to be difficult to stabilize. For this study, we used a glass capillary device as already described in Chapter 2. The compositions and physical properties of the three fluids used are listed in Table 5.2. A SSY solution with an initial concentration of 27 wt% (in the isotropic phase) was used as middle phase. Span 80 (2 wt%) added to hexadecane was used as the inner phase. Fluorosurfactant (2 wt%) dissolved into fluorinated oil was used as the continuous phase. Since fluorinated oil is immiscible with both water and hydrocarbon oils, coalescence between the innermost drop and the continuous phase does not occur, enhancing the stability of the double emulsions. The production of SSY chromonic shells in the glass capillary device is shown in Fig. 5.17(a). These shells were collected in a vial containing fluorinated oil and 2 wt% fluorosurfactant or directly on a glass cell that was then sealed with cover slip. Due to the volatility of fluorinated oil and the evaporation of water through the oil phase, the SSY concentration in the system increases, leading to an eventual phase transition from the isotropic to the other liquid crystalline phases.

Table 5.2: Compositions of the three fluids used in the experiments to generate SSY Chromonic shells.

| Fluid | Composition | $\rho(kg\ m^{-3})$ | $\mu\ (cP)$ |
|--------|---|--------------------|-------------|
| Inner | Hexadecane + 2 wt% Span 80 | 780 | 30 |
| Middle | SSY solution (27 wt%) | 1000 | 1 |
| Outer | Fluorocarbon oil + 2 wt% Fluorosurfactant | 1614 | 0.77 |

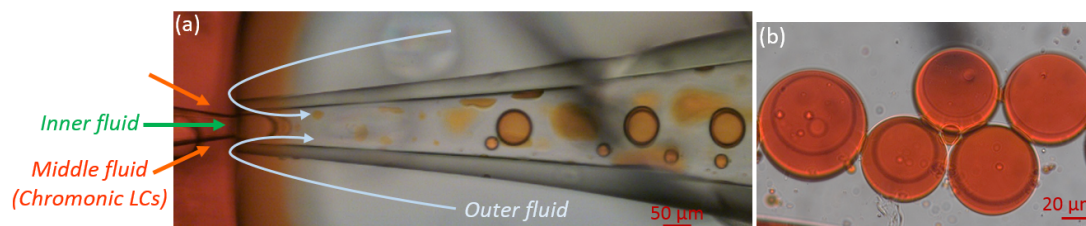


Figure 5.17: (a) Production of SSY Chromonic shells in glass capillary device. Flow rates of inner fluid, Q_i , middle fluid, Q_m , and outer continuous fluid, Q_o , are: $Q_i = 2000\ \mu\text{l/hr}$, $Q_m = 2500\ \mu\text{l/hr}$, $Q_o = 25,000\ \mu\text{l/hr}$. (b) Optical micrograph of SSY Chromonic shells.

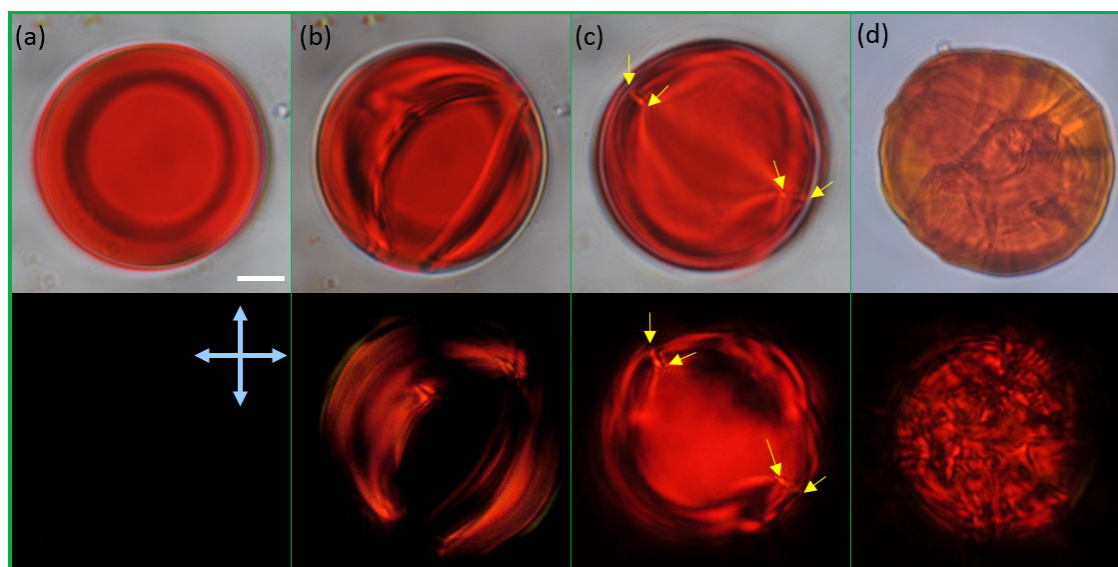


Figure 5.18: SSY shell experiences phase transition from the isotropic to the crystalline phase. Bright-field (top) and cross-polarized (bottom) images of SSY shell in isotropic phase (a), coexistence region of isotropic and nematic phases (b), nematic phase (c) where the defects are indicated by yellow arrows, and crystalline phase (d). Scale bar, $10\ \mu\text{m}$.

Fig. 5.18(a) shows a SSY shell in the isotropic phase. The shell is not birefringent, it appears black when viewed through crossed polarizers. Water in the shell diffuses through

the oil phase, leading to an increase of SSY concentration in the shell. A nematic layer of SSY nucleates, expands and wraps the innermost droplet, as shown in the bright-field and cross-polarized images displayed in Fig. 5.18(b). During this process, we observe the formation of a pair of $s = +1$ boojums, indicated by yellow arrows in Fig. 5.18(c). Interestingly, the boojums are connected by a line that spans the shell. This result contrasts with what is observed in thermotropic nematic shells, where $s = +1$ disclination lines are not stable and disappear by escaping in the third dimension, as discussed in Chapter 1, Section 1.3.2. At even higher concentration of SSY, the shell directly gets into the crystalline phase (Fig. 5.18(d)) without exhibiting those features characteristic of the columnar phase. These preliminary results show the emergence of new behaviors, not observed in thermotropic nematic shells, opening the door for future research.

5.5 Conclusion

In this chapter, we have studied how elastic anisotropy impacts the organization of a nematic phase that is confined to a curved space.

For this study, we have employed a lyotropic chromonic liquid crystal (SSY), displaying a nematic phase in which the twist elastic constant is much smaller than the other ones. By concentrating the SSY sample through evaporation, we can trigger a series of phase transitions: isotropic - nematic - columnar - crystalline. We have explored these transitions and studied the emerging structures in three different geometries: a spherical droplet, a sessile droplet and a spherical shell.

Spherical droplets display a twisted bipolar defect structure in the nematic phase that evolves into a concentric configuration as the system gets into the columnar phase. A further increase in the concentration of SSY makes the droplet develop facets and eventually adopt a crystalline structure. The non-uniform evaporation in free standing sessile droplets triggers mechanisms similar to those responsible for the “coffee ring effect”. This leads to the formation of concentric rings, each of them corresponding to a different phase. When the sessile droplet is immersed in a solvent, the evaporation is more uniform and we observe the emergence of interesting new patterns, such as a herringbone texture when the concentration of SSY is high. Our preliminary results on SSY shells show the formation of defect structures that seem to differ from those observed in conventional thermotropic liquid crystals. Studying these structures will be the focus of future investigation.

Conclusions

In this thesis, we explored the possibility of using liquid crystal shells as mesoscopic counterparts of atoms. Previous experimental and theoretical studies have revealed a great richness in defect configurations spontaneously emerging in liquid crystal shells, which could be exploited to produce particles with sought-after symmetries. Yet, several key challenges, such as scaling down the size of the shells to the colloidal range, or producing shells with a controlled defect structure, remain to be addressed in order to materialize these ideas. In this thesis, we tackle the two challenges mentioned above.

To reduce the size of the shells, we tested the different alternatives for producing shells. We investigated the limits of standard microfluidic techniques and found that they do not allow for scaling the system down to the colloidal scale. We then presented a new microfluidic method based on the “Confined Selective Withdrawal” (CSW) technique. We showed that this method enables a controlled production of shells, with sizes and production frequencies that follow well established scaling laws. The range of sizes that can be attained is significantly larger than with standard microfluidic methods, allowing us to produce shells with diameters smaller than 10 microns.

To produce shells with a controlled valence, we have investigated the energy landscape associated to the different defect structures observed in experimental nematic shells and evaluated the impact of metastability. We studied the possibility of inducing topological transitions between different defect configurations by playing with the shell geometry. We showed that transitions between configurations with different types of defects are energetically forbidden. Interestingly, increasing the overall thickness of the shell, by de-swelling the inner droplet, can lead to two different topological paths depending on the initial state of the system, involving: (i) the re-location of topological defects and (ii) a dramatic transition in which the inner droplet is expelled from the shell when a critical average thickness is reached. We have finally investigated, by means of numerical simulations, the role of elasticity and osmotically driven water fluxes through the shell on the expulsion of the inner droplet.

Finally, we used a lyotropic chromonic liquid crystal, where the elastic constant associated to twist deformation is much lower than the other elastic constants of the liquid crystal. We studied the effect of this elastic anisotropy on the defect structure adopted by

the liquid crystal under different confined geometries. We showed that in spherical droplets, this exotic liquid crystal exhibits a twisted bipolar configuration in the nematic phase, and a bent structure in the columnar phase at room temperature. In a spherical cap geometry, different textures arise within the sessile droplets due to the concentration-dependent liquid crystal phases. Our preliminary experiments with this exotic liquid crystal in double emulsions showed the inherent complexity of elastic anisotropy in spherical geometries.

Bibliography

- [1] J. F. Galisteo-López, M. Ibisate, R. Sapienza, L. S. Froufe-Pérez, Á. Blanco, and C. López, “Self-assembled photonic structures,” *Advanced Materials*, vol. 23, no. 1, pp. 30–69, 2011.
- [2] S. G. Johnson and J. D. Joannopoulos, *Photonic crystals: the road from theory to practice*. Springer Science & Business Media, 2001.
- [3] N.M. Litchinitser and V. M. Shalaev, “Metamaterials: transforming theory into reality,” *JOSA B*, vol. 26, no. 12, pp. B161–B169, 2009.
- [4] O. D. Lavrentovich, “Liquid crystals, photonic crystals, metamaterials, and transformation optics,” *Proceedings of the National Academy of Sciences*, vol. 108, no. 13, pp. 5143–5144, 2011.
- [5] K. H. Smith, E. Tejeda-Montes, M. Poch, and A. Mata, “Integrating top-down and self-assembly in the fabrication of peptide and protein-based biomedical materials,” *Chemical Society Reviews*, vol. 40, no. 9, pp. 4563–4577, 2011.
- [6] T. A. Desai, “Micro-and nanoscale structures for tissue engineering constructs,” *Medical Engineering and Physics*, vol. 22, no. 9, pp. 595–606, 2000.
- [7] N. Vogel, M. Retsch, C.-A. Fustin, A. del Campo, and U. Jonas, “Advances in colloidal assembly: the design of structure and hierarchy in two and three dimensions,” *Chem. Rev.*, vol. 115, no. 13, pp. 6265–6311, 2015.
- [8] G. M. Whitesides and M. Boncheva, “Beyond molecules: Self-assembly of mesoscopic and macroscopic components,” *Proceedings of the National Academy of Sciences*, vol. 99, no. 8, pp. 4769–4774, 2002.
- [9] G. M. Whitesides and B. Grzybowski, “Self-assembly at all scales,” *Science*, vol. 295, no. 5564, pp. 2418–2421, 2002.
- [10] L. Behlau, *Technology guide: Principles-applications-trends*. Springer Science & Business Media, 2009.
- [11] S. Glotzer, M. Solomon, and N. A. Kotov, “Self-assembly: From nanoscale to microscale colloids,” *AIChE Journal*, vol. 50, no. 12, pp. 2978–2985, 2004.

- [12] M. Boncheva and G. M. Whitesides, "Making things by self-assembly," *MRS bulletin*, vol. 30, no. 10, pp. 736–742, 2005.
- [13] A. D. McNaught and A. D. McNaught, *Compendium of chemical terminology*. Blackwell Science Oxford, 1997, vol. 1669.
- [14] A. Einstein, *Investigations on the Theory of the Brownian Movement*. Courier Corporation, 1956.
- [15] A. van Blaaderen, "Materials science: colloids get complex," *Nature*, vol. 439, no. 7076, pp. 545–546, 2006.
- [16] D. Frenkel, "Playing tricks with designer" atoms",," *Science*, vol. 296, no. 5565, pp. 65–66, 2002.
- [17] W. Poon, "Colloids as big atoms," *Science*, vol. 304, no. 5672, pp. 830–831, 2004.
- [18] D. Frenkel, "Colloidal encounters: a matter of attraction," *Science*, vol. 314, no. 5800, pp. 768–769, 2006.
- [19] V. J. Anderson and H. N. Lekkerkerker, "Insights into phase transition kinetics from colloid science," *Nature*, vol. 416, no. 6883, pp. 811–815, 2002.
- [20] A. van Blaaderen, "Chemistry: colloidal molecules and beyond," *Science*, vol. 301, no. 5632, pp. 470–471, 2003.
- [21] Z. Mao, H. Xu, and D. Wang, "Molecular mimetic self-assembly of colloidal particles," *Advanced Functional Materials*, vol. 20, no. 7, pp. 1053–1074, 2010.
- [22] V. N. Manoharan, M. T. Elsesser, and D. J. Pine, "Dense packing and symmetry in small clusters of microspheres," *Science*, vol. 301, no. 5632, pp. 483–487, 2003.
- [23] C. S. Plüsch and A. Wittemann, "Assembly of nanoparticles into colloidal molecules: Toward complex and yet defined colloids with exciting perspectives," in *Advances in Colloid Science*. InTech, 2016.
- [24] F. Li, D. P. Josephson, and A. Stein, "Colloidal assembly: the road from particles to colloidal molecules and crystals," *Angewandte Chemie International Edition*, vol. 50, no. 2, pp. 360–388, 2011.
- [25] K. P. Velikov, C. G. Christova, R. P. Dullens, and A. van Blaaderen, "Layer-by-layer growth of binary colloidal crystals," *Science*, vol. 296, no. 5565, pp. 106–109, 2002.
- [26] M. E. Leunissen, C. G. Christova, A.-P. Hynninen, C. P. Royall, A. I. Campbell, A. Imhof, M. Dijkstra, R. Van Roij, and A. Van Blaaderen, "Ionic colloidal crystals of oppositely charged particles," *Nature*, vol. 437, no. 7056, pp. 235–240, 2005.

- [27] K. Ho, C. T. Chan, and C. M. Soukoulis, “Existence of a photonic gap in periodic dielectric structures,” *Physical Review Letters*, vol. 65, no. 25, p. 3152, 1990.
- [28] S. C. Glotzer and M. J. Solomon, “Anisotropy of building blocks and their assembly into complex structures,” *Nature materials*, vol. 6, no. 8, pp. 557–562, 2007.
- [29] S.-M. Yang, S.-H. Kim, J.-M. Lim, and G.-R. Yi, “Synthesis and assembly of structured colloidal particles,” *Journal of Materials Chemistry*, vol. 18, no. 19, pp. 2177–2190, 2008.
- [30] S. Sacanna, L. Rossi, B. Kuipers, and A. Philipse, “Fluorescent monodisperse silica ellipsoids for optical rotational diffusion studies,” *Langmuir*, vol. 22, no. 4, pp. 1822–1827, 2006.
- [31] Y. Sun and Y. Xia, “Shape-controlled synthesis of gold and silver nanoparticles,” *Science*, vol. 298, no. 5601, pp. 2176–2179, 2002.
- [32] L. Manna, E. C. Scher, and A. P. Alivisatos, “Synthesis of soluble and processable rod-, arrow-, teardrop-, and tetrapod-shaped cdse nanocrystals,” *Journal of the American Chemical Society*, vol. 122, no. 51, pp. 12 700–12 706, 2000.
- [33] S. Sacanna and D. J. Pine, “Shape-anisotropic colloids: Building blocks for complex assemblies,” *Current Opinion in Colloid & Interface Science*, vol. 16, no. 2, pp. 96–105, 2011.
- [34] S. H. Lee and C. M. Liddell, “Anisotropic magnetic colloids: a strategy to form complex structures using nonspherical building blocks,” *Small*, vol. 5, no. 17, pp. 1957–1962, 2009.
- [35] S. Sacanna, W. Irvine, P. M. Chaikin, and D. J. Pine, “Lock and key colloids,” *Nature*, vol. 464, no. 7288, pp. 575–578, 2010.
- [36] L. Rossi, S. Sacanna, W. T. Irvine, P. M. Chaikin, D. J. Pine, and A. P. Philipse, “Cubic crystals from cubic colloids,” *Soft Matter*, vol. 7, no. 9, pp. 4139–4142, 2011.
- [37] M. Sindoro, N. Yanai, A.-Y. Jee, and S. Granick, “Colloidal-sized metal–organic frameworks: synthesis and applications,” *Accounts of chemical research*, vol. 47, no. 2, pp. 459–469, 2013.
- [38] J. Henzie, M. Grünwald, A. Widmer-Cooper, P. L. Geissler, and P. Yang, “Self-assembly of uniform polyhedral silver nanocrystals into densest packings and exotic superlattices,” *Nature materials*, vol. 11, no. 2, pp. 131–137, 2012.
- [39] S. C. Glotzer, “Some assembly required,” *Science*, vol. 306, no. 5695, pp. 419–420, 2004.

- [40] E. C. Nelson and P. V. Braun, “Enhancing colloids through the surface,” *Science*, vol. 318, no. 5852, pp. 924–925, 2007.
- [41] A. B. Pawar and I. Kretzschmar, “Fabrication, assembly, and application of patchy particles,” *Macromolecular rapid communications*, vol. 31, no. 2, pp. 150–168, 2010.
- [42] C. A. Mirkin, R. L. Letsinger, R. C. Mucic, and J. J. Storhoff, “A dna-based method for rationally assembling nanoparticles into macroscopic materials,” *Nature*, vol. 382, no. 6592, pp. 607–609, 1996.
- [43] S. Y. Park, A. K. Lytton-Jean, B. Lee, S. Weigand, G. C. Schatz, and C. A. Mirkin, “Dna-programmable nanoparticle crystallization,” *Nature*, vol. 451, no. 7178, pp. 553–556, 2008.
- [44] P. L. Biancaniello, A. J. Kim, and J. C. Crocker, “Colloidal interactions and self-assembly using dna hybridization,” *Physical Review Letters*, vol. 94, no. 5, p. 058302, 2005.
- [45] A. J. Kim, P. L. Biancaniello, and J. C. Crocker, “Engineering dna-mediated colloidal crystallization,” *Langmuir*, vol. 22, no. 5, pp. 1991–2001, 2006.
- [46] F. A. Aldaye and H. F. Sleiman, “Dynamic dna templates for discrete gold nanoparticle assemblies: control of geometry, modularity, write/erase and structural switching,” *Journal of the American Chemical Society*, vol. 129, no. 14, pp. 4130–4131, 2007.
- [47] M. E. Leunissen, R. Dreyfus, R. Sha, T. Wang, N. C. Seeman, D. J. Pine, and P. M. Chaikin, “Towards self-replicating materials of dna-functionalized colloids,” *Soft Matter*, vol. 5, no. 12, pp. 2422–2430, 2009.
- [48] R. J. Macfarlane, B. Lee, M. R. Jones, N. Harris, G. C. Schatz, and C. A. Mirkin, “Nanoparticle superlattice engineering with dna,” *science*, vol. 334, no. 6053, pp. 204–208, 2011.
- [49] M. R. Jones, R. J. Macfarlane, B. Lee, J. Zhang, K. L. Young, A. J. Senesi, and C. A. Mirkin, “Dna-nanoparticle superlattices formed from anisotropic building blocks,” *Nature materials*, vol. 9, no. 11, pp. 913–917, 2010.
- [50] M. R. Jones, N. C. Seeman, and C. A. Mirkin, “Programmable materials and the nature of the dna bond,” *Science*, vol. 347, no. 6224, p. 1260901, 2015.
- [51] Z. Zhang and S. C. Glotzer, “Self-assembly of patchy particles,” *Nano Letters*, vol. 4, no. 8, pp. 1407–1413, 2004.
- [52] F. Romano and F. Sciortino, “Colloidal self-assembly: Patchy from the bottom up,” *Nature materials*, vol. 10, no. 3, pp. 171–173, 2011.

- [53] Z. Zhang, A. S. Keys, T. Chen, and S. C. Glotzer, “Self-assembly of patchy particles into diamond structures through molecular mimicry,” *Langmuir*, vol. 21, no. 25, pp. 11 547–11 551, 2005.
- [54] P.-G. De Gennes, “Soft matter,” *Reviews of modern physics*, vol. 64, no. 3, p. 645, 1992.
- [55] Q. Chen, S. C. Bae, and S. Granick, “Directed self-assembly of a colloidal kagome lattice,” *Nature*, vol. 469, no. 7330, pp. 381–384, 2011.
- [56] S. Granick, “New developments with janus and multiblock colloids,” in *ABSTRACTS OF PAPERS OF THE AMERICAN CHEMICAL SOCIETY*, vol. 246. AMER CHEMICAL SOC 1155 16TH ST, NW, WASHINGTON, DC 20036 USA, 2013.
- [57] Q. Chen, S. C. Bae, and S. Granick, “Staged self-assembly of colloidal metastructures,” *Journal of the American Chemical Society*, vol. 134, no. 27, pp. 11 080–11 083, 2012.
- [58] Q. Chen, J. Yan, J. Zhang, S. C. Bae, and S. Granick, “Janus and multiblock colloidal particles,” *Langmuir*, vol. 28, no. 38, pp. 13 555–13 561, 2012.
- [59] Z. Gong, T. Hueckel, G.-R. Yi, and S. Sacanna, “Patchy particles made by colloidal fusion,” *Nature*, vol. 550, no. 7675, p. nature23901, 2017.
- [60] D. R. Nelson, “Toward a tetravalent chemistry of colloids,” *Nano Letters*, vol. 2, no. 10, pp. 1125–1129, 2002.
- [61] T. Lubensky and J. Prost, “Orientational order and vesicle shape,” *Journal de Physique II*, vol. 2, no. 3, pp. 371–382, 1992.
- [62] V. Vitelli and D. R. Nelson, “Nematic textures in spherical shells,” *Physical Review E*, vol. 74, no. 2, p. 021711, 2006.
- [63] M. A. Bates, “Nematic ordering and defects on the surface of a sphere: A monte carlo simulation study,” *The Journal of chemical physics*, vol. 128, no. 10, p. 104707, 2008.
- [64] H. Shin, M. J. Bowick, and X. Xing, “Topological defects in spherical nematics,” *Physical review letters*, vol. 101, no. 3, p. 037802, 2008.
- [65] G. Skačej and C. Zannoni, “Controlling surface defect valence in colloids,” *Physical review letters*, vol. 100, no. 19, p. 197802, 2008.
- [66] A. Fernández-Nieves, V. Vitelli, A. S. Utada, D. R. Link, M. Márquez, D. R. Nelson, and D. A. Weitz, “Novel defect structures in nematic liquid crystal shells,” *Physical review letters*, vol. 99, no. 15, p. 157801, 2007.

- [67] T. Lopez-Leon, A. Fernandez-Nieves, M. Nobili, and C. Blanc, “Nematic-smectic transition in spherical shells,” *Physical review letters*, vol. 106, no. 24, p. 247802, 2011.
- [68] T. Lopez-Leon and A. Fernandez-Nieves, “Topological transformations in bipolar shells of nematic liquid crystals,” *Physical Review E*, vol. 79, no. 2, p. 021707, 2009.
- [69] T. Lopez-Leon, M. A. Bates, and A. Fernandez-Nieves, “Defect coalescence in spherical nematic shells,” *Physical Review E*, vol. 86, no. 3, p. 030702, 2012.
- [70] J. Noh, K. R. De Sousa, and J. P. Lagerwall, “Influence of interface stabilisers and surrounding aqueous phases on nematic liquid crystal shells,” *Soft Matter*, vol. 12, no. 2, pp. 367–372, 2016.
- [71] T. Lopez-Leon, V. Koning, K. Devaiah, V. Vitelli, and A. Fernandez-Nieves, “Frustrated nematic order in spherical geometries,” *Nature Physics*, vol. 7, no. 5, pp. 391–394, 2011.
- [72] A. Darmon, M. Benzaquen, S. Čopar, O. Dauchot, and T. Lopez-Leon, “Topological defects in cholesteric liquid crystal shells,” *Soft matter*, vol. 12, no. 46, pp. 9280–9288, 2016.
- [73] A. Darmon, M. Benzaquen, D. Seč, S. Čopar, O. Dauchot, and T. Lopez-Leon, “Waltzing route toward double-helix formation in cholesteric shells,” *Proceedings of the National Academy of Sciences*, p. 201525059, 2016.
- [74] H.-L. Liang, E. Enz, G. Scalia, and J. Lagerwall, “Liquid crystals in novel geometries prepared by microfluidics and electrospinning,” *Molecular Crystals and Liquid Crystals*, vol. 549, no. 1, pp. 69–77, 2011.
- [75] H.-L. Liang, J. Noh, R. Zentel, P. Rudquist, and J. P. Lagerwall, “Tuning the defect configurations in nematic and smectic liquid crystalline shells,” *Phil. Trans. R. Soc. A*, vol. 371, no. 1988, p. 20120258, 2013.
- [76] L. Tran, M. O. Lavrentovich, G. Durey, A. Darmon, M. F. Haase, N. Li, D. Lee, K. J. Stebe, R. D. Kamien, and T. Lopez-Leon, “Change in stripes for cholesteric shells via anchoring in moderation,” *Phys. Rev. X*, vol. 7, p. 041029, Nov 2017.
- [77] G. Friedel, “The mesomorphic states of matter,” in *Annales de Physique*, vol. 18, no. 273, 1922, p. 5.
- [78] P. M. Chaikin and T. C. Lubensky, *Principles of condensed matter physics*. Cambridge university press, 2000.
- [79] P. Chaikin and T. Lubensky, “Principles of condensed matter physics cambridge univ,” *Press, Cambridge*, 1995.

- [80] L. Onsager, “The effects of shape on the interaction of colloidal particles,” *Annals of the New York Academy of Sciences*, vol. 51, no. 1, pp. 627–659, 1949.
- [81] W. L. McMillan, “Simple molecular model for the smectic a phase of liquid crystals,” *Physical Review A*, vol. 4, no. 3, p. 1238, 1971.
- [82] S. Chandrasekhar, “Liquid crystals (cambridge university, cambridge, 1977),” *Google Scholar*, p. 152.
- [83] P. De Gennes, *Solid State Commun. 6, 163 (1968)*; *PG de Gennes and J. Prost, The Physics of Liquid Crystals*. Clarendon Press, Oxford, 1993.
- [84] P. Oswald and P. Pieranski, “Nematic and cholesteric liquid crystals: Concepts and physical properties illustrated by experiments (crc, boca raton, fl),” 2005.
- [85] W. Zwetkoff, “Über die molekülanordnung in der anisotrop-flüssigen phase,” *Acta Phys URSS*, vol. 16, pp. 132–147, 1942.
- [86] W. Maier and A. Saupe, “Eine einfache molekulare theorie des nematischen kristallinflüssigen zustandes,” *Zeitschrift für Naturforschung A*, vol. 13, no. 7, pp. 564–566, 1958.
- [87] P. J. Collings, *Liquid crystals: nature’s delicate phase of matter*. Princeton University Press, 2002.
- [88] C. Oseen, “The theory of liquid crystals,” *Transactions of the Faraday Society*, vol. 29, no. 140, pp. 883–899, 1933.
- [89] F. C. Frank, “I. liquid crystals. on the theory of liquid crystals,” *Discussions of the Faraday Society*, vol. 25, pp. 19–28, 1958.
- [90] G. Crawford, D. W. Allender, and J. Doane, “Surface elastic and molecular-anchoring properties of nematic liquid crystals confined to cylindrical cavities,” *Physical Review A*, vol. 45, no. 12, p. 8693, 1992.
- [91] G. Barbero and G. Durand, “Splay-bend curvature and temperature-induced surface transitions in nematic liquid crystals,” *Physical Review E*, vol. 48, no. 3, p. 1942, 1993.
- [92] M. Kleman and O. D. Lavrentovich, *Soft matter physics: an introduction*. Springer Science & Business Media, 2007.
- [93] S. Čopar, “Topology and geometry of nematic braids,” *Physics Reports*, vol. 538, no. 1, pp. 1–37, 2014.
- [94] B. Jerome, “Surface effects and anchoring in liquid crystals,” *Reports on Progress in Physics*, vol. 54, no. 3, p. 391, 1991.

- [95] A. Sengupta, “Topological microfluidics: present and prospects,” *Liquid Crystals Today*, vol. 24, no. 3, pp. 70–80, 2015.
- [96] A. Rapini and M. Papoular, “Distorsion d’une lamelle nématique sous champ magnétique conditions d’ancrage aux parois,” *Le Journal de Physique Colloques*, vol. 30, no. C4, pp. C4–54, 1969.
- [97] J. A. Castellano, “Surface anchoring of liquid crystal molecules on various substrates,” *Molecular crystals and liquid crystals*, vol. 94, no. 1-2, pp. 33–41, 1983.
- [98] A. D. Rey, “Surfaces and interfaces of liquid crystals, th. rasing and i. musevic,” *Liquid Crystals Today*, vol. 21, no. 2, pp. 51–52, 2012.
- [99] J. M. Brake, A. D. Mezera, and N. L. Abbott, “Effect of surfactant structure on the orientation of liquid crystals at aqueous- liquid crystal interfaces,” *Langmuir*, vol. 19, no. 16, pp. 6436–6442, 2003.
- [100] N. A. Lockwood and N. L. Abbott, “Self-assembly of surfactants and phospholipids at interfaces between aqueous phases and thermotropic liquid crystals,” *Current Opinion in Colloid & Interface Science*, vol. 10, no. 3-4, pp. 111–120, 2005.
- [101] P. Poulin and D. Weitz, “Inverted and multiple nematic emulsions,” *Physical Review E*, vol. 57, no. 1, p. 626, 1998.
- [102] A. Saupe, “Disclinations and properties of the directorfield in nematic and cholesteric liquid crystals,” *Molecular Crystals and Liquid Crystals*, vol. 21, no. 3-4, pp. 211–238, 1973.
- [103] S. Chandrasekhar, “Liquid crystals,” *Cambridge University press*, vol. 49, no. 7, pp. 587–588, 1994.
- [104] P. S. Drzaic, *Liquid crystal dispersions*. World Scientific, 1995, vol. 1.
- [105] N. D. Mermin, “The topological theory of defects in ordered media,” *Reviews of Modern Physics*, vol. 51, no. 3, p. 591, 1979.
- [106] O. D. Lavrentovich, “Topological defects in dispersed words and worlds around liquid crystals, or liquid crystal drops,” *Liquid crystals*, vol. 24, no. 1, pp. 117–126, 1998.
- [107] R. B. Meyer, “On the existence of even indexed disclinations in nematic liquid crystals,” *Philosophical Magazine*, vol. 27, no. 2, pp. 405–424, 1973.
- [108] N. D. Mermin, “Surface singularities and superflow in 3 he-a,” in *Quantum fluids and solids*. Springer, 1977, pp. 3–22.
- [109] A. Erdelyi, W. Magnus, and F. Oberhettinger, “M. abramowitz and ia stegun, hand-book of mathematical functions,” 1972.

- [110] M. Kleman and O. D. Lavrentovich, “Topological point defects in nematic liquid crystals,” *Philosophical Magazine*, vol. 86, no. 25-26, pp. 4117–4137, 2006.
- [111] D. Melzer and F. Nabarro, “Optical studies of a nematic liquid crystal with circumferential surface orientation in a capillary,” *Philosophical Magazine*, vol. 35, no. 4, pp. 901–906, 1977.
- [112] O. Lavrentovich, T. Ishikawa, and E. Terentjev, “Disclination loop in mori-nakanishi ansatz: role of the divergence elasticity,” *Molecular Crystals and Liquid Crystals Science and Technology. Section A. Molecular Crystals and Liquid Crystals*, vol. 299, no. 1, pp. 301–306, 1997.
- [113] H. Mori and H. Nakanishi, “On the stability of topologically non-trivial point defects,” *Journal of the Physical Society of Japan*, vol. 57, no. 4, pp. 1281–1286, 1988.
- [114] R. Ondris-Crawford, E. P. Boyko, B. G. Wagner, J. H. Erdmann, S. Žumer, and J. W. Doane, “Microscope textures of nematic droplets in polymer dispersed liquid crystals,” *Journal of applied physics*, vol. 69, no. 9, pp. 6380–6386, 1991.
- [115] I. Muševič, *Liquid crystal colloids*. Springer, 2017.
- [116] H. Poincaré, “Mémoire sur les courbes définies par une équation différentielle (i),” *Journal de mathématiques pures et appliquées*, vol. 7, pp. 375–422, 1881.
- [117] H. Hopf, “Vektorfelder inn-dimensionalen mannigfaltigkeiten,” *Mathematische Annalen*, vol. 96, no. 1, pp. 225–249, 1927.
- [118] R. D. Kamien, “The geometry of soft materials: a primer,” *Reviews of Modern physics*, vol. 74, no. 4, p. 953, 2002.
- [119] V. Guillemin and A. Pollack, *Differential topology*. Englewood Cliffs, N.J., Prentice-Hall, 1974.
- [120] R. B. Meyer, “Piezoelectric effects in liquid crystals,” *Physical review letters*, vol. 22, no. 18, p. 918, 1969.
- [121] N. D. Mermin, *Boojums all the way through: communicating science in a prosaic age*. Cambridge University Press, 1990.
- [122] O. Prishchepa, V. Y. Zyryanov, A. Gardymova, and V. Shabanov, “Optical textures and orientational structures of nematic and cholesteric droplets with heterogeneous boundary conditions,” *Molecular Crystals and Liquid Crystals*, vol. 489, no. 1, pp. 84–410, 2008.
- [123] G. P. Crawford and S. Zumer, *Liquid crystals in complex geometries: formed by polymer and porous networks*. CRC Press, 1996.

- [124] R. Williams, “Two transitions in tangentially anchored nematic droplets,” *Journal of physics A: mathematical and general*, vol. 19, no. 16, p. 3211, 1986.
- [125] G. Volovik and O. Lavrentovich, “Topological dynamics of defects: boojums in nematic drops,” *Zh Eksp Teor Fiz*, vol. 85, no. 6, pp. 1997–2010, 1983.
- [126] P. Drzaic, “A new director alignment for droplets of nematic liquid crystal with low bend-to-splay ratio,” *Molecular Crystals and Liquid Crystals*, vol. 154, no. 1, pp. 289–306, 1988.
- [127] C. Williams, P. Pierański, and P. Cladis, “Nonsingular $s=+1$ screw disclination lines in nematics,” *Physical Review Letters*, vol. 29, no. 2, p. 90, 1972.
- [128] M. Kléman and M. Schlenker, “The use of dislocation theory in magnetoelasticity,” *Journal of Applied Physics*, vol. 43, no. 7, pp. 3184–3190, 1972.
- [129] Y. Zhou, A. Guo, R. Zhang, J. C. Armas-Perez, J. A. Martínez-González, M. Rahimi, M. Sadati, and J. J. de Pablo, “Mesoscale structure of chiral nematic shells,” *Soft matter*, vol. 12, no. 44, pp. 8983–8989, 2016.
- [130] B. Senyuk, Q. Liu, S. He, R. D. Kamien, R. B. Kusner, T. C. Lubensky, and I. I. Smalyukh, “Topological colloids,” *Nature*, vol. 493, no. 7431, p. 200, 2013.
- [131] C. R. Wand and M. A. Bates, “Monte carlo simulations of nematic and chiral nematic shells,” *Physical Review E*, vol. 91, no. 1, p. 012502, 2015.
- [132] J. Bunning, T. Faber, and P. Sherrell, “The frank constants of nematic 5cb at atmospheric pressure,” *Journal de Physique*, vol. 42, no. 8, pp. 1175–1182, 1981.
- [133] G.-P. Chen, H. Takezoe, and A. Fukuda, “Determination of k_i ($i=1-3$) and μ_j ($j=2-6$) in 5cb by observing the angular dependence of rayleigh line spectral widths,” *Liquid Crystals*, vol. 5, no. 1, pp. 341–347, 1989.
- [134] B. Cabane and S. Hénon, *Liquides. Solutions, dispersions, émulsions, gels*. Belin, 2015.
- [135] A. A. Sonin, *The surface physics of liquid crystals*. Taylor & Francis, 1995.
- [136] J. Lydon, “Chromonic liquid crystalline phases,” *Liquid Crystals*, vol. 38, no. 11-12, pp. 1663–1681, 2011.
- [137] J. Lydon, “Chromonic liquid crystal phases,” *Current opinion in colloid & interface science*, vol. 3, no. 5, pp. 458–466, 1998.
- [138] T. Attwood, J. Lydon, and F. Jones, “The chromonic phases of dyes,” *Liquid Crystals*, vol. 1, no. 6, pp. 499–507, 1986.

- [139] A. Vasilevskaya, E. Generalova, and A. S. Sonin, "Chromonic mesophases," *Russian Chemical Reviews*, vol. 58, no. 9, p. 904, 1989.
- [140] P. J. Collings, A. Dickinson, and E. Smith, "Molecular aggregation and chromonic liquid crystals," *Liquid Crystals*, vol. 37, no. 6-7, pp. 701–710, 2010.
- [141] S.-W. Tam-Chang and L. Huang, "Chromonic liquid crystals: properties and applications as functional materials," *Chemical Communications*, no. 17, pp. 1957–1967, 2008.
- [142] V. R. Horowitz, L. A. Janowitz, A. L. Modic, P. A. Heiney, and P. J. Collings, "Aggregation behavior and chromonic liquid crystal properties of an anionic monoazo dye," *Physical Review E*, vol. 72, no. 4, p. 041710, 2005.
- [143] W. Xiao, C. Hu, D. J. Carter, S. Nichols, M. D. Ward, P. Raiteri, A. L. Rohl, and B. Kahr, "Structural correspondence of solution, liquid crystal, and crystalline phases of the chromonic mesogen sunset yellow," *Crystal Growth & Design*, vol. 14, no. 8, pp. 4166–4176, 2014.
- [144] L. Joshi, S.-W. Kang, D. M. Agra-Kooijman, and S. Kumar, "Concentration, temperature, and pH dependence of sunset-yellow aggregates in aqueous solutions: An x-ray investigation," *Physical Review E*, vol. 80, no. 4, p. 041703, 2009.
- [145] F. Chami and M. R. Wilson, "Molecular order in a chromonic liquid crystal: a molecular simulation study of the anionic azo dye sunset yellow," *Journal of the American Chemical Society*, vol. 132, no. 22, pp. 7794–7802, 2010.
- [146] P. Gruner, B. Riechers, L. A. C. Orellana, Q. Brosseau, F. Maes, T. Beneyton, D. Pekin, and J.-C. Baret, "Stabilisers for water-in-fluorinated-oil dispersions: key properties for microfluidic applications," *Current Opinion in Colloid & Interface Science*, vol. 20, no. 3, pp. 183–191, 2015.
- [147] J.-C. Baret, "Surfactants in droplet-based microfluidics," *Lab on a Chip*, vol. 12, no. 3, pp. 422–433, 2012.
- [148] A. Utada, E. Lorenceau, D. Link, P. Kaplan, H. Stone, and D. Weitz, "Monodisperse double emulsions generated from a microcapillary device," *Science*, vol. 308, no. 5721, pp. 537–541, 2005.
- [149] S. Chandrasekhar and G. Ranganath, "The structure and energetics of defects in liquid crystals," *Advances in Physics*, vol. 35, no. 6, pp. 507–596, 1986.
- [150] G. P. De, J. Prost *et al.*, "The physics of liquid crystals," *Physics Today*, 1993.
- [151] M. Ravnik and S. Žumer, "Landau–de Gennes modelling of nematic liquid crystal colloids," *Liquid Crystals*, vol. 36, no. 10-11, pp. 1201–1214, 2009.

- [152] S. Čopar, T. Porenta, and S. Žumer, “Visualisation methods for complex nematic fields,” *Liquid Crystals*, vol. 40, no. 12, pp. 1759–1768, 2013.
- [153] G. M. Whitesides, “The origins and the future of microfluidics,” *Nature*, vol. 442, no. 7101, pp. 368–373, 2006.
- [154] G. M. Whitesides and A. D. Stroock, “Flexible methods for microfluidics,” *Phys. Today*, vol. 54, no. 6, pp. 42–48, 2001.
- [155] T. Thorsen, S. J. Maerkl, and S. R. Quake, “Microfluidic large-scale integration,” *Science*, vol. 298, no. 5593, pp. 580–584, 2002.
- [156] S.-Y. Teh, R. Lin, L.-H. Hung, and A. P. Lee, “Droplet microfluidics,” *Lab on a Chip*, vol. 8, no. 2, pp. 198–220, 2008.
- [157] R. Seemann, M. Brinkmann, T. Pfohl, and S. Herminghaus, “Droplet based microfluidics,” *Reports on progress in physics*, vol. 75, no. 1, p. 016601, 2011.
- [158] A.M. Gañán-Calvo, “Generation of steady liquid microthreads and micron-sized monodisperse sprays in gas streams,” *Physical Review Letters*, vol. 80, no. 2, p. 285, 1998.
- [159] P. Umbanhowar, V. Prasad, and D. Weitz, “Monodisperse emulsion generation via drop break off in a coflowing stream,” *Langmuir*, vol. 16, no. 2, pp. 347–351, 2000.
- [160] R. Suryo and O. A. Basaran, “Tip streaming from a liquid drop forming from a tube in a co-flowing outer fluid,” *Physics of Fluids*, vol. 18, no. 8, p. 082102, 2006.
- [161] S. L. Anna, N. Bontoux, and H. A. Stone, “Formation of dispersions using flow focusing in microchannels,” *Applied physics letters*, vol. 82, no. 3, pp. 364–366, 2003.
- [162] A. M. Gañán-Calvo and J. M. Gordillo, “Perfectly monodisperse microbubbling by capillary flow focusing,” *Physical review letters*, vol. 87, no. 27, p. 274501, 2001.
- [163] L. Martín-Banderas, M. Flores-Mosquera, P. Riesco-Chueca, A. Rodríguez-Gil, Á. Cebolla, S. Chávez, and A. M. Gañán-Calvo, “Flow focusing: A versatile technology to produce size-controlled and specific-morphology microparticles,” *Small*, vol. 1, no. 7, pp. 688–692, 2005.
- [164] S. Takeuchi, P. Garstecki, D. B. Weibel, and G. M. Whitesides, “An axisymmetric flow-focusing microfluidic device,” *Advanced materials*, vol. 17, no. 8, pp. 1067–1072, 2005.
- [165] M. Seo, C. Paquet, Z. Nie, S. Xu, and E. Kumacheva, “Microfluidic consecutive flow-focusing droplet generators,” *Soft Matter*, vol. 3, no. 8, pp. 986–992, 2007.
- [166] A. R. Abate, J. Thiele, and D. A. Weitz, “One-step formation of multiple emulsions in microfluidics,” *Lab on a Chip*, vol. 11, no. 2, pp. 253–258, 2011.

- [167] Y. Xia and G. M. Whitesides, "Soft lithography," *Annual review of materials science*, vol. 28, no. 1, pp. 153–184, 1998.
- [168] A. D. Stroock and G. M. Whitesides, "Components for integrated poly (dimethylsiloxane) microfluidic systems," *Electrophoresis*, vol. 23, no. 20, pp. 3461–3473, 2002.
- [169] A. R. Abate, A. T. Krummel, D. Lee, M. Marquez, C. Holtze, and D. A. Weitz, "Photoreactive coating for high-contrast spatial patterning of microfluidic device wettability," *Lab on a Chip*, vol. 8, no. 12, pp. 2157–2160, 2008.
- [170] C.-H. Chen, A. R. Abate, D. Lee, E. M. Terentjev, and D. A. Weitz, "Microfluidic assembly of magnetic hydrogel particles with uniformly anisotropic structure," *Advanced materials*, vol. 21, no. 31, pp. 3201–3204, 2009.
- [171] A. Perro, C. Nicolet, J. Angly, S. Lecommandoux, J.-F. Le Meins, and A. Colin, "Mastering a double emulsion in a simple co-flow microfluidic to generate complex polymersomes," *Langmuir*, vol. 27, no. 14, pp. 9034–9042, 2010.
- [172] Z. Nie, S. Xu, M. Seo, P. C. Lewis, and E. Kumacheva, "Polymer particles with various shapes and morphologies produced in continuous microfluidic reactors," *Journal of the American chemical society*, vol. 127, no. 22, pp. 8058–8063, 2005.
- [173] S.-H. Huang, W.-H. Tan, F.-G. Tseng, and S. Takeuchi, "A monolithically three-dimensional flow-focusing device for formation of single/double emulsions in closed/open microfluidic systems," *Journal of Micromechanics and Microengineering*, vol. 16, no. 11, p. 2336, 2006.
- [174] J. R. Anderson, D. T. Chiu, H. Wu, O. Schueller, and G. M. Whitesides, "Fabrication of microfluidic systems in poly (dimethylsiloxane)," *Electrophoresis*, vol. 21, no. 1, pp. 27–40, 2000.
- [175] A. Utada, L.-Y. Chu, A. Fernandez-Nieves, D. Link, C. Holtze, and D. Weitz, "Dripping, jetting, drops, and wetting: The magic of microfluidics," *Mrs Bulletin*, vol. 32, no. 9, pp. 702–708, 2007.
- [176] H. C. Shum, J.-W. Kim, and D. A. Weitz, "Microfluidic fabrication of monodisperse biocompatible and biodegradable polymersomes with controlled permeability," *Journal of the American Chemical Society*, vol. 130, no. 29, pp. 9543–9549, 2008.
- [177] R. K. Shah, H. C. Shum, A. C. Rowat, D. Lee, J. J. Agresti, A. S. Utada, L.-Y. Chu, J.-W. Kim, A. Fernandez-Nieves, C. J. Martinez *et al.*, "Designer emulsions using microfluidics," *Materials Today*, vol. 11, no. 4, pp. 18–27, 2008.
- [178] G. Vladislavljević, I. Kobayashi, and M. Nakajima, "Production of uniform droplets using membrane, microchannel and microfluidic emulsification devices," *Microfluidics and nanofluidics*, vol. 13, no. 1, pp. 151–178, 2012.

- [179] C. J. Martinez, J. W. Kim, C. Ye, I. Ortiz, A. C. Rowat, M. Marquez, and D. Weitz, “A microfluidic approach to encapsulate living cells in uniform alginate hydrogel microparticles,” *Macromolecular bioscience*, vol. 12, no. 7, pp. 946–951, 2012.
- [180] I. G. Loscertales, A. Barrero, I. Guerrero, R. Cortijo, M. Marquez, and A. Ganan-Calvo, “Micro/nano encapsulation via electrified coaxial liquid jets,” *Science*, vol. 295, no. 5560, pp. 1695–1698, 2002.
- [181] L. Rayleigh, “On the instability of jets,” *Proceedings of the London mathematical society*, vol. 1, no. 1, pp. 4–13, 1878.
- [182] J. Plateau, *Quatrime note sur de nouvelles applications curieuses de la persistance des impressions de la rétine*, 1849.
- [183] A. S. Utada, A. Fernandez-Nieves, H. A. Stone, and D. A. Weitz, “Dripping to jetting transitions in coflowing liquid streams,” *Physical review letters*, vol. 99, no. 9, p. 094502, 2007.
- [184] A. Evangelio, F. Campo-Cortés, and J. Gordillo, “Simple and double microemulsions via the capillary breakup of highly stretched liquid jets,” *Journal of Fluid Mechanics*, vol. 804, pp. 550–577, 2016.
- [185] S. A. Nabavi, G. T. Vladislavljević, S. Gu, and E. E. Ekanem, “Double emulsion production in glass capillary microfluidic device: Parametric investigation of droplet generation behaviour,” *Chemical Engineering Science*, vol. 130, pp. 183–196, 2015.
- [186] I. G. Loscertales, A. Barrero, M. Márquez, R. Spretz, R. Velarde-Ortiz, and G. Larsen, “Electrically forced coaxial nanojets for one-step hollow nanofiber design,” *Journal of the American Chemical Society*, vol. 126, no. 17, pp. 5376–5377, 2004.
- [187] A. Barrero and I. G. Loscertales, “Micro-and nanoparticles via capillary flows,” *Annu. Rev. Fluid Mech.*, vol. 39, pp. 89–106, 2007.
- [188] Z. Sun, E. Zussman, A. L. Yarin, J. H. Wendorff, and A. Greiner, “Compound core-shell polymer nanofibers by co-electrospinning,” *Advanced materials*, vol. 15, no. 22, pp. 1929–1932, 2003.
- [189] G. Taylor, “Disintegration of water drops in an electric field,” vol. 280, no. 1382, pp. 383–397, 1964.
- [190] M. Cloupeau and B. Prunet-Foch, “Electrohydrodynamic spraying functioning modes: a critical review,” *Journal of Aerosol Science*, vol. 25, no. 6, pp. 1021–1036, 1994.

- [191] Á. G. Marín, I. G. Loscertales, M. Marquez, and A. Barrero, “Simple and double emulsions via coaxial jet electrosprays,” *Physical review letters*, vol. 98, no. 1, p. 014502, 2007.
- [192] M. Rubio-Rubio, A. Sevilla, and J. Gordillo, “On the thinnest steady threads obtained by gravitational stretching of capillary jets,” *Journal of Fluid Mechanics*, vol. 729, pp. 471–483, 2013.
- [193] E. Castro-Hernández, F. Campo-Cortés, and J. M. Gordillo, “Slender-body theory for the generation of micrometre-sized emulsions through tip streaming,” *Journal of Fluid Mechanics*, vol. 698, pp. 423–445, 2012.
- [194] A. Marin, F. Campo-Cortés, and J. Gordillo, “Generation of micron-sized drops and bubbles through viscous coflows,” *Colloids and Surfaces A: Physicochemical and Engineering Aspects*, vol. 344, no. 1, pp. 2–7, 2009.
- [195] A. Evangelio, F. Campo-Cortes, and J. M. Gordillo, “Pressure gradient induced generation of microbubbles,” *Journal of Fluid Mechanics*, vol. 778, pp. 653–668, 2015.
- [196] A. Chauhan, C. Maldarelli, D. Papageorgiou, and D. Rumschitzki, “Temporal instability of compound threads and jets,” *Journal of Fluid Mechanics*, vol. 420, pp. 1–25, 2000.
- [197] M. Herrada, J. Montanero, C. Ferrera, and A. Gañán-Calvo, “Analysis of the dripping–jetting transition in compound capillary jets,” *Journal of Fluid Mechanics*, vol. 649, pp. 523–536, 2010.
- [198] A. Craya, “Recherches theoriques sur l’écoulement de couches superposees de fluides de densites differentes,” *La houille blanche*, no. 1, pp. 44–55, 1949.
- [199] W. R. Debler, “Stratified flow into a line sink,” *Journal of the Engineering Mechanics Division*, vol. 85, no. 3, pp. 51–66, 1959.
- [200] I. Cohen, H. Li, J. L. Hougland, M. Mrksich, and S. R. Nagel, “Using selective withdrawal to coat microparticles,” *Science*, vol. 292, no. 5515, pp. 265–267, 2001.
- [201] L. Martín-Banderas, A. Rodríguez-Gil, Á. Cebolla, S. Chávez, T. Berdún-Álvarez, J. M. Fernandez Garcia, M. Flores-Mosquera, and A. M. Gañán-Calvo, “Towards high-throughput production of uniformly encoded microparticles,” *Advanced Materials*, vol. 18, no. 5, pp. 559–564, 2006.
- [202] L. D. Zarzar, V. Sresht, E. M. Sletten, J. A. Kalow, D. Blankschtein, and T. M. Swager, “Dynamically reconfigurable complex emulsions via tunable interfacial tensions,” *Nature*, vol. 518, no. 7540, pp. 520–524, 2015.

- [203] D. Seč, T. Lopez-Leon, M. Nobili, C. Blanc, A. Fernandez-Nieves, M. Ravnik, and S. Žumer, “Defect trajectories in nematic shells: Role of elastic anisotropy and thickness heterogeneity,” *Physical Review E*, vol. 86, no. 2, p. 020705, 2012.
- [204] A. Darmon, O. Dauchot, T. Lopez-Leon, and M. Benzaquen, “Elastic interactions between topological defects in chiral nematic shells,” *Physical Review E*, vol. 94, no. 6, p. 062701, 2016.
- [205] V. Koning, T. Lopez-Leon, A. Fernandez-Nieves, and V. Vitelli, “Bivalent defect configurations in inhomogeneous nematic shells,” *Soft Matter*, vol. 9, no. 20, pp. 4993–5003, 2013.
- [206] S. R. Seyednejad, M. R. Mozaffari, and M. R. Ejtehadi, “Confined nematic liquid crystal between two spherical boundaries with planar anchoring,” *Physical Review E*, vol. 88, no. 1, p. 012508, 2013.
- [207] H. Ramezani-Dakhel, M. Sadati, R. Zhang, M. Rahimi, K. Kurtenbach, B. Roux, and J. J. de Pablo, “Water flux induced reorientation of liquid crystals,” *ACS central science*, 2017.
- [208] M. Smoluchowski, “Über brownsche molekularbewegung unter einwirkung äußerer kräfte und deren zusammenhang mit der verallgemeinerten diffusionsgleichung,” *Annalen der Physik*, vol. 353, pp. 1103–1112, 1915.
- [209] A. V. Bui, H. M. Nguyen, and M. Joachim, “Prediction of water activity of glucose and calcium chloride solutions,” *Journal of Food Engineering*, vol. 57, no. 3, pp. 243–248, 2003.
- [210] S. Zhou, Y. A. Nastishin, M. Omelchenko, L. Tortora, V. Nazarenko, O. Boiko, T. Ostapenko, T. Hu, C. Almasan, S. Sprunt *et al.*, “Elasticity of lyotropic chromonic liquid crystals probed by director reorientation in a magnetic field,” *Physical review letters*, vol. 109, no. 3, p. 037801, 2012.
- [211] K. Nayani, R. Chang, J. Fu, P. W. Ellis, A. Fernandez-Nieves, J. O. Park, and M. Srinivasarao, “Spontaneous emergence of chirality in achiral lyotropic chromonic liquid crystals confined to cylinders,” *Nature communications*, vol. 6, p. 8067, 2015.
- [212] J. Jeong, Z. S. Davidson, P. J. Collings, T. C. Lubensky, and A. Yodh, “Chiral symmetry breaking and surface faceting in chromonic liquid crystal droplets with giant elastic anisotropy,” *Proceedings of the National Academy of Sciences*, vol. 111, no. 5, pp. 1742–1747, 2014.
- [213] J. Jeong, G. Han, A. C. Johnson, P. J. Collings, T. C. Lubensky, and A. G. Yodh, “Homeotropic alignment of lyotropic chromonic liquid crystals using noncovalent interactions,” *Langmuir*, vol. 30, no. 10, pp. 2914–2920, 2014.

- [214] J. Jeong, L. Kang, Z. S. Davidson, P. J. Collings, T. C. Lubensky, and A. Yodh, “Chiral structures from achiral liquid crystals in cylindrical capillaries,” *Proceedings of the National Academy of Sciences*, vol. 112, no. 15, pp. E1837–E1844, 2015.
- [215] Z. S. Davidson, L. Kang, J. Jeong, T. Still, P. J. Collings, T. C. Lubensky, and A. Yodh, “Erratum: Chiral structures and defects of lyotropic chromonic liquid crystals induced by saddle-splay elasticity [phys. rev. e 91, 050501 (r)(2015)],” *Physical Review E*, vol. 92, no. 1, p. 019905, 2015.
- [216] P. J. Collings, J. N. Goldstein, E. J. Hamilton, B. R. Mercado, K. J. Nieser, and M. H. Regan, “The nature of the assembly process in chromonic liquid crystals,” *Liquid Crystals Reviews*, vol. 3, no. 1, pp. 1–27, 2015.
- [217] D. Edwards, J. Jones, O. Lozman, A. Ormerod, M. Sintyureva, and G. Tiddy, “Chromonic liquid crystal formation by edicol sunset yellow,” *The Journal of Physical Chemistry B*, vol. 112, no. 46, pp. 14 628–14 636, 2008.
- [218] H.-S. Park, S.-W. Kang, L. Tortora, Y. Nastishin, D. Finotello, S. Kumar, and O. D. Lavrentovich, “Self-assembly of lyotropic chromonic liquid crystal sunset yellow and effects of ionic additives,” *The Journal of Physical Chemistry B*, vol. 112, no. 51, pp. 16 307–16 319, 2008.
- [219] S. V. Shiyankovskii, T. Schneider, I. I. Smalyukh, T. Ishikawa, G. Niehaus, K. Doane, C. J. Woolverton, and O. Lavrentovich, “Real-time microbe detection based on director distortions around growing immune complexes in lyotropic chromonic liquid crystals,” *Physical Review E*, vol. 71, no. 2, p. 020702, 2005.
- [220] S.-W. Tam-Chang, J. Helbley, T. D. Carson, W. Seo, and I. K. Iverson, “Template-guided organization of chromonic liquid crystals into micropatterned anisotropic organic solids,” *Chemical Communications*, no. 5, pp. 503–505, 2006.
- [221] H.-S. Park, A. Agarwal, N. A. Kotov, and O. D. Lavrentovich, “Controllable side-by-side and end-to-end assembly of au nanorods by lyotropic chromonic materials,” *Langmuir*, vol. 24, no. 24, pp. 13 833–13 837, 2008.
- [222] A. Yamaguchi, G. P. Smith, Y. Yi, C. Xu, S. Biffi, F. Serra, T. Bellini, C. Zhu, and N. A. Clark, “Phases and structures of sunset yellow and disodium cromoglycate mixtures in water,” *Physical Review E*, vol. 93, no. 1, p. 012704, 2016.
- [223] I.-H. Lin, D. S. Miller, P. J. Bertics, C. J. Murphy, J. J. de Pablo, and N. L. Abbott, “Endotoxin-induced structural transformations in liquid crystalline droplets,” *Science*, vol. 332, no. 6035, pp. 1297–1300, 2011.
- [224] J. Oakes and P. Gratton, “Solubilisation of dyes by surfactant micelles. part 1; molecular interactions of azo dyes with nonionic and anionic surfactants,” *Coloration technology*, vol. 119, no. 2, pp. 91–99, 2003.

- [225] C. Rottman and M. Wortis, “Statistical mechanics of equilibrium crystal shapes: Interfacial phase diagrams and phase transitions,” *Physics Reports*, vol. 103, no. 1-4, pp. 59–79, 1984.
- [226] R. G. Larson, “Transport and deposition patterns in drying sessile droplets,” *AIChE Journal*, vol. 60, no. 5, pp. 1538–1571, 2014.
- [227] R. D. Deegan, O. Bakajin, T. F. Dupont, G. Huber, S. R. Nagel, and T. A. Witten, “Capillary flow as the cause of ring stains from dried liquid drops,” *Nature*, vol. 389, no. 6653, p. 827, 1997.
- [228] R. G. Larson, “In retrospect: Twenty years of drying droplets,” *Nature*, vol. 550, no. 7677, p. 466, 2017.
- [229] Z. S. Davidson, Y. Huang, A. Gross, A. Martinez, T. Still, C. Zhou, P. J. Collings, R. D. Kamien, and A. Yodh, “Deposition and drying dynamics of liquid crystal droplets,” *Nature communications*, vol. 8, p. 15642, 2017.
- [230] M. De Frutos, A. Leforestier, and F. Livolant, “Relationship between the genome packing in the bacteriophage capsid and the kinetics of dna ejection,” *Biophysical Reviews and Letters*, vol. 9, no. 01, pp. 81–104, 2014.
- [231] J. Lydon, “Chromonic review,” *Journal of Materials Chemistry*, vol. 20, no. 45, pp. 10 071–10 099, 2010.

Résumé

L'un des objectifs majeurs de la recherche contemporaine en science des matériaux est la production d'architectures tridimensionnelles complexes grâce à l'auto-assemblage de briques élémentaires colloïdales. De ce point de vue, le développement de méthodes permettant la production de particules colloïdales capables d'interagir entre elles de façon complexe est donc crucial. Cette thèse décrit une nouvelle stratégie pour produire des particules anisotropes à l'aide de cristaux liquides. Il s'agit de doubles émulsions, où un cristal liquide nématique est confiné à l'intérieur d'une coque sphérique, et dont la géométrie impose la présence de défauts topologiques. Le nombre et la position des défauts déterminent la valence des particules ainsi que la directionnalité des futures liaisons entre celles-ci. Dans cette étude, nous fabriquons de telles coques de cristaux liquides de façon contrôlée à la fois vis-à-vis de leur taille et des configurations de défauts. Nous décrivons les méthodes microfluidiques traditionnelles qui permettent de produire des coques de cristaux liquides, et nous en testons les limites de fonctionnement. Nous montrons que ces techniques ne permettent pas de réduire la taille du système à l'échelle colloïdale. Nous présentons un setup microfluidique amélioré, qui nous permet de produire des coques avec une grande distribution de taille et à haute fréquence. En combinant résultats expérimentaux et simulations numériques, nous étudions la possibilité d'induire des transitions entre différentes configurations de défauts, grâce à une modification continue de la géométrie de la coque. Enfin, nous nous intéressons à un cristal liquide chromonique doté d'une grande anisotropie élastique en phase nématique. Nous étudions la manière dont ce nématique exotique répond à l'influence du confinement et de la courbure, et nous explorons les nouvelles symétries qui en émergent.

Mots Clés

Cristaux liquides, défauts topologiques, microfluidique, émulsions doubles, particules anisotropiques, auto-assemblage.

Abstract

One main goal of modern material science is to produce complex three-dimensional architectures from the self-assembly of pre-designed colloidal building blocks. Developing methods to produce colloidal particles capable to interact in complex ways is crucial in this perspective. This thesis describes a new strategy in which liquid crystals are used for producing anisotropic colloidal particles. These new particles are double emulsions where a nematic liquid crystal is confined to a spherical shell, the geometry of which imposes the presence of topological defects. The number and position of the defects set the valence of the particles as well as the directionality of the eventual bonds between them. Our study aims at fabricating such liquid crystal shells in a controlled way, both in terms of size and defect structure. We describe the standard microfluidic methods used to produce liquid crystal shells and test their operational limits. We show that the standard microfluidic techniques do not allow for scaling the system down to the colloidal scale. We then present a new microfluidic set-up which improves our capability of producing shells in a large range of sizes at high frequencies. Combining experiments and numerical simulations, we study the possibility of inducing transitions between different valence states through a continuous variation of the shell geometry. Finally, we study a lyotropic chromonic liquid crystal, which exhibits a large elastic anisotropy in the nematic phase. We study how this exotic nematic liquid crystal responds to confinement and curvature and investigate the new emerging symmetries.

Keywords

Liquid crystals, topological defects, microfluidics, double emulsions, anisotropic colloids, self-assembly.